SYNTHESIS AND CHARACTERIZATION OF NOVEL HIERARCHICALLY

FUNCTIONALIZED CARBON NANOFIBERS FOR ENERGY CONVERSION AND

STORAGE APPLICATIONS

A Dissertation
Submitted to the Graduate Faculty
of the
North Dakota State University
of Agriculture and Applied Science

By

Zhengping Zhou

In Partial Fulfillment of the Requirements
for the Degree of
DOCTOR OF PHILOSOPHY

Major Program:
Materials and Nanotechnology

June 2014

Fargo, North Dakota

North Dakota State University
Graduate School

Title

Synthesis and Characterization of Novel Hierarchically Functionalized Carbon
Nanofibers for Energy Conversion and Storage Applications

By

Zhengping Zhou

The Supervisory Committee certifies that this *disquisition* complies with North Dakota

State University's regulations and meets the accepted standards for the degree of

DOCTOR OF PHILOSOPHY

SUPERVISORY COMMITTEE:

Dr. Xiangfa Wu

Chair

Dr. Eric Hobbie

Dr. Robert Pieri

Dr. Andriy Voronov

Dr. Long Jiang

Approved:

10/29/2014	Dr. Alan Kallmeyer
Date	Department Chair

ABSTRACT

Among various energy conversion and storage devices available in the market, supercapacitors are deemed as an effective, competitive solution to the increasing demand for high-power density energy-storage devices. Yet, supercapacitors usually carry relatively low energy density compared to batteries. Nanostructured electrode materials are expected being able to greatly enhance the electrochemical performance of supercapacitors. This research aims at rational synthesis and electrochemical characterization of novel hierarchically functionalized carbon nanofibers (CNFs) for use as advanced electrode materials of supercapacitors. These novel CNFs [(i.e., graphene-beaded CNFs (G/CNFs) and carbon nanotube (CNT)-grown CNFs (CNT/CNFs)] were successfully synthesized. The unique synthesis routes consist of electrospinning the precursor polymer nanofibers, followed by controlled carbonization, chemical vapor deposition (CVD) for CNT growth, and in situ polymerization for coating nanostructured conducting polymer. These new electrode materials carry the advantages of G/CNFs and CNT/CNFs (e.g., unique nanostructural continuity, large specific surface area, low intrinsic contact electric resistance, etc.) and conducting polymers (e.g., high pseudocapacitance), and therefore show excellent electrochemical performance including high specific capacitance, superior energy and power densities, and excellent cyclability. In addition, this work also provides the experimental study on parameter dependency of conic angle in electrospinning and scalable fabrication of core-shell nanofibers via needleless emulsion electrospinning.

ACKNOWLEDGMENTS

TABLE OF CONTENTS

LIST OF TABLES

LIST OF FIGURES

xiv

LIST OF ABBREVIATIONS

AC .... Activated carbons

APS .... Ammonium persulfate

CNFs .... Carbon nanofibers

CNTs .... Carbon nanotubes

CV .... Cyclic voltammetry

CVD .... Chemical vapor deposition

DC .... Direct current

DCPD .... Dicyclopentadiene

DMF .... N, N-dimethylformamide

ECR .... Electrical contact resistance (Ω)

EDLCs .... Electrical double layer capacitors

EIS .... Electrochemical impedance spectroscopy

ESL .... Equivalent series inductance (Ω)

ESR .... Equivalent series resistance (Ω)

FTIR .... Fourier transforms infrared spectroscopy

G/CNFs .... Graphene-beaded CNFs

GCD .... Galvanostatic charging/discharging

HEVs .... Hybrid electric vehicles

IPDI .... Isophorone diisocyanate

IR .... Internal resistance

MWNTs .... Multi-walled nanotubes

PAN .... Polyacrylonitrile

PANI ....Polyaniline

PEDOT........................Poly(3,4-ethylenedioxythiophene)

PMCs...........................Polymer matrix composites

PPy ....Polypyrrole

PS ....Polystyrene

Pt ....Platinum

PVA............................Poly (vinyl alcohol)

SEM ....Scanning electron microscope

SWNTs........................Single-walled nanotubes

TEM ....Transmission electron microscope

THF............................Tetrahydrofuran

XRD ....X-ray diffractometer

LIST OF SYMBOLS

θ ....Angles

°C ....Celsius degree

C_s ....Specific capacitance (F/g)

S_a ....Specific area of the electrode (m^2/g)

a_0 ....Effective size of the ion (A$^\circ$)

ε_o ....Dielectric constant

ε_r ....Electrolyte dielectric constant

Ar ....Argon

b ....Pore radius (A$^\circ$)

C_2H_4 ....Ethylene

cm^2/v/s........................Intrinsic electron mobility

Co_3O_4 ....Cobalt oxide

dt ....Discharge time

dV ....Voltage drop upon discharging process

E_d ....Energy density (Wh/kg)

F ....Farad

H_2 ....Hydrogen

H_2SO_4 ....Sulfuric acid

H_3PO_4 ....Phosphoric acid

Hz ....Frequency

I ....Constant charge/discharge current (A)

I_D ....Intensity of the D peak

I_G ....Intensity of the G peak

IrO_2.............................Iridium dioxide

kV/m ....Electric field

kW/kg.........................Kilowatt per kilogram

m ....Mass of electrode materials

MnO_2..........................Manganese dioxide

MoO_3..........................Molybdenum trioxide

$Ni(AcAc)_2$ ....Nickel acetylacetonate

P_d...............................Power density (kW/g)

Q.................................Surface charge

r ....Torus radius

rad/s............................Circular frequency

R_{ct} ....Interfacial charge-transfer resistance

R_s ....Equivalent series resistance

RuO_2...........................Ruthenium dioxide

S/cm ....Electrical conductivity

TiO_2............................Titanium dioxide

V_0...............................Volume of the torus

Wh/kg.........................Watt hours per kilogram

$Z^{/}$ ....Real parts of the complex impedance

$Z^{//}$................................Imaginary parts of the complex impedance

ΔE_{OR}..........................Reversibility of the redox reactions

ε_a.................................Dielectric constant of air

λ ....Wavelength

d ....Effective thickness of the electric double layer

CHAPTER 1. INTRODUCTION

1.1.   Increasing Demands of Alternative Energy Technologies

Fast consumption of nonrenewable fossil fuels and its severe influence on climate change and environmental pollution have become one of the major challenges to our modern society. Fossil fuels such as petroleum oils, coal, and natural gas have constituted the primary sources to meet the world's energy demands since the 20th century. In 2010 the International Energy Agency reported that about 13.2% of the global final energy consumption came from renewables, with 12.3% coming from traditional biofuels and hydropower, while only 0.9% came from new renewable energy sources (e.g., solar, wind, tide, biomass, geothermal energy, etc.). However, more than 81% of the global final energy consumption accounted from fossil fuels (Figure 1.1) (Arunachalam and Fleicher, 2008; Brennan and Owende, 2010; International Energy Agency, 2010; Sharma et al., 2009). Without fossil fuels, most today's social and economic activities such as transportation, communication, production of goods and commercial services could disappear or shrink significantly. Yet, fossil fuels are very limited and nonrenewable resources. Moreover, the emission of green gases and other harmful wastes due to combustion of fossil fuels is the leading factor responsible for global climate change and environmental pollution, which threatens both human health and the entire ecosystem.
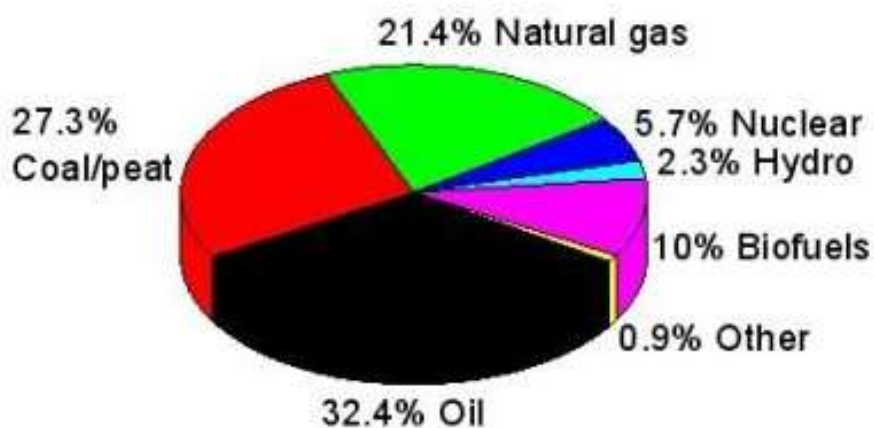
Figure 1.1. Global primary energy supply (2010) (International Energy Agency, 2010).

With the concern of increasing energy consumption, decreasing availability of fossil fuels, and resulting environmental deterioration, substantial effort has been dedicated to development of innovative, affordable, high-efficiency energy harvesting, conversion and storage technologies for utilization of various renewable energy sources such as solar, wind, tide, and geothermal energy. To meet the characteristics of renewable energy resources, novel energy conversion and storage technologies are expected to store and utilize electrical energy generated from various intermittent renewable "clean" energy sources to lower dependence on fossil fuels (Benson and Orr, 2008; Winter and Brodd, 2004; Zhao, 2011). At the forefront of renewable energy technologies, rechargeable batteries, fuel cells and electrochemical capacitors constitute the three major types of energy conversion and storage devices. Among these devices, innovative materials/technologies pay a crucial role in the enhancement of renewable energy conversion and storage capacity, efficiency, and cyclability (Whittingham, 2008). In the last two decades, nanostructured materials have attracted worldwide interests as high-performance electrodes of energy conversion and storage devices because of their unique low-dimension and size effect at nanoscale, which provides favorable high specific surface area to facilitate the fast charge transfer across the surface of

electrodes than conventional electrode materials. As a matter of fact, the efficiency and reliability of energy conversion and storage devices primarily depends on the electrode materials and structures, thus development of high-performance nanostructured materials with optimized material composition, structures and surface morphology is highly demanded to enhance their electrochemical performance. In addition, to better meet the growing demands of high-quality energy requirements, new technological breakthroughs are essential to design and fabrication of innovative electrodes for next generation of low-cost, high efficiency energy conversion and storage devices with high energy and power densities, superior cyclability, and excellent environmental adaptability.

1.2.   Outstanding Problems to Be Resolved

Novel technologies and devices are urgently desired to meet such a global trend of energy harvesting, conversion and storage. In parallel, there are worldwide interests and huge market potential in portable electronics and power tools, all-electric and plug-in hybrid electric vehicles (HEVs), and smart electrical grid integrated with fluctuating energy resources (e.g., solar and wind energies). These broad applications require low-cost, reliable and efficient energy conversion and storage devices with high energy and power densities.

Among a variety of electrochemical energy storage devices, electrical double layer capacitors (EDLCs), also called ultracapacitors or supercapacitors, have been under intensive investigation due to their high power density, ultrafast charge/discharge rates and long life cycles (Miller and Simon, 2008; Chmiola et al., 2006; Simon, and Gogotsi, 2008). It has been generally accepted that supercapacitors can be designed to bridge the gap between rechargeable batteries and standard capacitors used in broad industrial sectors (Snooka et al., 2010). Yet, owing to their

unique charge-storage mechanism of rooting charges at the interface of electrochemical double layers, supercapacitors usually carry a much lower energy density than that of secondary batteries (~1/100-1/10). Thus, it is technically crucial to enhance the energy density of supercapacitors while maintaining their existing advantages via nurturing novel charge-storage strategies, formulating innovative system architectures, and synthesizing new generation electrode materials, electrolytes, and separators to meet the ever growing requirements of future systems (Qu et al., 2012; Wang et al., 2011).

In addition, conducting polymers have been under intensive research as potential low-cost electrode materials for use in supercapacitors due to their high capability of storing charges in the bulk state via a reversible redox reaction and resulting high energy density (Snooka et al., 2010). As one of the promising conducting polymers for use in electrodes, polyaniline (PANI) carries a high theoretical specific pseudocapacitance up to 750 F/g (Snooka et al., 2010; Lota et al., 2004). Besides, PANI also possesses other favorable properties such as low mass density and cost compared to transition-metal oxides [e.g., Ruthenium dioxide (RuO_2), Manganese dioxide (MnO_2), etc.], and good electrical conductivity, easy synthesis, and sound environmental stability (Gomez et al., 2011; Ryu et al. 2002, Lota et al., 2004; Zhao et al., 2011). However, several outstanding issues still need to be resolved in rendering PANI as an electrode material to meet the practical requirements of supercapacitors such as the redox switching, relatively low electrical conductivity, and poor cyclability(Zhao et al., 2011; Zhou et al., 2004). To address these issues, nanostructured PANI have been synthesized on the surface of various carbon materials such as carbon nanotubes (CNTs), carbon nanofibers (CNFs), porous carbon, and graphene for use in supercapacitors (Ghosh et al., 2013; Chen et al., 2013; Wang et al., 2006; Portert et al., 2008; He et al., 2012; Zhou et al., 2013).

Moreover, due to their discrete nature, carbon nanostructures (e.g., CNTs, short CNFs, exfoliated graphene, graphitic nanoflakes, etc.) are typically stacked loosely in porous electrodes. Such a discrete structural configuration may lead to noticeable electrical contact resistance and thus adversely decreases the energy and power densities of the resulting supercapacitors (Ghosh et al., 2013; Chen et al., 2013; Wang et al., 2006; Portert et al., 2008; He et al., 2012; Zhou et al., 2013; Wu et al., 2012). Therefore, new techniques and processes are still desired to resolve such a dilemma of achieving the ultrahigh specific surface area while maintaining the high, reliable electrical connectivity in carbon nanostructures.

1.3.   Dissertation Objectives

The goal of this dissertation research was to investigate three innovative, rational, effective approaches for synthesis of new multifunctional nanofibers for use as hybrid electrode materials of supercapacitors with highly enhanced energy and power densities. Specifically, innovative rational synthesis routes were formulated for fabricating electrospun graphene-beaded CNFs and CNT-grown CNFs, which were further utilized as the supporting backbones for the nanostructured active materials. Besides, high-performance pseudocapacitive materials (e.g., PANI) were coated on the surface of these novel continuous CNFs to form hierarchically functionalized ternary core-shell nanofibrous structures. When integrated into porous electrodes in supercapacitors, these hierarchical multifunctional CNFs were expected to yield high power and energy densities. The high power density was derived directly from the high specific surface area as well as the high conductivity of the continuous electrospun CNFs, while the high energy density was resulted from the pseudocapacitive performance of the novel nanofibrous active materials. Moreover, the internal electrical conductivity, capacitance efficiency, and cycling stability of the resulting hybrid

high-performance supercapacitors would be remarkably enhanced during cycling. Thus, the research was expected to greatly advance the fundamental understanding of novel nanostructured electrode materials for use in supercapacitors and related nanomanufacturing, structural and electrochemical characterization, device fabrication, and performance modeling. The research would significantly contribute to the development of next generation of high-performance electrical energy conversion and storage devices with high energy and power densities for a greener world based on cutting-edge renewable energy technologies. In addition, the research would also stimulate and extend to broad research areas of nano-architectured electrochemical energy conversion and storage devices such as batteries, fuel cells and solar cells based on hybrid hierarchically functionalized nanofibrous electrodes.

Specifically, the research tasks in this dissertation work included the follows:

(1)   To formulate unique rational effective routes to synthesize innovative porous carbon nanofibrous materials by means of low-cost electrospinning, followed by controlled carbonization and surface-functionalization. Three types of multifunctional carbon nanofibrous materials were proposed:

a) Continuous CNFs that would be synthesized by controlled carbonization of electrospun polyacrylonitrile (PAN) nanofibers with the diameter around 200-400 nanometers;

b) Continuous porous CNT-grown CNFs that would be synthesized by controlled carbonization of electrospun composite $PAN/Ni(AcAc)_2$ nanofibers, followed by controlled CNT-growth by means of chemical vapor deposition (CVD);

c) Continuous graphene-beaded CNFs that would be synthesized by controlled carbonization of electrospun PAN/oxidized graphene nanofibers;

(2)   To form hybrid ternary hierarchical porous core-shell materials via controlled deposition of nanostructured PANI onto the above electrospun carbon nanofibrous materials as supporting backbones.

(3)   To characterize the microstructure, surface morphology, and electrochemical properties of the hierarchical nanofibrous electrode materials synthesized above.

(4)   To fabricate both solid-state and aqueous proof-of-concept hybrid supercapacitors with the proposed hierarchical multifunctional nanofibrous materials as electrodes, and to characterize their electrochemical properties.

(5)   To explore the fundamental understanding of the electrochemical performance and related structural and electrochemical mechanisms of the resulting high performance supercapacitors.

(6)   To explore the fundamental understanding of parameter dependency of conic angle in electrospinning and scalable fabrication of core-shell nanofibers via needleless emulsion electrospinning.

1.4.   Chapter Arrangement

The dissertation begins in Chapter 1 with an introduction of the topic that underlies the demands of alternative energy technologies, outstanding problems, dissertation objectives, and chapter arrangement. Chapter 2 is a brief review on the development and energy storage mechanisms of supercapacitors, as well as a novel, low-cost, top-down nanomanufacturing technique – electrospinning. Chapter 3 deals with the fabrication and electrochemical capacitor behavior of CNFs surface-grown with CNTs. Chapter 4 describes the fabrication and characterization of graphene-beaded CNFs for use in supercapacitors. Chapter 5 describes the

ternary core-shell structured CNFs surface-grown with CNTs and PANI as hierarchal multifunctional electrodes for use in pseudosupercapacitors. Chapter 6 focuses on the high-performance porous electrodes for pseudosupercapacitors based on graphene-beaded CNFs surface-coated with nanostructured conducting polymers (PANIs). Chapter 7 covers a fundamental study of the formation of conic angle in electrospinning of nanofibers and scale-up fabrication of core-shell nanofibers by needleless emulsion electrospinning. Each chapter consists of a brief introduction, experimental section, results and discussion, and a summary. Chapter 8 summarizes the main conclusions of the dissertation research and future work.

CHAPTER 2. LITERATURE REVIEW

In this chapter, a brief review is made on electrochemical capacitors and related novel nanostructured materials for electrodes. The emphasis is focused on the development and fundamental principles of electrochemical capacitors and related fabrication methods. Typical electrode materials, e.g., carbon materials, conducting polymers, transition oxides, etc., are further addressed. The nanomanufacturing approaches used in this dissertation work are also reviewed.

2.1. Historical Development of Electrochemical Capacitors

Electrostatic capacitors are the most direct and literal way of storing electrical energy and have been one of the primary building blocks of electrical circuits since the earliest days of electrical engineering. Figure 2.1 shows the historical development of electrical capacitor technology (Tan et al., 2006). The concept of electrostatic charge was first described by the Ancient Greeks, but the first electrical capacitor using electrostatic charge was patented by Pieter van Musschenbroek in 1745 (Conway, 1999), using a Leyden jar. The Leyden jar capacitor, called the "condenser", used a glass phial as the dielectric medium, acidic electrolyte as the conductor, and metal coating on either side of the glass as the electrodes. Since then, the performance of capacitors has progressed through generations of technological evolution in understanding of the fundamental science behind the electrochemical charge storage device with vital contributions from Luigi Galvani, Alessandro Volta, Benjamin Franklin, Michael Faraday, and Joseph John Thompson, among others (Conway, 1999).
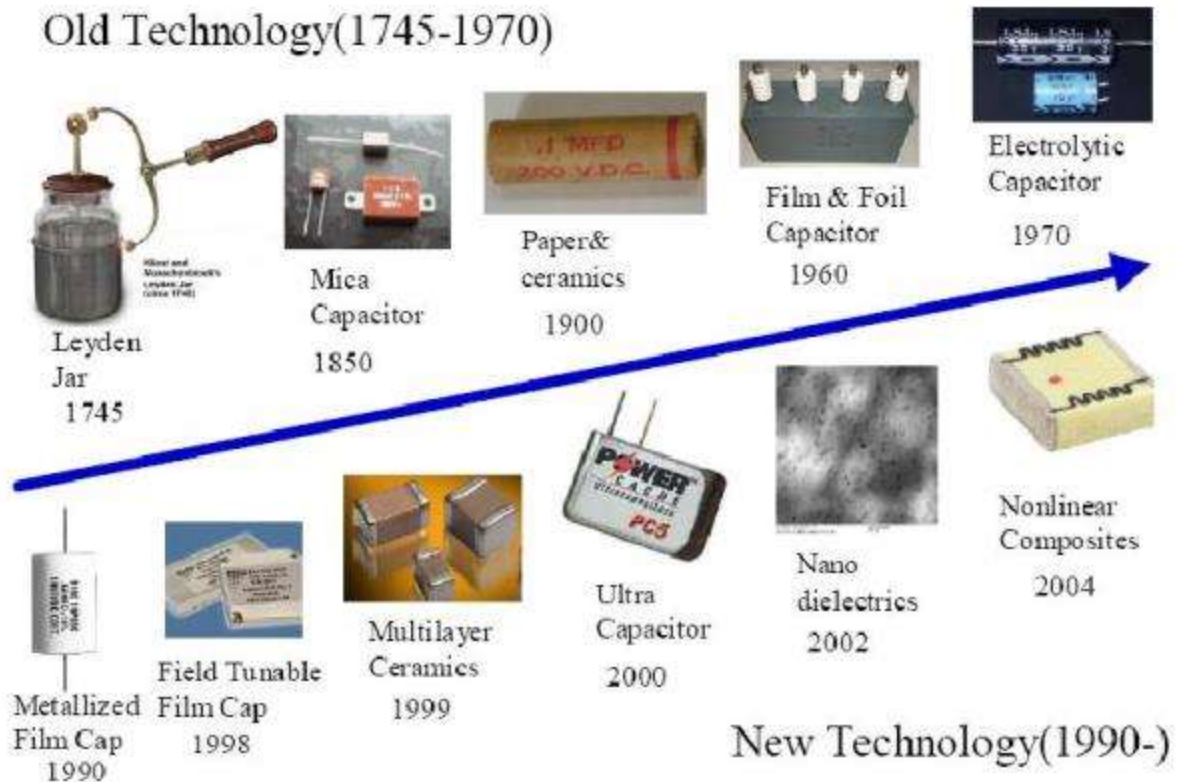
Figure 2.1. Historical evolution of capacitor technology (Tan, 2006).

Electrostatic capacitors accumulate and store electric charges on the conductive electrodes separated by an insulator or dielectric material (Aricò et al., 2005; Benson and Orr, 2008; Bruce et al., 2008; Dunn et al., 2011; Song et al., 2011; Winter and Brodd, 2004; Zhao et al., 2011). The primary advantages of electrostatic capacitors include high power density of over 10 kW/kg, fast charge/discharge rates within tens of microseconds, and low equivalent series resistance (ESR) and inductance (ESL) (Zhao et al., 2011). Current commonly used dielectric materials in electrostatic capacitors include electrolytics, ceramics, polymer films and mica, which are typically available in planar or spiral wound constructions and employed widely in microelectronic devices. Although electrostatic capacitor technology appears to be the ideal choice for high-speed electronic devices and circuits, the specific capacitance generated by an electrostatic capacitor is typically less than 10 mF/g and related energy density is less than 0.1 Wh/kg.

10

Historically, the phenomenon of storing electrical charges at the interface between an electrode and an electrolytic solution had been extensively studied since the late 1800s. Yet, the first practical device based on electrolytic capacitors was invented as late as 1957 by Becker in General Electric Co. This first capacitor was based on high surface-area porous carbon electrodes in an aqueous electrolyte (see Figure 2.2). Later, in 1966 the Standard Oil Company of Ohio (SOHIO) patented the first commercial electrochemical charge storage device based on the double-layer capacitance of high surface-area carbon material in a non-aqueous tetraalkylammonium electrolyte (Rightmire, 1966). However, it was not until 1978 that Nippon Electric Company (NEC) and Panasonic Co. in Japan started to manufacture double-layer capacitors based on aqueous electrolyte in pasted electrodes and non-aqueous electrolyte in non-pasted electrodes, respectively (Endo et al., 2001). In the same year, NEC coined the term "supercapacitor." These low voltage double-layer capacitors with a high internal resistance were primarily designed to replace the unreliable coin cell batteries for memory backup applications. In the 1980s, ELNA Co. designed another type of double-layer capacitors, with the brand name "Dynacap," using an organic electrolyte.
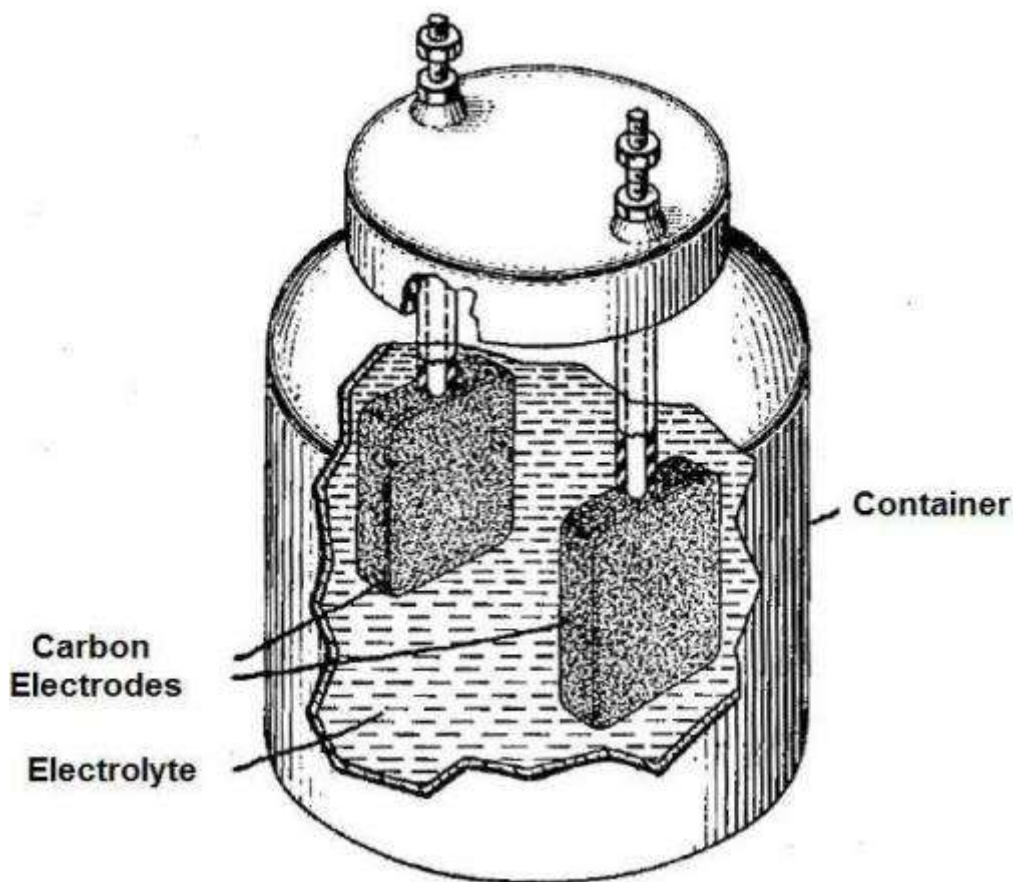
Figure 2.2. The electrolytic capacitor patented by Becker in General Electric Co. (Becker, 1957).

Furthermore, Trasatti proposed the first non-carbon electrode material, RuO_2, in the late 1970's and 1980's for use in supercapacitors, and Conway and coworkers implemented a different principle named pseudocapacitance and carried out extensive fundamental and development work of electrochemical capacitors based on transition metal oxides including RuO_2, MnO_2, Titanium dioxide (TiO_2), Iridium dioxide (IrO_2), and Cobalt oxide (Co_3O_4) (Conway and Angerstein-Kozlowska, 1981; Hadzi-Jordanov et al., 1975; Trasatti and Buzzanca, 1971). The high surface area of carbon based electrodes (1000 – 2000 m^2/g) and solid state transition metal oxides led to the commercialization of electrochemical storage devices by Matsushita Electric Industrial Co. (Japan) in 1980's. These devices were called power capacitors with the power densities of 200 –

300 W/kg (Conway, 1999). However, only in the 1990's the whole field of supercapacitor technology burgeoned in the context of hybrid electric vehicles (HEVs). By 1996, a number of patents on supercapacitors had been granted (Sarangapani, 1996). Two years later, the U.S. Department of Energy (DOE) initiated a 5-year short-term program (1998-2003) and long-term supercapacitor development program (2003-present) with the goals of reaching the specific energy density of 5 and 15 Wh/kg and the specific power density of 500 and 1600 W/kg, respectively (Kotz and Carlen, 2000). Today, many companies, e.g., Maxwell, Tanahashi, AVX, ENC, ESMA, CAP-XX, NCC, NessCap, etc., have been actively involved in developing high-performance electrochemical capacitors in the world for a variety of applications such as those used in electric and fuel cell vehicles for improving acceleration and recovering braking energy, and in microcomputers and system boards as a backup power supply.

2.2.   Energy Storage Mechanisms in Supercapacitors

Based on the charge storage mechanisms, supercapacitors can be categorized into EDLCs and pseudocapacitors.

2.2.1. EDLCs

EDLCs charge/discharge electrical energy only by adsorption of the highly reversible electrolyte ions, which form an electric double layer at the interface between the porous electrodes and electrolyte (Burke, 2000; Conway, 1991; Kotz and Carlen, 2000). A schematic illustration of an EDLC is shown in Figure 2.3. The non-faradaic process of surface-charge/discharge of EDLCs involves only physical adsorption of ions; it doesn't involve any chemical reaction or transfer of charges between the electrolyte and electrode. Because of this unique energy storage mechanism,

EDLCs have a faster charge/discharge rate and a much longer life cycle (>500,000 cycles) than those of rechargeable batteries and fuel cells (Duffy et al., 2008). Yet, EDLCs have a relatively lower energy density because the ion adsorption only happens on the surface of electrodes.
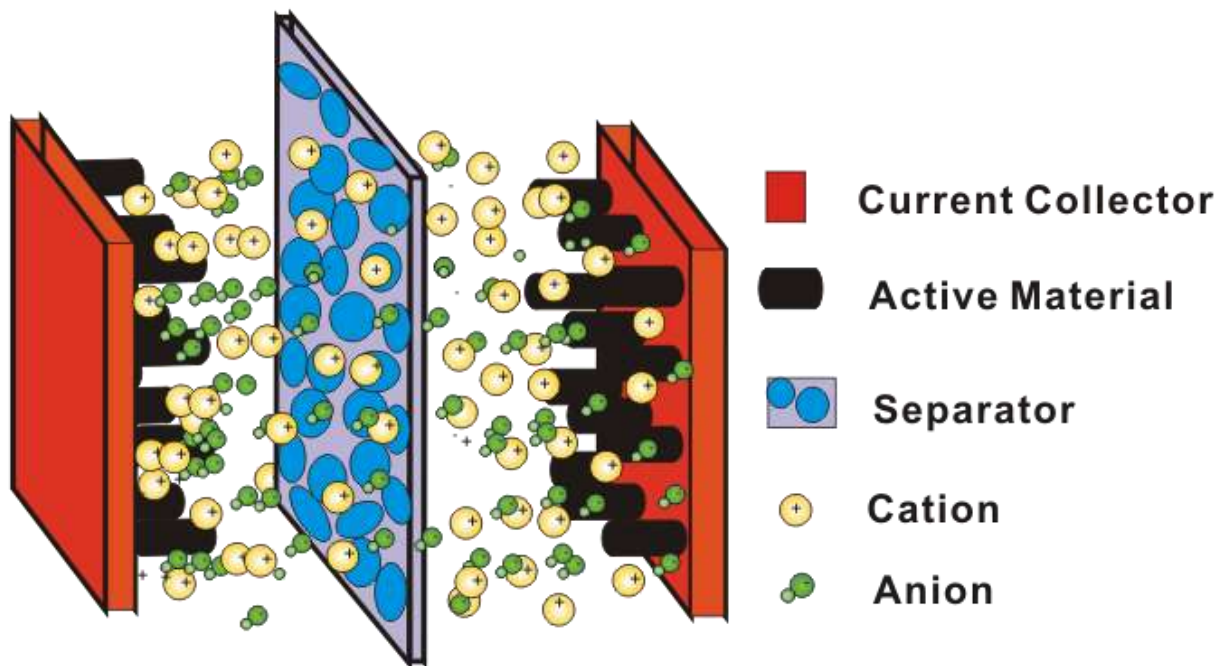
Figure 2.3. Schematic of an EDLC (Conway, 1991).

2.2.2. Pseudocapacitors

Compared to EDLCs, pseudocapacitors store electrical energy depending on the electrosorption process and redox reactions occurring on or near the electrode surface (Simon and Gogotsi, 2008). During this process, electrons and ions transfer through the electrode system, similar to charging and discharging in a battery. Pseudocapacitors usually use transition metal oxides [e.g., RuO_2, Nickel oxide (NiO), Co_3O_4, MnO_2, Molybdenum trioxide (MoO_3), etc.] or conducting polymers [e.g., PANI, polypyrrole (PPy), poly-[3,4-ethylenedioxythiophene] (PEDOT), etc.] as active materials to increase the specific capacitance via pseudocapacitive redox reactions because they have a variety of oxidation states available for redox charge transfer (Fan and Maier, 2006; Frackowiak et al., 2006; Gupta and Miura, 2006; Hu and Chen, 2004; Naoi and

Simon, 2008; Toupin et al., 2004; Xu et al., 2006; Zheng et al., 1995). In principle, pseudocapacitors can provide the energy density with the magnitude over one order higher than EDLCs.

2.2.3. Hybrid systems

Hybrid capacitors are developed to exploit the advantages and mitigate the disadvantages of both EDLCs and pseudocapacitors for improved energy-storage performance. Hybrid capacitors utilize both Faradaic and non-Faradaic processes to store charges; in principle, they can achieve the energy and power densities greater than EDLCs without sacrificing the cycling stability and affordability that have limited the electrochemical performance of pseudocapacitors. Based on their electrode configuration, hybrid systems can be classified as asymmetric and battery-supercapacitor type electrodes. Asymmetric hybrids combine Faradaic and non-Faradaic processes by coupling an EDLC electrode with a pseudocapacitor electrode. In particular, asymmetric hybrids coupling an activated carbon cathode with a conducting polymer anode have been under intensive investigation. In contrast, battery-type hybrids couple a supercapacitor electrode with a battery electrode. Such a unique configuration reflects the demand for higher energy-density supercapacitors and higher power-density batteries, which combines the energy characteristics of batteries with the high power density, long cycle life, and short charging/discharging times of supercapacitors.

2.3.   Capacitance, Energy Density and Power Density of Supercapacitors

According to the capacitor model proposed by Helmholtz in 1853, the double layer capacitance C of a capacitor is (Simon and Gogotsi, 2008)

$$C = \frac{\varepsilon_r \varepsilon_o S_a}{d}, \qquad (2.1)$$

where ε_r is the electrolyte dielectric constant, ε_o is the dielectric constant of 8.854×10^{-12} F/m, S_a is the specific area of the electrode/electrolyte interface accessible to ions, and d is the effective thickness of the electric double layer. However, some studies suggested that the capacitance depends not only on the surface area, but also on the pore size accessible to reversible electrolyte ions (Gamby et al., 2001; Qu and Shi, 1998). Helmholtz's capacitor model was refined recently by Huang et al. (Huang et al., 2008) by taking into account the effect of pore size on the effective capacitance such that the capacitive behavior could be characterized by the following two models corresponding to different pore sizes. When the pore size of the mesoporous carbons is larger than 2 nm, the capacitance is determined as (Huang et al., 2008)

$$C = \frac{\varepsilon_r \varepsilon_o A}{b \ln\left(\frac{b}{b-d}\right)}, \qquad (2.2)$$

when the size of micropores is less than 1 nm, the capacitance is calculated as (Huang et al., 2008)

$$C = \frac{\varepsilon_r \varepsilon_o A}{b \ln\left(\frac{b}{a_0}\right)}, \qquad (2.3)$$

where b is the pore radius and a_0 is the effective size of the ion.

The maximum specific capacitance (C_s) (capacitance per unit mass of a single electrode, F/g) of an EDLC is calculated as a function of the discharging voltage according to the following formula (Kotz and Carlen, 2000; Liu et al., 2003)

$$C_s = \frac{I}{dV(t)/dt}\left(\frac{1}{m_a} + \frac{1}{m_b}\right), \qquad (2.4)$$

where I is the constant charge/discharge current (A), dt is the discharge time (s), dV is the voltage drop (V) during the interval of a discharging process (excluding the internal resistance (*IR*) drop), and m_a and m_b are the masses (g) of the anode and cathode, respectively.

In all energy conversion and storage devices, energy and power densities are the two major measures of their qualities. Energy density describes the amount of energy that can be stored per unit mass while power density delineates how fast the stored energy can be released. The energy storage mechanism in EDLC is due to charge accumulation in the electric double layer at the interfaces between electrodes (cathode and anode) and electrolyte. The energy density E_d (Wh/kg) delivered by the electrodes of a supercapacitor in electrochemical testing is defined by (Niu et al., 2012; Cheng et al., 2013)

$$E_d = \frac{1}{2} \times C_s \times \Delta V^2, \qquad (2.5)$$

while the corresponding power density P_d (W/kg) is expressed as:

$$P_d = \frac{E_d}{\Delta t}. \qquad (2.6)$$

where C_s is the specific capacitance (F/g), ΔV is the voltage drop (V) upon discharging process (excluding the internal resistance (*IR*) drop). An ideal energy storage system is supposed to have high energy and power density; accordingly, it should have high capacitance, large voltage window and low equivalent series resistance (ESR).

2.4. Advantages of Supercapacitor Compared to Other Energy Storage Devices

Figure 2.4 shows the Ragone plot of various electrochemical energy storage systems, a diagram of the power density against the energy density (US defense logistics agency, 2004). From this plot, it can be found that supercapacitors occupy the domain between rechargeable batteries or fuel cells (i.e., high energy density) and conventional capacitors (i.e., ultrahigh power density). Both rechargeable batteries and fuel cells have much lower power densities, which limit their applications, though they have relatively higher energy densities up to several hundred watt hours per kilogram (Wh/kg) than the others. Compared to rechargeable batteries and fuel cells, etc.,

supercapacitors store and release electrical energy based on highly reversible electrolyte ions at the interface between the porous electrodes and electrolyte (Winter and Brodd, 2004; Conway, 1991; Kötz and Carlen; 2000). According to the report of US defense logistics agency, supercapacitors can provide a much higher power density (about 10 kW/kg) than rechargeable batteries and fuel cells (Simon and Gogotsi; 2008). Owing to their unique charge-storage mechanism of rooting charges at the interface of electrochemical double layers, supercapacitors usually carry a much lower energy density (~4-5 Wh/kg) than that of secondary batteries (~1/100-1/10). Thus, supercapacitors can be used as a supplement to provide a higher power boost to rechargeable batteries or fuel cells. Key benefits of supercapacitors include their higher energy/power efficiency, faster charge/discharge rate and longer lifetime even in harsh conditions, which relies on their low electrical internal resistance of the electrodes and the electrical contact resistance between the electrodes and charge collectors (Wu et al., 2012). To date, with their numerous superior advantages, supercapacitors become an increasingly competitive option in a wide range of applications such as instant switches, portable electronics, backup power supplies, regenerative braking systems, and motor starters, and the like (Andrew, 2000; Harrop et al., 2009; Miller and Burke, 2008; Miller and Simon, 2008;).
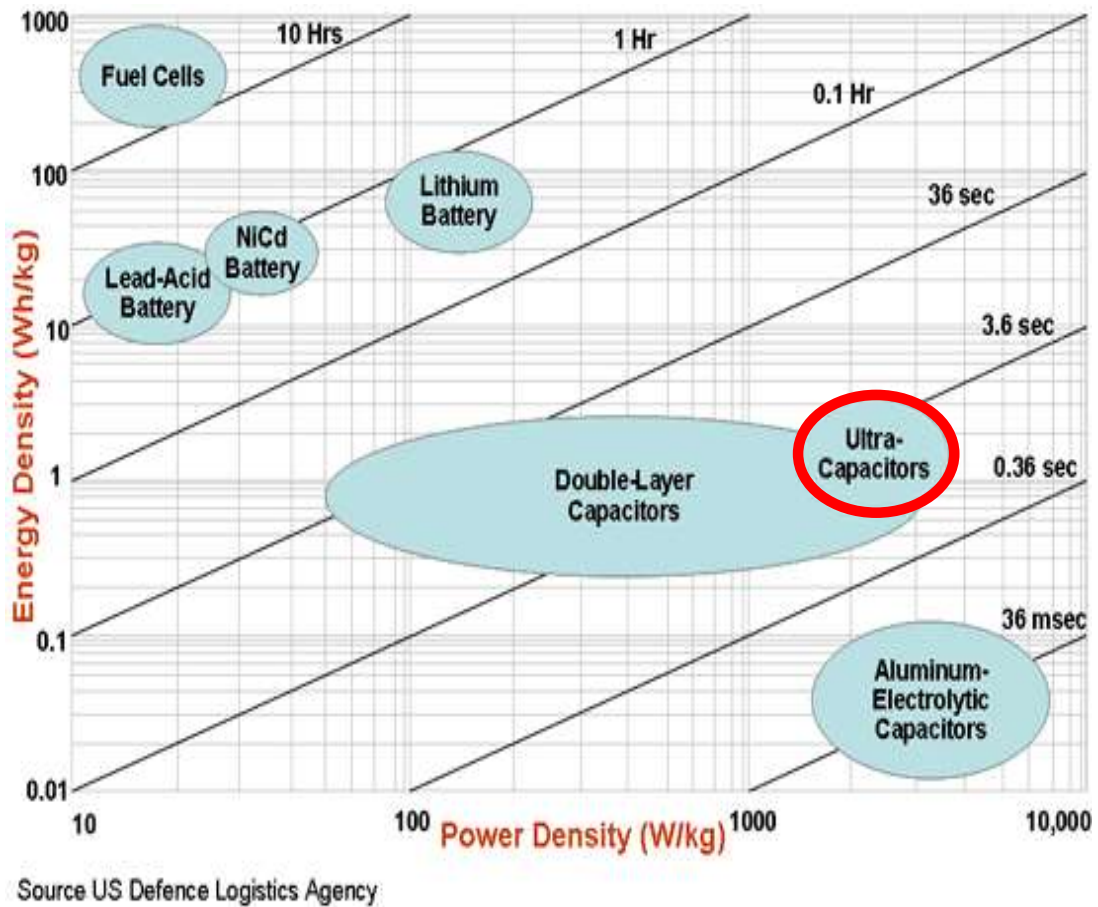
Figure 2.4. Variation of the energy density vs. the power density for various energy conversion and storage devices (US defense logistics agency, 2004).

In principle, the specific capacitance of a supercapacitor relies highly on the specific surface area of the electrodes and the module voltage (Winter and Brodd, 2004; Conway, 1991; Kötz and Carlen; 2000), in which the former is determined by the porosity of the electrode material while the latter is governed by the dielectric properties of the electrolyte. Besides, the energy/power efficiency and lifetime of a supercapacitor also depend upon the internal electrical resistance and electrical contact resistance within the electrodes and between the electrodes and the charge collectors (Wu et al., 2012). Due to the low cost and high electrochemical stability, activated carbon has been extensively integrated into commercialized supercapacitors with the

capacitance of a unit supercapacitor up to 5,000 F (Frackowiak and Béguin, 2001; Pandolfo and Hollendamp, 2006).

2.5. Applications of Supercapacitors

In earlier days because of their limited energy and power densities, supercapacitors were mainly used for low-power, low energy applications such as memory backup. Recently, intensive research has been conducted to increase their energy and power densities. As a result, supercapacitors are offering new solutions for many cutting-edge applications (Miller and Simon, 2008; Chmiola et al., 2006; Simon and Gogotsi, 2008).

The idea of using electrochemical supercapacitors for electric vehicle application is much appealing because of their high energy efficiency, high power density and ability to recuperate energy loss during braking. Fuel cells and batteries are promising energy storage devices for electric vehicles because of their high energy density, but they do not meet the high power requirement needed for acceleration and hill climbing in an instant. Such a crucial peak power requirement can be met by involving supercapacitors (Frackowiak, 2007; Obreja, 2008). As supercapacitors have fast charge rate, it makes regenerative braking possible. It has been reported that by installing supercapacitor-based regenerative braking systems in vehicles, the fuel consumption could be reduced by 15-20% (Clegg, 1996). Also, supercapacitors can be used for the internal combustion engine cranking to reduce the power load of batteries and extend their lifetime. So far, expanding potential applications of high power supercapacitors are under intensive investigation such as those used for railway and subway vehicles.

Supercapacitors can also be used to provide electrical energy needed by power quality systems that ensure reliable and disturbance-free power distribution. Supercapacitors can supply

the energy needed to inject power into the electrical grid and thus compensate for any voltage fluctuations. Similarly, in wind power applications, an energy storage system is required to carry a large power capacity to absorb power surges during wind gusts, and also a large energy capacity for deep wind fluctuations lasting for minutes or longer. A battery-supercapacitor hybrid energy storage system will take advantages of both the technologies and provide high power and energy capacities, and thereby increase the overall efficiency of the energy storage system. The largest portion of the supercapacitors sold nowadays is installed in consumer electronic products, where they mainly serve as power backup sources for memories, microcomputers, system boards, and clocks. In these applications, there is a primary power source which normally supports the load. In case of power outages due to disconnection or turn-off of the primary power source, contact problems due to vibration or shocks, or a drop of the system voltage due to switching to other heavy loads, supercapacitors can supply the instantaneous power. Supercapacitor development is also underway to reduce the cell size and cost. These two issues, particularly the latter, are considered crucial to the continued migration of supercapacitors into new applications. As cost per Farad drops over time, applications of supercapacitors will tend to expand rapidly.

2.6.   Materials for Supercapacitor Electrodes

2.6.1. Carbon materials

The electrodes of EDLCs are usually made of high effective surface-area conducting materials such as activated carbons (AC), carbon aerogels, carbon nanotubes (CNTs), carbon nanofibers (CNFs), and graphene platelets (Fern et al., 2008; Futaba et al., 2006; Izadi-Najafabadi et al., 2010; Liu et al., 2010; Zhu et al., 2010; Frackowiak, 2007; Obreja, 2008). Among these carbon materials, AC is the most widely used material today due to its high specific surface area

and moderate cost. In the recent years, a mesoporous AC obtained by the carbonization of mixtures of poly (vinyl alcohol) (PVA) with magnesium citrate, with a high specific surface area (1,000 to 2,000 m^2/g) and a pore size distribution (2 to 5 nm), is able to reach the power density around 2,600 W/kg at 1 Wh/kg in 2 M H_2SO_4 aqueous electrolytes (Fern et al., 2008).

Among various types of CNTs, single-walled nanotubes (SWNTs) have an ideal limiting specific surface area (up to 1,300 m^2/g), which makes them an attractive candidate for use in the high-capacitance supercapacitors (Izadi-Najafabadi et al., 2010). The energy density of supercapacitors with the electrodes made of aligned high-densely packed SWNTs can reach up to 69.4 Wh/kg (from 180 F/g) by using the zipping effect of liquids (An et al., 2001; Futaba et al., 2006). However, the high cost for mass production of high-quality SWNTs is a challenge to the commercialization of SWNT based supercapacitors.

Continuous electrospun CNFs were firstly prepared by Reneker and his co-workers via stabilization and carbonization of electrospun precursor polymer nanofibers (Reneker and Chun, 1996; Reneker et al., 2006; Reneker and Yarin; 2008). After that, CNFs have shown the great potential for development of cost-effective, structure-flexible, and property-tailorable porous electrodes for uses in supercapacitors and rechargeable batteries (Kim and Yang; 2003; Miao et al., 2010; Zhang et al., 2011; Ji and Zhang, 2009; Ji et al., 2009). When measured in KOH aqueous solution, the specific capacitance of the electrodes based on carbonized electrospun PAN nanofibers (with diameters of 200-400 nm) was 173 F/g at a low charge/discharge current density of 10 mA/g and 120 F/g at a high charge/discharge current density of 1,000 mA/g (Kim and Yang; 2003). The electrochemical performance of such electrodes can be further enhanced via improving the specific surface area of the CNFs through a variety of post-processes such as coating metal (or

metal oxide) nanoparticles on the CNFs to induce the pseudocapacitive effect (Zhang et al., 2011; Ji and Zhang, 2009; Ji et al., 2009).

Graphene consists of two-dimensional (2D) monolayers of sp^2-bonded carbon atoms and has attracted rapidly growing attention in the last decade (Geim, 2009; Novoselov et al., 2004; Huang and Kaner, 2004; He et al., 2012; Katsnelson, 2007; Hu et al., 2012; Fan et al., 2013; Wang et al., 2006). Graphene exhibits unique physical and chemical properties such as excellent electrical conductivity ($\sim 2 \times 10^3$ S/cm) (Wu et al., 2009), large specific surface areas ($\sim 3,100$ m^2/g) (Zhu et al., 2011), and amazing intrinsic electron mobility ($\sim 200,000$ cm^2/v/s) (Zhang et al., 2005). These unique features make graphene a promising nanostructured material for broad application including microelectronics, energy storage devices, fuel cells, sensors, and gas sorbents (Liang and Zhi, 2009; Fowler et al., 2009; Wu et al., 2009). In particular, graphene-based materials can be used as high-performance electrodes for EDLCs and pseudocapacitors, which have demonstrated higher values of specific capacitance than other carbonaceous materials, e.g., CNFs, CNTs, and activated carbon (Stoller et al., 2008; Lv et al., 2009; Liang and Zhi, 2009; Fowler et al., 2009; Wu et al., 2009; Zhou et al., 2012). Recent study of graphene-based supercapacitors reported that a supercapacitor with graphene-based electrodes has a high specific capacitance of 154.1 F/g and energy density of 85.6 Wh/kg (based on the total electrode weight) at a current density of 1 A/g (Liu et al., 2010). In addition, graphene can be conveniently manufactured and functionalized in large quantity at low cost from graphite by means of chemical exfoliation (Balandin et al., 2008; Neto et al., 2009; Lee et al., 2008; Dreyer et al., 2010; Loh et al., 2010; Drzal et al., 2004; Wan et al., 2011; Ruoff, 2008). Furthermore, recent intensive investigations have pointed out that metal oxides (e.g., RuO_2 and MnO_2) and conducting polymers (e.g., PANI, polythiophene, PPy, etc.) loaded/coated on the surface of graphene nanosheets can noticeably

enhance the electrochemical performance of capacitors with graphene as electrodes (Lota et al., 2004; Zhao et al., 2011; Gomez et al., 2011; Ryu et al. 2002). However, in the process of graphene preparation and electrode fabrication, restacking/aggregation of graphene sheets may lead to irreversible agglomeration and folding/scrolling, which results in a decrease of the effective electrochemical performance and therefore limits the practical applications of supercapacitors.

2.6.2. Transition metal oxides

Among various metal oxides, RuO_2 has been broadly studied because of its ultrahigh theoretical specific capacitance (~2,000 F/g), a wide potential window (1.4 V), high electrical conductivity (3×10^5 S/cm), long cycle life, and excellent chemical stability (Hu and Chen, 2004; Naoi and Simon, 2008; Zheng et al., 1995). Although a high specific capacitance (up to 750 F/g) of hydrous RuO_2 has been reported in sulphuric acid electrolytes, its high cost severely limits its attractive commercial applications as a high-capacitance pseudocapacitive electrode material for energy storage devices (Naoi and Simon, 2008). In the recent years, low-cost MnO_2 has been intensively investigated to replace the high-cost RuO_2 for pseudocapacitive electrode materials. Toupin et al. (2004) achieved a very high specific capacitance of 1,380 F/g by using Platinum (Pt) supported amorphous MnO_2 nano-sized ultrathin film as electrodes, which is close to the theoretical value of 1,370 F/g as expected for a redox process involving one electron per manganese atom (Toupin et al., 2004). Yet, the low electrical conductivity, poor compatibility with organic electrolytes, and short life cycle of MnO_2 are the major factors responsible for the rate-limiting for high power applications.

2.6.3. Conducting polymers

Besides metal oxides, conducting polymers are also regarded as the promising electrode materials for use in high-performance pseudocapacitors due to their large pseudocapacitance, relatively high electrical conductivity, low cost, and low mass density (Snooka et al., 2010; Fan and Maier, 2006; Frackowiak et al., 2006; Gupta and Miura, 2006; Xu et al., 2006). The charge-discharge processes of conducting polymer-based electrodes are related to their reversible faradic reactions, which can trigger the pseudocapacitive effect to reach the superior electrochemical performance, e.g., the specific capacitance of 775 F/g for PANI, 480 F/g for PPy, and 210 F/g for PEDOT (Fan and Maier, 2006; Gupta and Miura, 2006; Xu et al., 2006; Lota et al., 2004). The main drawback of conducting polymers as supercapacitor electrodes is related to their low power density and poor mechanical stability during cycling due to the volumetric changes in the doping/undoping processes (Frackowiak et al., 2006). In addition, due to their sluggish transport of ions into the electrode system, the charge/discharge rate of conducting polymer based electrodes is much slower than that of carbon based electrodes.

To address these issues, PANI nanostructures have been grown on the surface of various carbon materials such as CNTs, CNFs, porous carbon, and graphene for use in supercapacitors (Ghosh et al., 2013; Chen et al., 2013; Wang et al., 2006; Portert et al., 2008; He et al., 2012; Zhou et al., 2013; Lota et al., 2004; Zhao et al., 2011; Gomez et al., 2011; Ryu et al. 2002). For example, Zhou et al. reported a supercapacitor based on SWCNTs coated with PANI with a specific capacitance of 190.6 F/g (Zhou et al., 2004). Meng et al. synthesized a flexible paper-like buckypaper coated with PANI films as supercapacitor electrodes, which exhibited a capacitance of 424 F/g with a retention ratio of 89.4% after 1,000 cycles at 1 A/g (Meng et al., 2009). Niu et al. also developed ultrathin flexible SWCNT/PANI hybrid films with a unique continuous

"skeleton/skin" structure; the resulting supercapacitor based on such hybrid films as electrodes had the energy and power densities of 131 W h/kg and 62.5 kW/kg, respectively (Niu et al., 2012). Wei et al. fabricated the novel whisker-like PANI nanorods grown on CNFs as supercapacitor electrodes; the maximum specific capacitance of the resulting supercapacitors was 427 F/g in 1 M H_2SO_4 electrolyte (Wei et al., 2013). Luo et al. also developed porous $ZnCo_2O_4$ nanotubes and carbon-coated MoO_2 nanofibers as high-performance electrode materials by using the low-cost single-nozzle electrospinning technique (Luo et al., 2011; Luo et al., 2012). The electrochemical performance of typical nanostructured electrode materials is tabulated in Table 2.1.

Table 2.1. The electrochemical performance of typical nanostructured electrode materials.

Materials	Specific Capacitance (F/g)	Electrolytes	Voltage Window (V)	Discharge Current Density or Scan Rate
Activated Carbons (AC)	100	1 M $(C_2H_5)_4NBF_4$	0-2.0	1 mA/cm^{-2}
CNTs	90	1 M H_2SO_4	0-1.0	2 mV/s
Graphene sheets	146	1M KOH	-0.9-0.4	50 mA/cm^{-2}
CNFs	173	6 M KOH	0-0.9	10 mA/g
PANI/graphene	425	2 M H_2SO_4	-0.2-0.8	1 mA/g
Polypyrrole/graphene	165	1M NaCl	0-1.0	1 A/g
Polyanline(PANI)/carbon	150	1M $Me_4NCF_3SO_3$/ acetonitrile	0-1.0	20 mA/g
PANI/CNFs	427	1 M H_2SO_4	-0.2-0.8	5 mV/s
PANI-20 wt% CNTs	320	1 M H_2SO_4	0-0.6	5 mV/s
Hydrous RuO_2	750	1M H_2SO_4	-0.2-0.7	50 mA/cm^{-2}
PANI/SWCNT cloth composite	410	1 M H_2SO_4	-0.2-0.8	0.5 A/g

2.7. Nanomanufacturing and Electrospinning

Continuous, scalable, low-cost fabrication of nanomaterials is one of the most active fields in nanotechnology. Several efficient fabrication techniques have been formulated for synthesis of continuous nanofibers with controlled properties such as electrospinning, meltblowing and spunbonding. Electrospinning is a low-cost, scalable, and efficient top-down nanofabrication process that has been well-established for producing continuous nanofibers of a large variety of natural and synthetic polymers, and polymer derived carbon, metals, metal oxides, and ceramics (Doshi and Reneker, 1995; Zheng et al., 1995; Reneker and Chun, 1996; Huang et al., 2003; Hu and Chen, 2004; Dzenis, 2004; Li and Xia, 2004; Grieiner and Wendorff, 2007; Ramaseshan et al., 2007; Reneker et al., 2007; Reneker and Yarin, 2008; Naoi and Simon, 2008). Electrospinning produces nanofibrous materials with the diameters in the range from a few nanometers to micrometers based on the principle of electrohydrodynamic jetting from a single spinneret or liquid surface (Doshi and Reneker, 1995; Reneker and Chun, 1996; Dzenis, 2004; Grieiner and Wendorff, 2007; Reneker et al., 2007; Rutledge and Fridrikh, 2007; Reneker and Yarin, 2008). Due to the large surface-to-mass ratio (specific surface area), tailorable surface morphology, as well as relatively high degree of molecular orientation, electrospun nanofibers are suitable for uses in protective clothing and wound dressing (Gibson et al., 2001; Smith et al., 2001; Smith and Reneker, 2004), fine filtration (Gopal et al., 2006; Barhate and Ramakrishna, 2007; Maze et al., 2007), nanofiber-reinforced polymer matrix composites (PMCs) (Kim and Reneker, 1999; Wu, 2003; Dzenis 2008; Chen et al., 2008; Wu, 2009 (book); Cheng et al., 2010; Chen et al., 2011; Chen et al., 2012 (a, b); Wu et al., 2013; Wu and Yarin, 2013) Furthermore, electrospun nanofibers have also been considered as scaffolds for tissue growth (Li et al., 2002; Matthews et al., 2002; Burger et al., 2006; Pham et al., 2006; Barnes et al., 2007; Xie et al., 2008), drug delivery (Kenawy et al.,

2002; Chew et al., 2006; Liang et al., 2007), sensor/transistor (Ramakrishna et al., 2007; Andrady, 2008), and energy harvesting, conversion and storage (Kim and Yang, 2003; Kim et al., 2007; Ji and Zhang, 2009; Schulz et al., 2010; Zhang et al., 2011; Zhou et al., 2012), among others.

2.7.1. Needle-based electrospinning

As shown in Fig. 2.5, a typical needle-based electrospinning setup consists of a syringe, syringe pump, spinneret, fiber collector, and a high-voltage direct-current (DC) supply. The DC potential of 10 to 50 kV is typically applied between the spinneret and the collector plate to create a high DC electrostatic field, which causes the polymer solution to be highly charged. With increasing the applied voltage, a critical voltage can be reached to ensure that the electrostatic force overcomes the surface tension of the polymer solution. At the beginning of a classic electrospinning process, the solution droplet at the tip of needle will first form a conical structure under the action of electrostatic force (Yarin et al., 2001). The formed conical shape of the solution droplet is called the Taylor cone (Taylor, 1964 and 1969; Spivak and Dzenis, 1999; Yarin, Koombhonges, Reneker, 2001(JAP)). When the electrostatic force surpasses the surface tension, an electrified jet is ejected from the Taylor cone, further elongated and accelerated within the electrostatic field. After a variety of jet destabilizations occurring simultaneously with solvent evaporation, the ultra-thinned jet is solidified and then deposited on the collector to form a nonwoven nanofiber mat. Figure 2.6 shows a few types of nanofibers produced by means of electrospinning for this thesis research in Professor Xiangfa Wu's research group at NDSU.
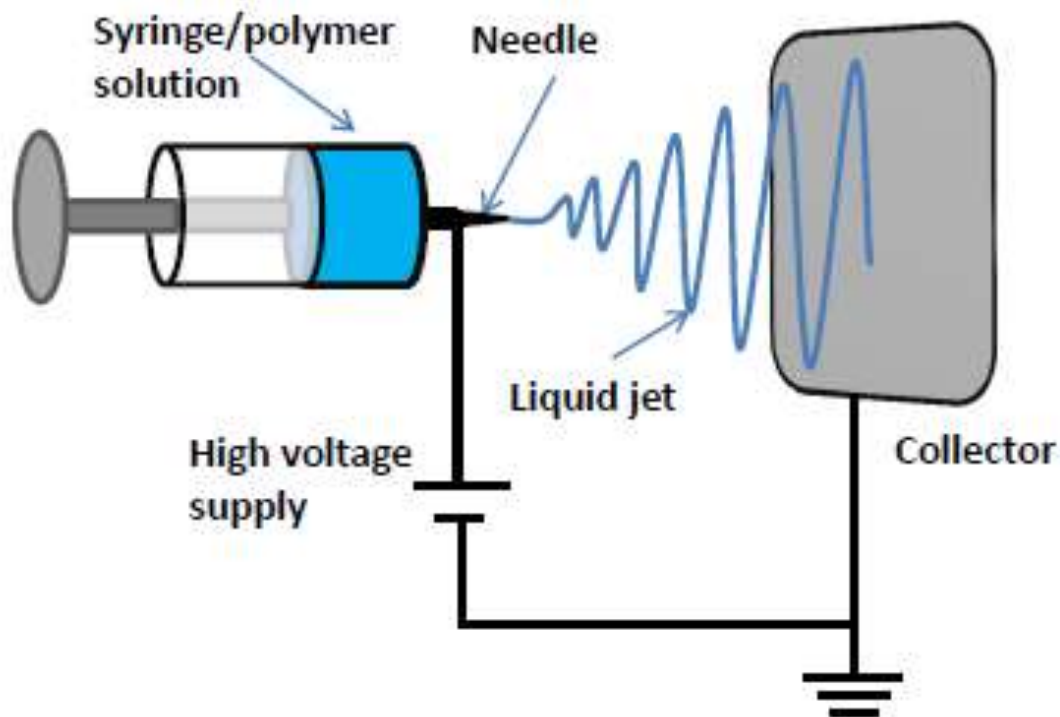
Figure 2.5. Schematic of a classic needle-based electrospinning setup.

It is noteworthy that the process of electrospinning is very complicated, and it involves multiple physical phenomena such as electrohydrodynamics, diffusion and transfer of heat, solidification and crystallization, and the process has not yet been completely elucidated. The contemporary theoretical investigations are focused primarily on jet initiation (Taylor, 1964 and 1969; Spivak and Dzenis, 1999; Yarin et al., 2001), slender jet behavior (Kirichenko et al., 1986; Spivak and Dzenis, 1998; Spivak et al., 2000; Shin et al., 2001; Hohman et al., 2001; Feng, 2002 and 2003; Fridrikh et al., 2003) and straight jet destabilization (Kirichenko et al., 1986; Spivak and Dzenis, 1998; Reneker et al., 2000; Spivak et al., 2000; Hohman et al., 2001; Yarin et al., 2001) as reviewed recently by Reneker et al. (2007). Among these, to understand the whipping/bending instability of an electrospinning jet, Hohman et al. (2001) developed a linearized destabilization model to determine the critical condition of jet instability (i.e., the axisymmetric and asymmetric

29

modes). This model has been used to predict the jet destabilization wavelength once the whipping/bending of a jet occurs, and has also been considered to correlate the final nanofiber diameter to the processing and material parameters (Fridrikh et al., 2003). In parallel, Reneker et al. (2000) formulated an efficient bead model to elucidate the whipping/bending instability of the jet in electrospinning. In this model, the jet is treated as a chain of beads (mass particles), each of which is connected through two neighboring one-dimensional (1D) spring-dashpot elements based on the Maxwellian viscoelastic model with varying viscosity according to the extent of solvent evaporation. By further taking into account the effect of solvent evaporation, Yarin et al. (2001) refined this model to predict the jet trajectory at a distance up to 10 cm from the spinneret as largely validated by their experimental observations. To date, numerous experimental and modeling studies have been carried out for understanding the fundamental electrohydrodynamic phenomena involved in the electrospinning process and the properties of the resulting nanofibres; these include the recent studies on controllable nanofiber production, jet solidification and mechanical properties of electrospun nanofibers, among others (Wu and Dzenis, 2005 and 2007; Thompson et al., 2007; Lim et al., 2008; Wu, 2010; Wu et al., 2011; Wu et al., 2013; Wu and Yarin, 2013).
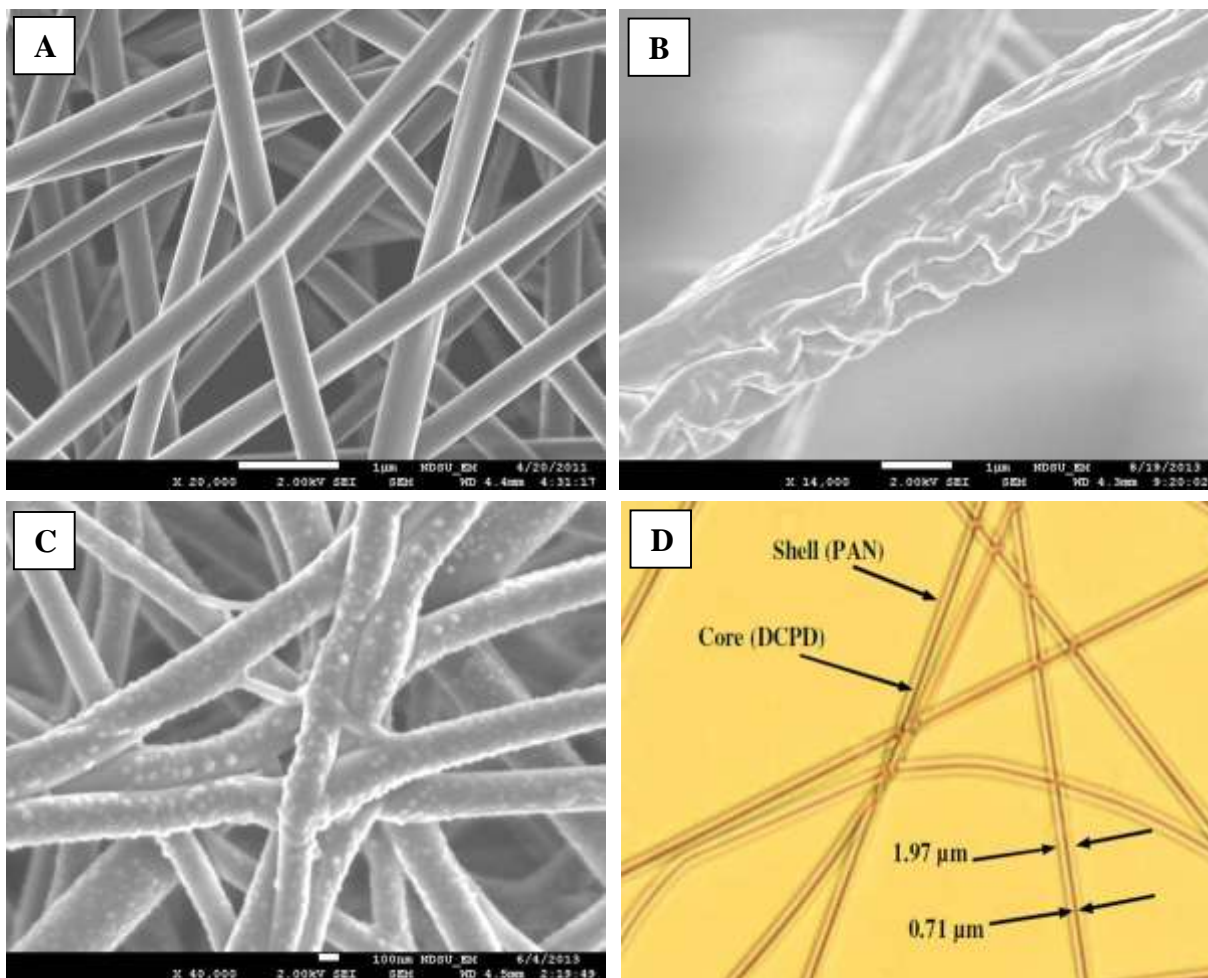
Figure 2.6. Electrospun nanofibers with controlled morphologies. A: Smooth PAN nanofibers, B: Rough polystyrene (PS) fibers, C: Poly (vinyl alcohol) (PVA)/soy protein nanofibers coated with silver nanoparticles, D: Core-shell dicyclopentadiene (DCPD)/PAN nanofibers, E: Graphene-beaded CNFs, F: Graphene-beaded CNFs coated with Ni nanoparticles, G: CNTs grown on the surface of CNFs, H: Needle-like PANI nanorods grown on the surface of CNFs (Synthesized for this thesis research).
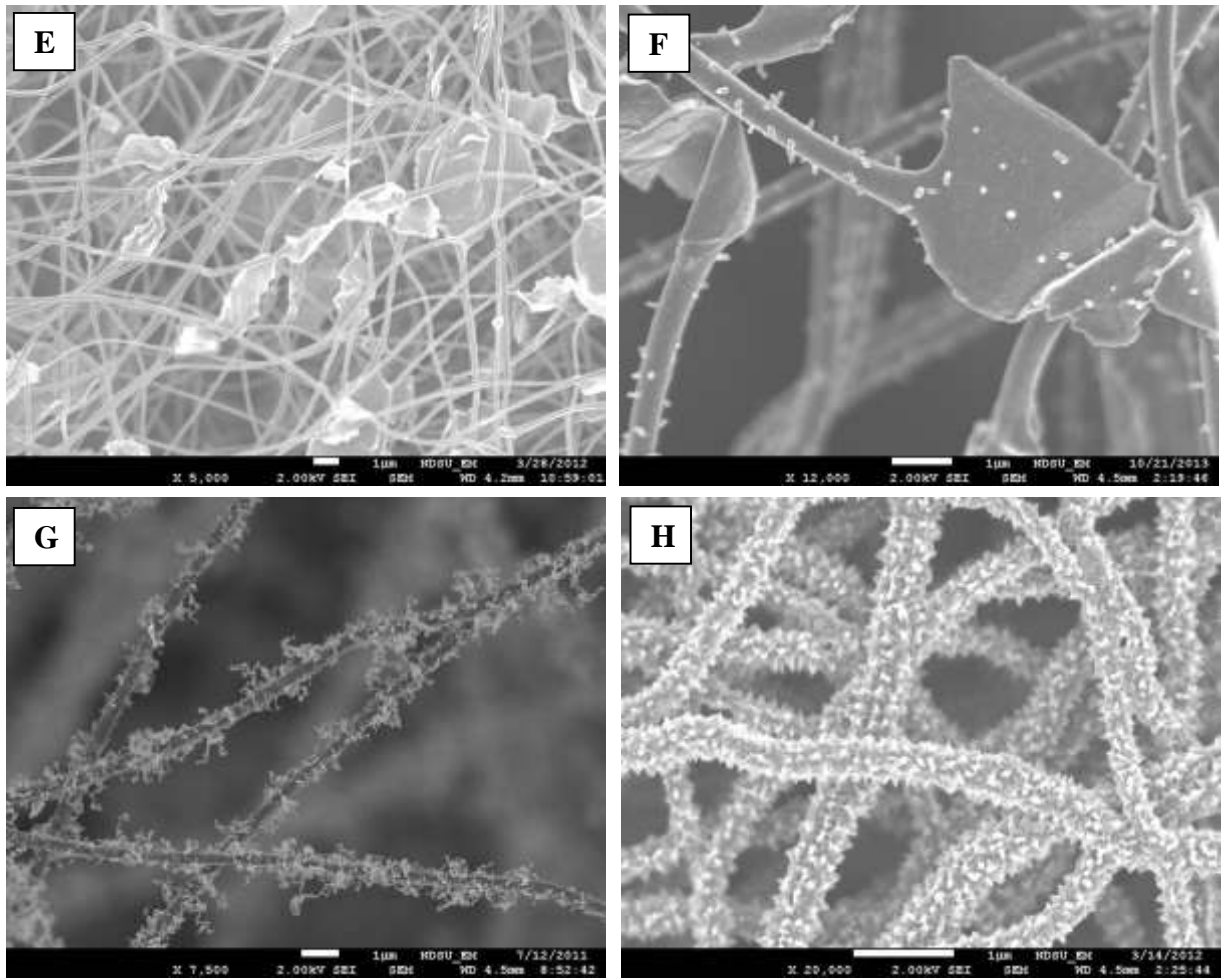
Figure 2.6. Electrospun nanofibers with controlled morphologies (continued). A: Smooth PAN nanofibers, B: Rough polystyrene (PS) fibers, C: Poly (vinyl alcohol) (PVA)/soy protein nanofibers coated with silver nanoparticles, D: Core-shell dicyclopentadiene (DCPD)/PAN nanofibers, E: Graphene-beaded CNFs, F: Graphene-beaded CNFs coated with Ni nanoparticles, G: CNTs grown on the surface of CNFs, H: Needle-like PANI nanorods grown on the surface of CNFs (Synthesized for this thesis research).

2.7.2. Needleless electrospinning

As a matter of fact, the productivity of single-needle-based electrospinning is very low, largely a few grams per day, which could not satisfy the demand of any practical applications. To date, substantial research effort has been devoted to enhancing the manufacturing productivity of nanofibers, such as adopting multiple spinnerets and utilizing destabilization of a thin layer of

immiscible polymer solution based on the principle of needleless electrospinning (Yarin and Zussman, 2004; Wu and Dzenis, 2005; Theron et al., 2005; Reneker et al., 2007; Lukas et al., 2008 and 2009; Miloh et al., 2009; Forward et al., 2013), i.e., free-surface electrohydrodynamic jetting (as shown in Fig. 2.7). However, such an approach may encounter technical difficulties because initiation of multiple jets from a thin dielectric liquid layer depends upon its electrohydrodynamic destabilization in electrostatic field. The wavelength of such an electrohydrodynamic destabilization highly relies on the surface (interface) tension, dielectric constant, mass density, and thickness of a thin liquid layer (Theron et al., 2005; Wu and Dzenis, 2005; Zhou et al., 2014).
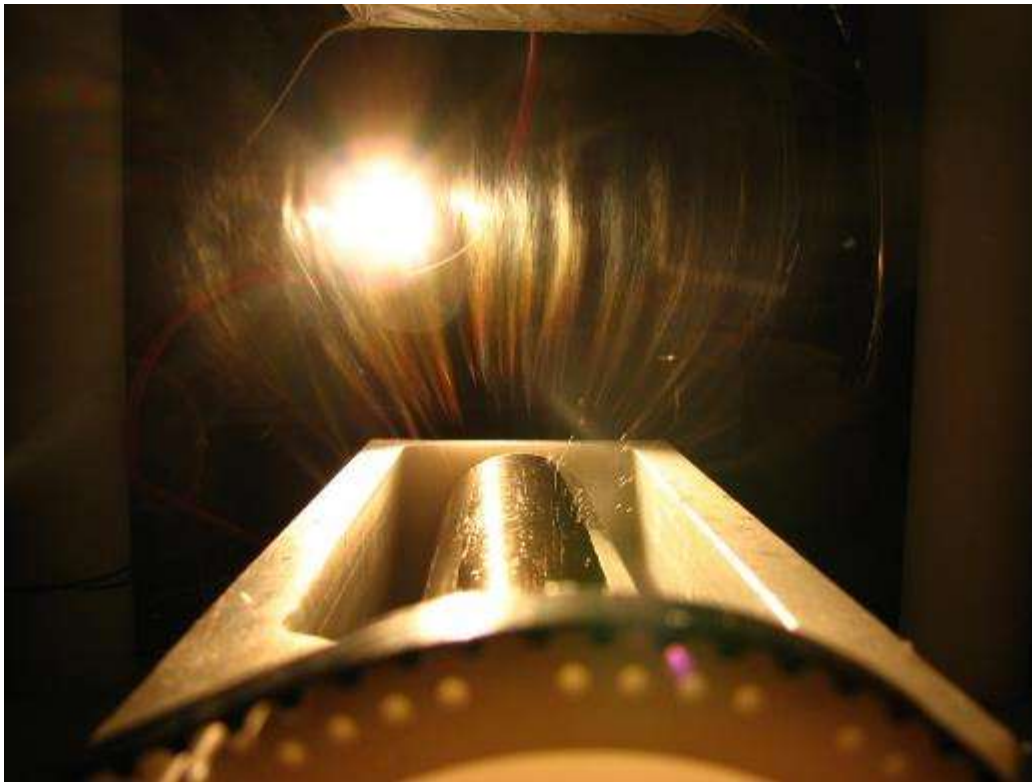
Figure 2.7. Multiple jets from a rotating drum of a lab-made needleless electrospinning device for continuous PEO nanofibers fabrication (The device was designed by a senior design group mentored by Drs. Wu and Akhatov at NDSU).

Among others, in recent years, Lukas and his coworkers made the technical breakthrough in needleless electrospinning technology by using free-jetting of a thin liquid layer formed on a

rotating drum (as shown in Fig. 2.7) (Sarkar and Lukas, 2007; Lukas et al., 2008 and 2009; Petrick and Maly, 2009). Such a technical breakthrough directly led to the Nanospider™, a robust and efficient needleless electrospinning device commercialized successfully by Elmarco, Inc, a world-leading company focusing on fabrication and commercialization of needleless-electrospinning machines for mass production of nonwoven nanofibers for various industry-level uses. Elmarco has provided over one hundred of Nanospider™ machines to companies and universities for mass fabrication of high quality nanofibres in the United States.

2.7.3. Co-electrospinning

The classic electrospinning technique has also been extended to produce core-shell and hollow nanofibers by replacing the single needle (nozzle) with a coaxial spinneret, i.e., co-electrospinning (Sun et al., 2003; Li et al., 2004; McCann et al., 2005; Moghe and Gupta, 2008; Sinha-Ray et al., 2012), in which two polymer solutions are infused into the interior and exterior nozzles to form the core and shell materials, respectively. In addition, co-electrospun core-shell nanofibers can be further converted into hollow nanofibers via extracting or thermal decomposition of the core material (Li et al., 2004). Continuous core-shell and hollow nanofibers can be potentially used for gas and liquid transport, drug delivery, electrode materials of supercapacitors and rechargeable batteries, encapsulation of healing agent for self-repairing composites (Sinha-Ray et al., 2012; Wu et al., 2013; Wu and Yarin, 2013), etc. In addition, core-shell nanofibers can also be produced by means of single-needle-based emulsion electrospinning (Xu et al., 2006; Bazilevshy et al., 2007; Yarin, 2011; Zhou et al., 2014). During this process, the core and shell materials are first dissolved separately into proper solvents to form two immiscible or less-miscible solutions. Proper mixture of the two resulting solutions leads to an

electrospinnable emulsion. Upon electrospinning of the emulsion, droplets of one solution of the emulsion are encapsulated into the second one inside the electrospinning jet, deformed, and elongated, and consequently form the core of the core-shell fiber. In principle, emulsion electrospinning can be utilized for producing a variety of core-shell and hollow nanofibers based on the conventional electrospinning setup with a single spinneret (nozzle), although appropriate preparation of an electrospinnable emulsion is required.

Nevertheless, if applying needleless electrospinning to massively produce core-shell nanofibers based on destabilization of two immiscible solution layers, it is challenging to simultaneously tune the parameters of two liquid layers (e.g., thickness) such that destabilization of two immiscible liquid layers takes place with very close wavelengths, which could guarantee the generation of stable core-shell jets. Initiation of multiple jets due to destabilization of either the top or bottom liquid layer can be expected; however, in such a case, destabilization of the second liquid layer could be suppressed due to the different destabilization conditions. Therefore, new techniques for scale-up fabrication of ultrathin core-shell fibers are still desired in order to satisfy the ever-growing demand of core-shell fibers for broad applications in biomedical, industrial, and other sectors.

CHAPTER 3. FABRICATION AND ELECTROCHEMICAL BEHAVIOR OF CARBON NANOFIBERS SURFACE-GROWN WITH CNTS

3.1. Introduction

One-dimensional (1D) CNTs carry high electrical conductivity and specific surface area, due to their unique tubular graphene nanostructure. However, when CNTs are integrated into electrodes for use in supercapacitors and rechargeable batteries, their discrete nature and electrical contact resistance (ECR) directly influence the effective electrical and electrochemical performances of the electrodes. In view of this concern, in this chapter, a recently reported innovative rational synthesis route (Lai et al., 2008) was adopted and modified for fabrication of continuous hierarchical CNFs surface-grown with CNTs (CNT/CNFs) for first use as flexible, porous electrode materials of electrochemical supercapacitors. This rational synthesis consisted of electrospinning the precursor polymer nanofibers, followed by controlled carbonization, and CNT growth via chemical vapor deposition (CVD) in a reaction furnace. Prototype solid-state supercapacitors were fabricated with the porous hierarchical CNF films as symmetric electrodes and a thin layer of PVA/H_3PO_4 (10 wt. %) as polymer electrolyte. The electrochemical behavior of the solid-state supercapacitor was characterized using cyclic voltammetry (CV) and galvanostatic charging/discharging (GCD) tests on a BT-2000 Battery tester (Arbin Instruments, TX). Experimental results showed that the specific capacitance of the porous CNF electrodes was up to 185 F/g at the discharge current density of 625 mA/g and the specific capacitance of 114 F/g can be maintained even at a high discharge current density up to 2.5 A/g. SEM and TEM were used to characterize the morphology and structure of the porous CNF electrodes. The excellent connectivity of the synthesized continuous hierarchical CNF networks resulted in the low intrinsic

contact electric resistance of the supercapacitors; the ultrahigh specific surface area and related unique nanostructures are responsible for the high electrochemical properties of the novel continuous hierarchical CNFs as measured in this study.

3.2. Experimental

3.2.1. Materials

In this study, polyacrylonitrile (PAN, Mw = 150,000) and N, N-dimethylformamide anhydrous (DMF, 99.0%) were used for electrospinning the precursor polymer composite nanofibers. Nickel (II) acetylacetonate [$Ni(AcAc)_2$, 95.0%] was dissolved in the PAN/DMF solution as catalyst after thermal decomposition in the as-electrospun nanofibers for the growth of CNTs on carbonized electrospun nanofibers. PVA (Mw = 130,000, 99% hydrolyzed) and H_3PO_4 were utilized to prepare the gel electrolyte of PVA/H_3PO_4 solution. All the chemicals above were purchased from Sigma-Aldrich, Corp. (St. Louis, MO). In addition, copper sheets purchased from McMaster-Carr (Elmhurst, IL) were used as the current collectors in the electrodes. All the materials were used as received without further purification or change.

3.2.2. Preparation of PAN/$Ni(AcAc)_2$/DMF solution for electrospinning

The electrospinnable PAN/$Ni(AcAc)_2$/DMF solution was prepared using the following route. As-received $Ni(AcAc)_2$ was first dispersed in DMF solvent by bath sonication for 1 hour at room temperature. PAN powder was dissolved in DMF to prepare 15 wt. % PAN/DMF solutions. Then, the $Ni(AcAc)_2$/DMF solution was added into the 15 wt. % PAN/DMF solution to achieve a solution with the concentrations of 13 wt. % PAN and 5 wt. % $Ni(AcAc)_2$ in DMF, respectively.

The solution was further stirred for 24 h at room temperature, resulting in uniform PAN/Ni(AcAc)$_2$/DMF solution before electrospinning.

3.2.3. Electrospinning precursor PAN/ Ni(AcAc)$_2$ nanofibers

The experimental setup for electrospinning is schematically shown in Fig. 2.4. The PAN/ Ni(AcAc)$_2$/DMF solution was placed into a 10 ml plastic syringe installed with a blunt-ended stainless steel needle as spinneret, which had an inner diameter of 0.48 mm. The spinneret was connected to a positive high-voltage DC power supply with adjustable voltage that was purchased from the Gamma High Voltage Research, Inc. (Ormond Beach, FL). A laboratory- made aluminum rotary plate as the nanofiber collector with a diameter of 33 cm was placed 20 ∼ 25 cm away from the tip of the spinneret. During electrospinning, a high positive voltage of 15-25 kV was applied to the needle, while a high negative voltage of 2-10 kV [provided by another negative high-voltage DC power supply that was purchased from the Gamma High Voltage Research, Inc. (Ormond Beach, FL)] was applied to the aluminum rotary plate. The flow rate of the electrospun solution was set at 1.0-1.5 ml/h using a syringe pump (model number: KDS 200) purchased from the KD Scientific Inc. (Holliston, MA). After electrospinning, a nonwoven nanofiber film of randomly oriented electrospun PAN/Ni(AcAc)$_2$ nanofibers was obtained and peeled off from an aluminum foil attached onto the aluminum rotary plate. The as-electrospun nanofiber films were dried at 100 °C in oven for 6 h prior to the stabilization treatment.

3.2.4. Stabilization and carbonization of PAN/Ni(AcAc)$_2$ nanofibers and CVD for CNT growth

Controlled stabilization and carbonization of as-electrospun PAN/Ni(AcAc)$_2$ nanofiber films were performed in a tubular furnace (Atomate, Inc., Santa Barbara, CA). For oxidative stabilization of PAN, the electrospun nanofiber films were first heated in air to 215 °C at a heating rate of 1°C/min followed by holding the temperature at 215 °C for 1 h.

During the process of carbonization, the as-stabilized PAN/Ni(AcAc)$_2$ nanofiber films were heated in Ar to 500 °C at a rate of 5 °C/min; subsequently, the carbonized composite nanofibers were treated at 500 °C for 1 h in a mixture flow of H$_2$ and Ar (H$_2$/Ar = 1/2) for the reduction of Ni^{2+} ions into Ni atoms, which diffused to the surface of the nanofibers and agglomerated into Ni nanoparticles. The size of the resulting Ni nanoparticles can be controlled via adjusting the temperature and duration of the process similar to that based on other catalytic metal as reported in the literature (Lai et al., 2008). After that, the samples were heated to 650 °C at a rate of 5 °C/min in an Ar flow and kept at this temperature; the Ar flow was then replaced with the mixture flow of Ar and C$_2$H$_4$ (Ar/C$_2$H$_4$ = 1) to grow carbon nanostructures (*i.e.*, multi-walled CNTs). After reaction for 1 h, the C$_2$H$_4$ gas was turned off. Then the furnace was cooled down to the ambient temperature. After the above treatments/reactions, the electrospun PAN/Ni(AcAc)$_2$ nanofibers were converted into hierarchical porous CNFs surface-grown with multi-walled CNTs (MWCNTs).

3.2.5. Electrode preparation and electrochemical characterization

The prototype solid-state supercapacitors were fabricated based on the above hierarchical porous CNFs surface-grown with Ni nanoparticles and CNTs using a symmetrical two-electrode

cell setup (see Fig. 3.1). During the fabrication, a thin layer of polymer electrolyte made of PVA and H_3PO_4 (10 wt. %) was sandwiched between two patches of the CNF samples with the thickness of ~200 μm, which functioned as the two electrodes of the prototype supercapacitors (Kaempgen et al., 2009; Sung et al., 2006). In addition, a thin PAN nanofiber film was used as the separator to isolate the two CNF electrodes. Two copper foils were used to cover the CNF electrodes as the current collectors of the supercapacitors.

Figure 3.1. Schematic of a solid-state supercapacitor.

The electrochemical capacitive behavior and specific capacitance of the solid-state supercapacitors were characterized on a battery tester BT-2000 (Arbin Instruments, TX) available in the Center for Nanoscale Science and Engineering (CNSE) at NDSU, from which the corresponding characteristic CV and GCD curves were recorded. In the constant current charging/discharging measurement, the symmetrical two-electrode cell was charged and discharged between 0 to 0.8 V in the PVA and H_3PO_4 (10 wt.%) electrolyte. The current densities used in the test were 625, 1250, 1875, and 2500 mA/g, respectively. Scanning rates of 5, 10, 30, and 50 mV/s in the potential range of 0 to 0.8 V were utilized in the CV measurements. By analyzing the CV diagrams and GCD curves, the specific capacitance, energy density, power

density, cycling stability, and electrical resistance of the solid-state supercapacitors were calculated using the relations (2.4)-(2.6) in Chapter 2.

3.2.6. Morphology and microstructure characterization

The surface morphologies of the as-electrospun, stabilized, and carbonized nanofibers were analyzed by using a field-emission scanning electron microscope (SEM, JEOL JSM-7600F). Prior to SEM examination of the as-electrospun and stabilized nanofibers, these nanofiber specimens were sputter-coated with carbon to avoid charge accumulations. A transmission electron microscope (TEM, JEOL JEM-2100) was further employed to characterize the carbonaceous microstructures of the carbonized CNF specimens. Before TEM characterization, the specimens were dispersed by sonication in acetone, and the resulting solution mixture was dropped onto lacey carbon films supported on a copper grid. In addition, the microstructures and structural conversion of the carbonized nanofibers were investigated by a laser confocal Raman Spectrometer (Nicolet NXR 9650 FT-Raman spectrometer, 632.8 nm) and a Siemens D5000 X-ray diffractometer (XRD). The X-ray tube operating at 40 kV and 44 mA with the CuKα radiation (wavelength $\lambda = 0.154$ nm) was used; and the XRD profiles were recorded with the 2θ angles ranging from 5 ° to 60 ° at the scanning speed of 5 °/min.

3.3.   Results and Discussions

3.3.1.   Morphology and structure characterization

SEM micrographs shown in Figs. 3.2 (A-D) show the representative morphologies of the as-electrospun PAN nanofibers, PAN/Ni(AcAc)$_2$ nanofibers, carbonized electrospun PAN nanofibers, and carbonized PAN/Ni(AcAc)$_2$ nanofibers, respectively. Both the PAN and

PAN/Ni(AcAc)$_2$ precursor nanofibers in the as-electrospun nanofiber mats exhibited uniform and smooth morphology without identifiable microscopic beads and/or beaded nanofibers. These nanofibers have an average diameter in the range of 400-500 nanometers. After carbonization of the precursor as-electrospun PAN nanofibers at 650 °C, the average diameter was reduced to about 300 nm. During carbonization of PAN/ Ni(AcAc)$_2$ nanofibers at 500 °C for 1 h in a mixture flow of H$_2$ and Ar (H$_2$/Ar = 1/2) , the Ni^{2+} ions were reduced into elemental Ni, which further aggregated into nanoparticles on the surface of nanofibers (Lai et al., 2008; Zhou et al., 2012) as shown in Fig. 3.2 (D).
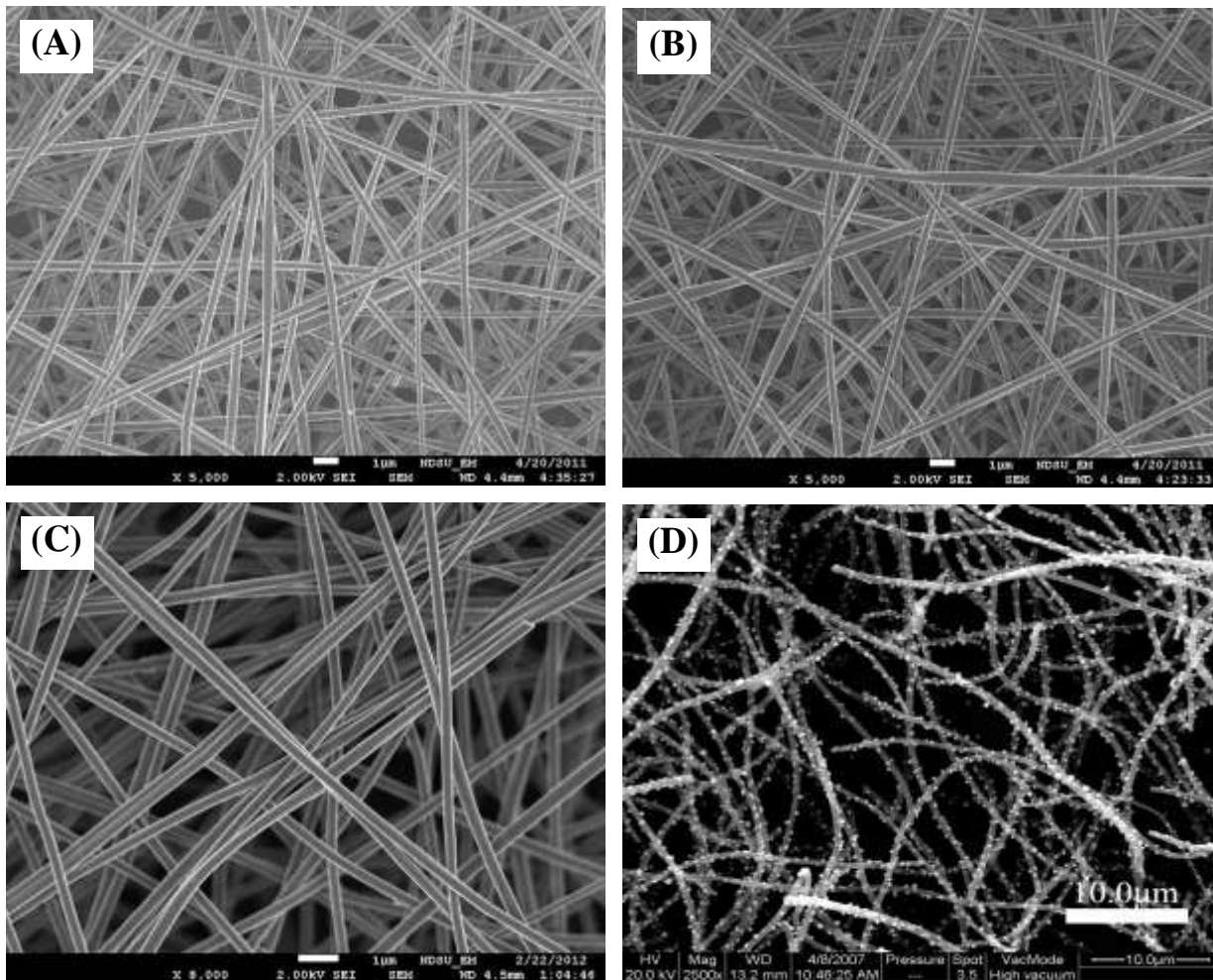
Figure 3.2. SEM micrographs of (A) PAN and (B) PAN/Ni(AcAc)$_2$ nanofibers; SEM micrographs of (C) carbonized electrospun PAN nanofibers and (D) electrospun CNFs surface-grown with Ni nanoparticles.

In principle, the major factors that influence the capacitance of electric double-layer capacitors (EDLCs) are the specific surface area and electrical conductivity of the electrodes. Tubular carbon nanostructures such as CNTs and CNFs provide a high electrical conductivity and a large specific surface area. Thus, the present process to grow tubular carbon nanostructures onto the surface of carbonized electrospun PAN nanofibers is expected to enhance the specific surface area and electrical conductivity of the resulting electrode materials. At the reaction condition of 650 °C in H$_2$/Ar atmosphere, reduction of Ni^{2+} ions and formation of Ni nanoparticles on the CNF

surface can be evidenced in the TEM micrograph (Fig. 3.3A). The Ni nanoparticles agglomerated on the surface in nearly uniform morphology with the sizes of 10-30 nm. The C_2H_4 gas was carried into the tubular reaction furnace and decomposed into carbon atoms, which deposited on the surface of Ni nanoparticles, where tubular nanostructures in terms of multi-walled CNTs grew consequently on the electrospun CNFs (Lai et al., 2008). The TEM micrograph (Fig. 3.3B) clearly shows the growth of tubular carbon nanostructures on CNFs. Theses tubular carbon nanostructures carried the graphene shells with the outer diameters of ~20-40 nm and the lengths of several microns. The diameter and length of the tubular carbon nanostructures could be tailored by adjusting the temperature and duration of the reaction (Ziebro et al., 2010). In addition, Ni nanoparticles could also be identified at the tip or middle locations of carbon nanostructures due to the different growth mechanisms. The presence of Ni nanoparticles in the tubular carbon nanostructures and CNFs could be advantageous, because such a hybrid system consisted of both pseudocapacitive nanoparticles of metals or metal oxides and conventional capacitive carbon.
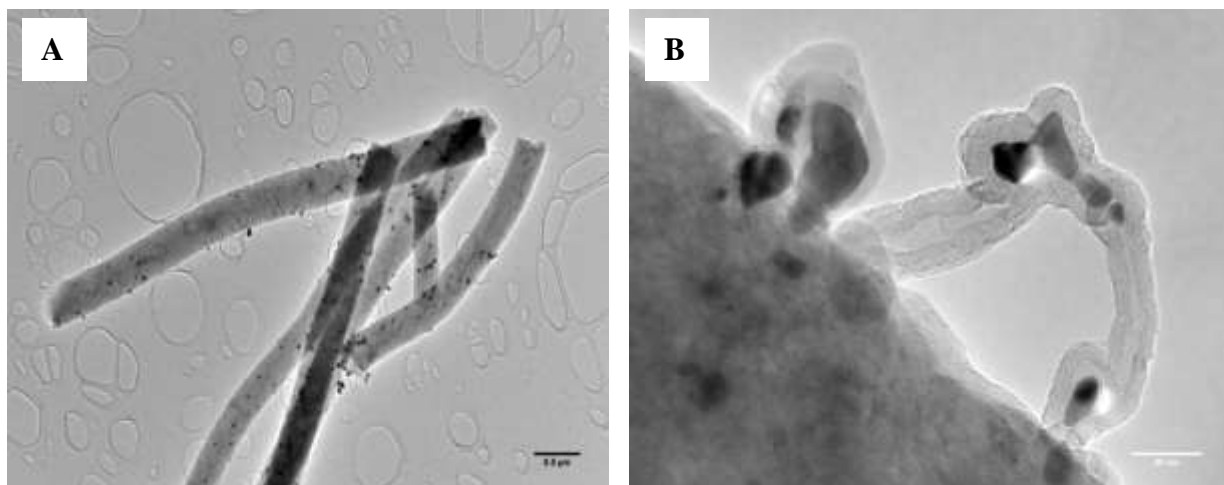
Figure 3.3. TEM micrographs of Ni nanoparticles on the electrospun CNFs (A) and tubular carbon nanostructures embedded with Ni nanoparticles at the surface of a CNF (B).

During the pyrolysis process inside the tubular furnace at 650 °C, the Ni atoms inside the CNFs diffused onto the CNF surface and aggregated into Ni nanoparticles, which functioned as catalyst for the growth of carbon nanostructures. Figure 3.4 shows the SEM micrographs about the growth of CNTs on the surface of CNFs with varying durations of C_2H_4 supply of (A) 2 min, (B) 10 min, (C) & (D) 30 min, and (E) & (F) 60 min, respectively. It can be found that the length of the CNTs depended on the duration of C_2H_4 supply. The longer is the supply duration of C_2H_4, the larger is the length of CNTs (Lai et al., 2008). The lengths of CNTs under this study were controlled in the range of several nanometers to micrometers.
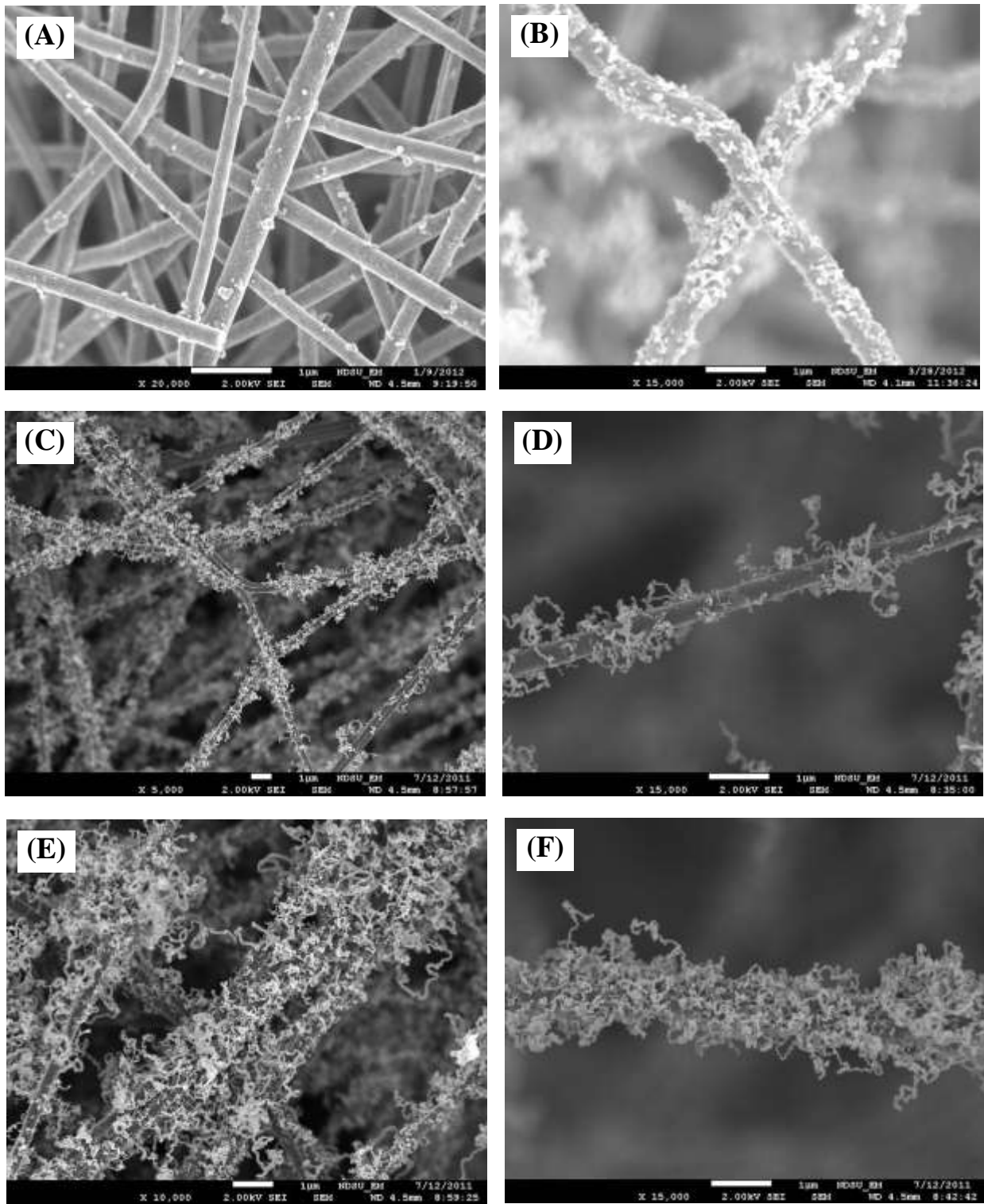
Figure 3.4. SEM micrographs of hierarchical porous CNT/CNFs at varying duration of C_2H_4 supply. The duration of C_2H_4 supply: (A) 2 min, (B) 10 min, (C) & (D) 30 min, and (E) & (F) 60 min.

The crystalline structures of CNFs and Ni/CNT/CNFs at the process temperature of 650

°C were analyzed by the X-ray diffraction with the 2θ values lying between 5° and 60°, as shown

in Fig. 3.5. The XRD pattern of as-prepared Ni/CNT/CNFs shows two characteristic peaks at 2θ

angles of ~44.7° and 52.6° corresponding to the (111) and (200) reflection position of Ni (Geng et

al., 2007; Kumar et al., 2013), respectively. These diffraction peaks indicated that the Ni

nanoparticles were a single fcc phase without significant oxides or other impurity phases (Geng et

al., 2007; Kumar et al., 2013). Additionally, the pattern shows a typical intense peak of carbon or

graphite materials at 2θ angles of ~25°, which was attributed to the crystallographic plane (002)

(Zhou et al., 2009 and 2010). Compared to pure CNFs without a clear 2θ peak (~25°),

Ni/CNT/CNFs demonstrated an obvious peak and more ordered in structure and well crystallized.
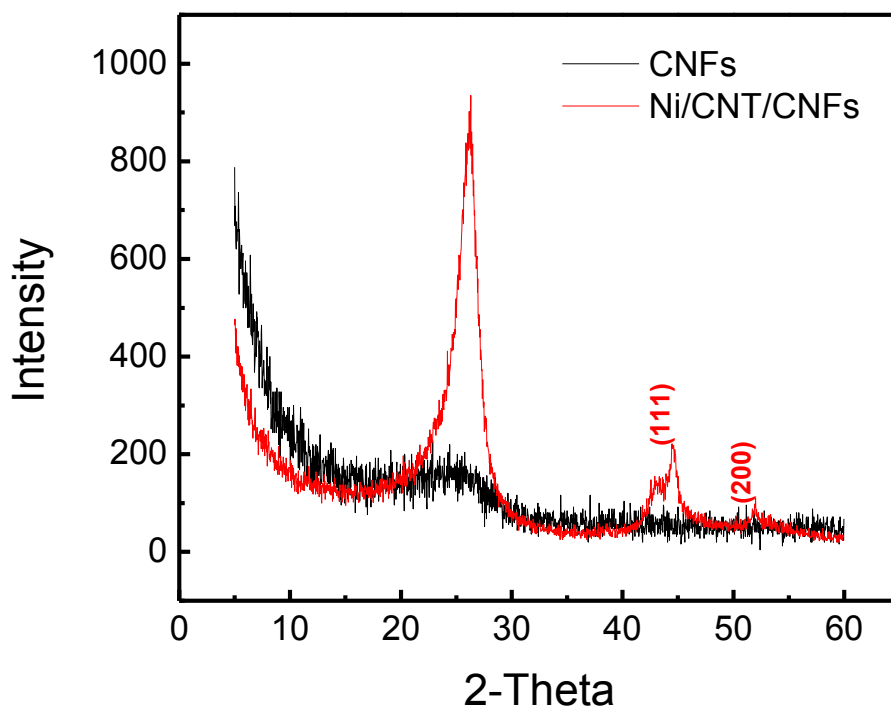
Figure 3.5. X-ray diffraction patterns of CNFs and Ni/CNT/CNFs at the process temperature of
650 °C, respectively.

3.3.2. Electrochemical characterization

3.3.2.1. *CV measurements*

The electrochemical behavior of the hierarchical porous CNT/CNF electrodes was characterized in a gel electrolyte of PVA and 10 wt. % H_3PO_4 by CV. Figure 3.6 depicts the typical CV curves of the electrodes at various scanning rates (e.g., 5, 10, 30, and 50 mV/s). At the low scanning rates (e.g., 5 mV/s and 10 mV/s), the shapes of CV curves were nearly rectangular; i.e., the electrodes were stable in the gel electrolyte (see the inserted cyclic CV diagram at scanning rate of 10 mV/s in Fig. 3.6). In contrast, at high scanning rates (e.g., 30 mV/s and 50 mV/s), the CV curves were distorted with oblique angles. This observation indicated the existence of high contact electric resistance between the electrodes and current collectors (Wu et al., 2012). Pseudocapacitive behavior of the Ni nanoparticles was not clearly identified from Fig. 3.6 (i.e., the Ni nanoparticles in this study exhibited the electrochemical behavior similar to that of carbon) (Srinivasan and Weidner, 1997). In principle, the high specific surface area of the electrodes, low volume fraction of Ni nanoparticles, and the well-capsulation of Ni nanoparticles by the surrounding carbon might have shielded the pseudocapacitive effect of the Ni nanoparticles (Srinivasan and Weidner, 1997).
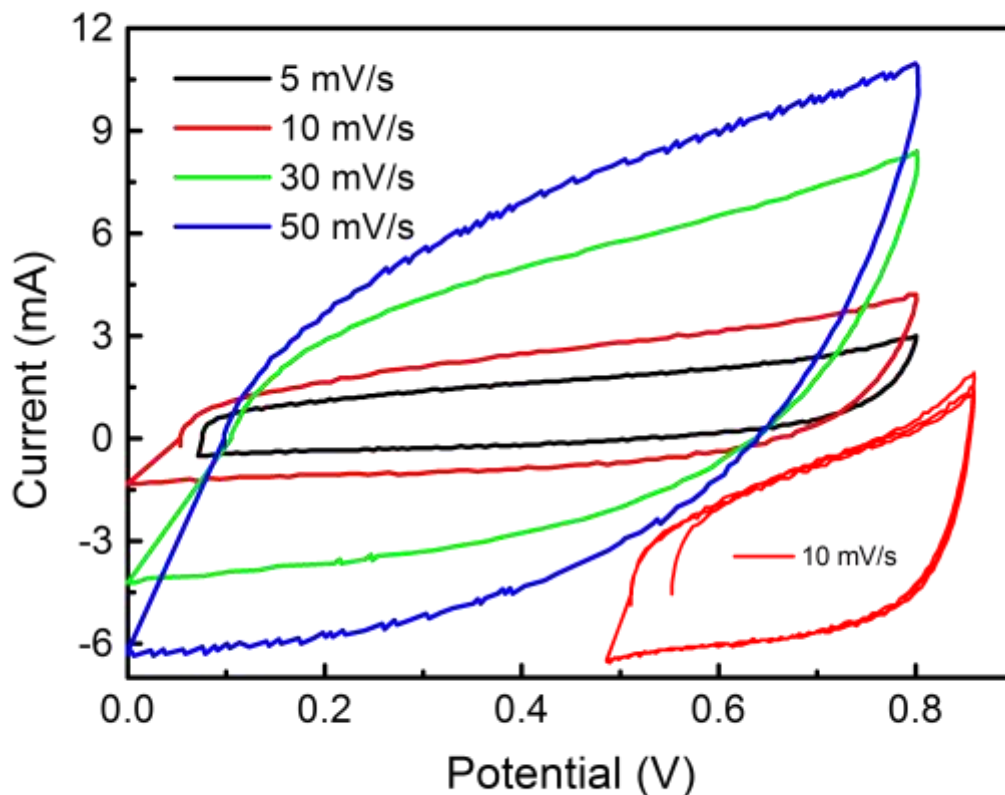
Figure 3.6. CV curves of the hierarchical porous CNF electrodes in the gel electrolyte of PVA and 10 wt. % H_3PO_4 at different scanning rates.

3.3.2.2. GCD measurements

The typical GCD curves of the hierarchical porous CNT/CNF electrodes in the PVA/H_3PO_4 gel electrolyte at 625 and 1,875 mA/g, respectively, are shown in Fig. 3.7. No significant IR drop was detected at a relatively low discharge current of 625 mA/g, reflecting a very low equivalent series resistance (ESR) of the hybrid porous electrodes. The results suggested that the unique connectivity of continuous CNT/CNFs effectively improved the electric conductivity of the hybrid porous electrodes; nonetheless, it was evident that the IR dropped substantially with the increase of discharge current density.
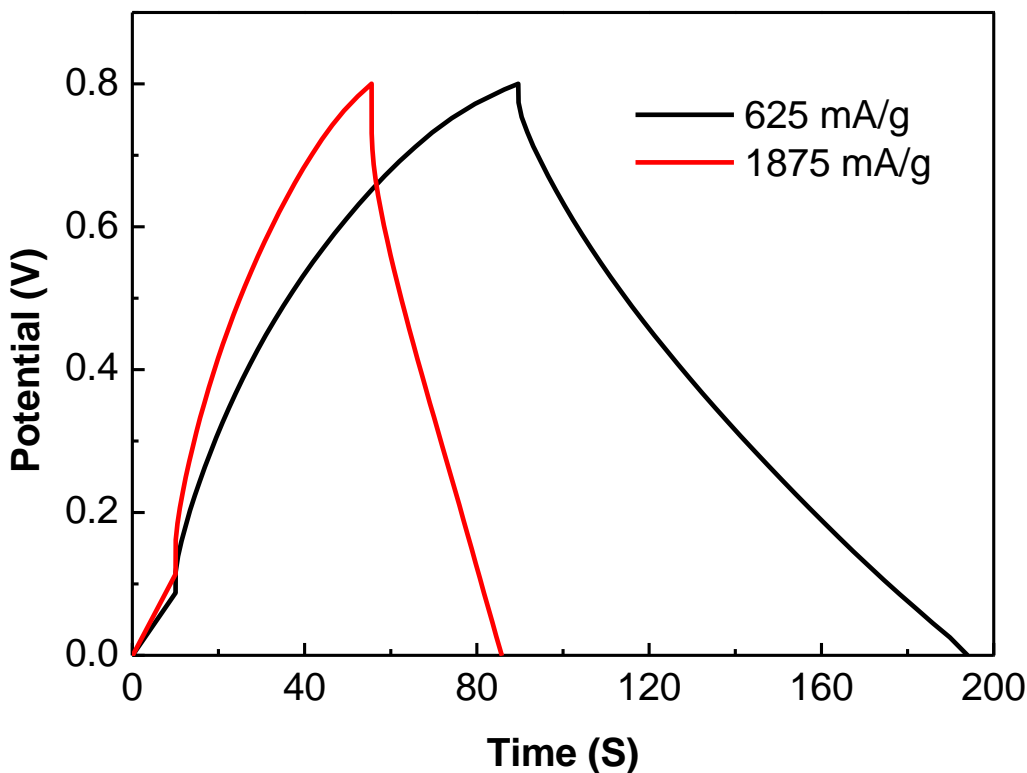
Figure 3.7. GCD curves of the hierarchical porous CNF electrodes in the PVA/H$_3$PO$_4$ gel electrolyte at different discharge current densities.

The specific discharge capacitance of the hierarchical porous CNT/CNF electrodes of supercapacitors can be calculated according to relation (2.4). Figure 3.8 shows the specific capacitance as a function of the discharge current density of the hierarchical porous CNT/CNF electrodes in the PVA/H$_3$PO$_4$ gel electrolyte. The specific capacitance was up to 185 F/g at the discharge current density of 625 mA/g. It is also noticed that the capacitance of the hierarchical porous CNT/CNF electrodes is higher than those reported recently in the literature, including activated carbon nanofiber electrodes (100 F/g at 1 A/g) (Seo and Park, 2009), MWNTs (102 F/g) (Niu et al., 1997), SWNTs (180 F/g) (An et al., 2001), and porous CNF electrodes (140 F/g in 6 M KOH solution) (Kim et al., 2007). Due to the high conductivity and large specific surface area

of the hierarchical porous CNT/CNF electrodes, the specific capacitance values of 114 F/g can be still maintained even at the discharge current density as high as 2.5 A/g. All the experimental results reported in this chapter have been published in *Applied Physics Letters* in 2012 (Zhou et al., 2012).
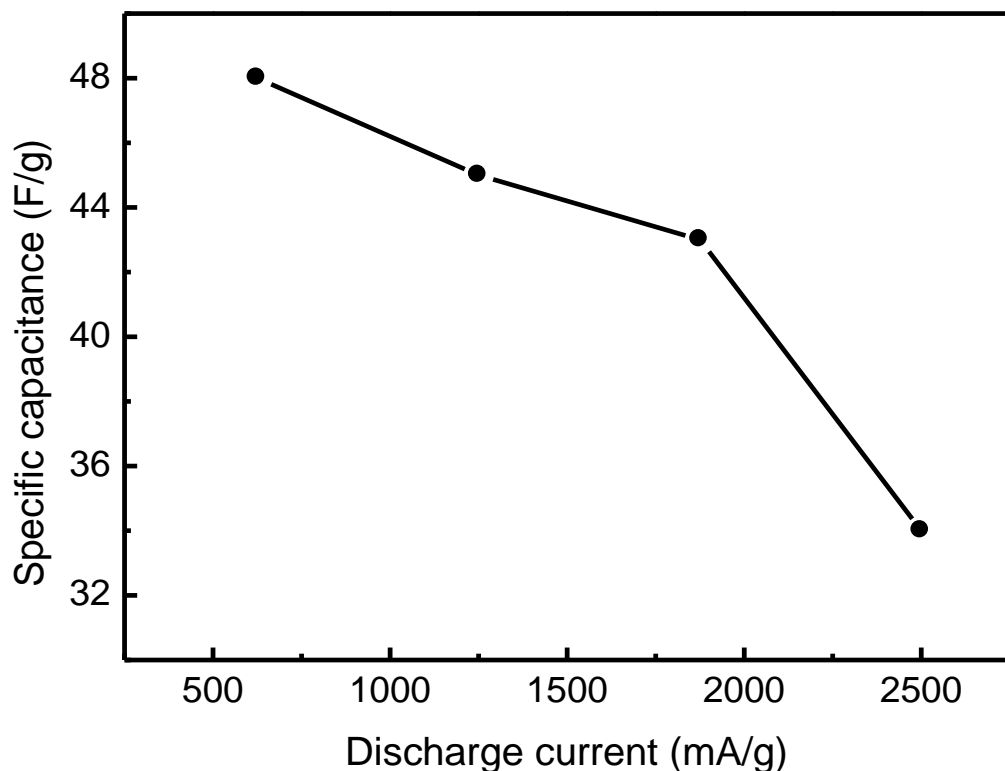
Figure 3.8. Dependence of the specific capacitance on the discharge current density for the hierarchical porous CNT/CNF electrodes in the PVA/H$_3$PO$_4$ gel electrolyte.

3.4.   Summary

Electrospun CNFs surface-grown with CNTs could be a new type of hierarchical porous nanomaterials for design and fabrication of porous electrodes with high specific surface area and superior specific capacitance for use in supercapacitors and pseudocapacitors. The excellent

connectivity and electrical conductivity of the hierarchical porous carbonaceous nanomaterials can provide the low intrinsic contact electric resistance of the supercapacitors. Such hierarchically-structured conductive nanofibrous material also offers an innovative nanostructured template for synthesis of advanced porous multifunctional electrode materials to be discussed in Chapter 4.

CHAPTER 4. TERNARY CORE-SHELL STRUCTURED CARBON NANOFIBERS SURFACE-GROWN WITH CNTS AND POLYANILINE AS MULTIFUNCTIONAL ELECTRODES FOR USE IN PSEUDOSUPERCAPACITORS

4.1.   Introduction

As reviewed in Chapter 1, conducting polymers have been under intensive research as potential low-cost electrode materials for use in supercapacitors due to their large pseudocapacitance, low mass density, and sound environmental stability. Yet, conducting polymer-based pseudocapacitors usually carry relatively low electrical conductivity, poor cyclability, and low power density compared to EDLCs. This chapter studies the synthesis and electrochemical performance of CNFs surface-grown with CNTs and ultrathin PANI layers, termed as PANI/CNT/CNFs, for use as high-performance electrode material for pseudocapacitors. The novel hierarchical multifunctional PANI/CNT/CNF films were successfully synthesized via *in situ* polymerization of aniline on the surface of CNT/CNFs as prepared in Chapter 3. The morphology and microstructure of the PANI/CNT/CNFs were characterized by means of SEM, TEM, and Raman spectroscopy. The electrochemical properties of the new material were analyzed by electrochemical impedance spectroscopy (EIS), cyclic voltammetry (CV), and galvanostatic charge/discharge (GCD) in a 1 M H_2SO_4 electrolyte. Experimental results of the microstructures and electrochemical properties were discussed in detail, and related mechanisms were explored to correlate the electrochemical performance of the novel ternary multifunctional PANI/CNT/CNF films to their unique microstructure.

4.2. Experimental

4.2.1. Materials

Ammonium persulfate (APS), sulfuric acid (H_2SO_4), and aniline monomer were purchased from Sigma-Aldrich Chemical Co. (St. Louis, MO, USA). All the chemicals were used as received without further purification or modification.

4.2.2. Preparation of PANI/CNT/CNF films

The process to synthesize the CNFs surface-grown with CNTs (CNT/CNFs) has been reported in Chapter 3. In this study, the PANI/CNT/CNF films were synthesized by *in situ* polymerization of aniline in the as-synthesized CNT/CNF films as hierarchically nanostructured templates. A solution of 0.03 M aniline in 200 ml 1 M H_2SO_4 was prepared first. The CNT/CNF films were immersed in the solution for 1 h. Then, another 200 ml 1 M H_2SO_4 solution containing 0.0075 M APS was added to the above solution, drop-by-drop. The mixture solution was continuously stirred for 5 h and the aniline polymerized in an ice-bath. The molar ratio of aniline/APS was 4:1. During this period, the color of the solution slowly changed till dark green. After polymerization, the PANI/CNT/CNF films were filtered and washed sequentially with deionized water and acetone. The films were dried in a vacuum oven at 70 °C for 3 h. The PANI content in the PANI/CNT/CNF films was ~50% by weight.

4.2.3. Structural and electrochemical characterization

The surface morphology and structure of the films were analyzed by SEM, TEM, and Raman spectroscopy. The electrochemical properties of the supercapacitor cells were characterized by EIS, CV, and GCD. Three-electrode EIS setup was employed for the impedance

measurements. A saturated calomel electrode was used as the reference electrode. 1 M H_2SO_4 aqueous solution and stainless steel wire mesh were used as the electrolyte and the current collector, respectively. EIS was tested in the frequency range of 10^5-0.01 Hz by using the Electrochemical Multiplexer ECM8 (Gamry Instruments, Inc., PA). The CV and GCD were conducted by using the Arbin BT-2000 testing system (Arbin Instruments, TX) in a 1 M H_2SO_4 electrolyte in the voltage range of -0.2 to 0.8 V. The specific capacitance, energy density, and power density were calculated according to the GCD curves which were recorded at constant current densities. The specific capacitance, C_s (F/g), energy density, E_d (W h/kg), and power density, P_d (kW/kg), delivered by supercapacitors are calculated by relations (2.4-2.6).

4.3.   Results and Discussions

4.3.1. Scheme of synthesis of PANI/CNT/CNFs

The synthesis procedure of the novel ternary core-shell PANI/CNT/CNFs consisted of three sequential processes: the "top-down" electrospinning fabrication, "bottom-up" CVD, and *in-situ* polymerization. As illustrated in Fig. 4.1, the precursor solution was prepared by dissolving $Ni(AcAc)_2$ and PAN powders in DMF, which were used to electrospin $Ni(AcAc)_2$/PAN nanofibers with the diameter around 300 nm (He et al., 2012; Zhou et al., 2013). These nanofibers were converted into continuous CNFs with Ni nanoparticles aggregated at surface via thermal stabilization in open air, carbonization in inert gas environment (Ar), and NiO reduction into Ni in the H_2/Ar environment in a tubular reaction quartz furnace (Zhou et al., 2012; Zhou and Wu, 2013). During the CVD process of CNT growth onto CNFs, ethylene (C_2H_4) was used as carbon source, and Ni nanoparticles were used as catalyst (Zhou et al., 2012). Consequently, *in-situ* polymerization of aniline with synthesized CNT/CNF networks as a porous scaffold for active

sites of aniline resulted in ternary hierarchical core-shell nanofibrous material with PANI coated onto the surface of CNTs and CNFs.
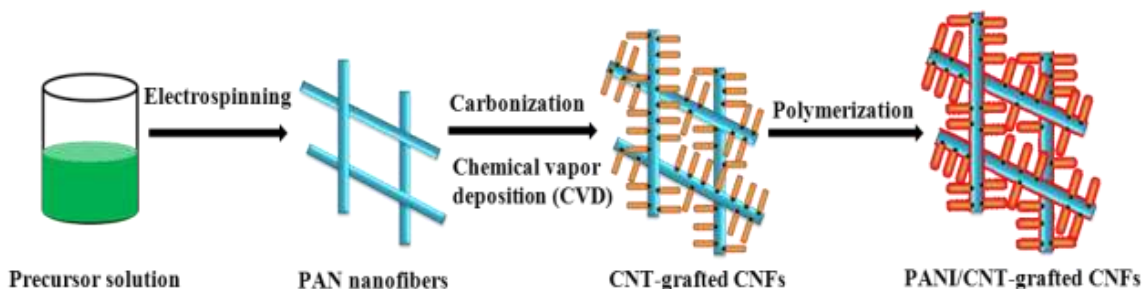
Figure 4.1. Schematic illustration of the rational synthesis process for fabrication of ternary core-shell PANI/CNT/CNF.

The PANI/CNT/CNF films carried several unique features as demanded for use as electrode material of high-performance supercapacitors: 1) the ultrathin PANI layers were deposited onto CNT/CNF networks to enable the fast electron transport and effective current collection (Wang et al., 2011; Wu et al., 2012); 2) the CNF networks were utilized as current collectors and the CNTs coated onto the CNFs functioned as charge channels of the PANI layers, which ensures the high rate charge/discharge capability (Portert et al., 2008, Wu et al., 2012; Chen et al., 2011); and 3) the ultrathin PANI layers carried very high specific surface area and complex surface morphology beneficial to the large specific pseudocapacitance and high energy and power densities. Results of electrochemical characterization demonstrated that the supercapacitors comprising of continuous PANI/CNT/CNF film electrodes exhibited high electrochemical performance and superior cycling stability.

4.3.2. SEM and TEM micrographs of CNFs and CNT/CNFs

During the process of fabricating PANI/discrete carbon nanostructure (e.g., CNTs, graphene, carbon black, etc.) materials, the restacking and aggregation of carbon nanostructures and PANI composites (see Fig. 4.2) directly leads to the decrease of the effective electrical and electrochemical performance and limits the practical applications of the resulting supercapacitors.
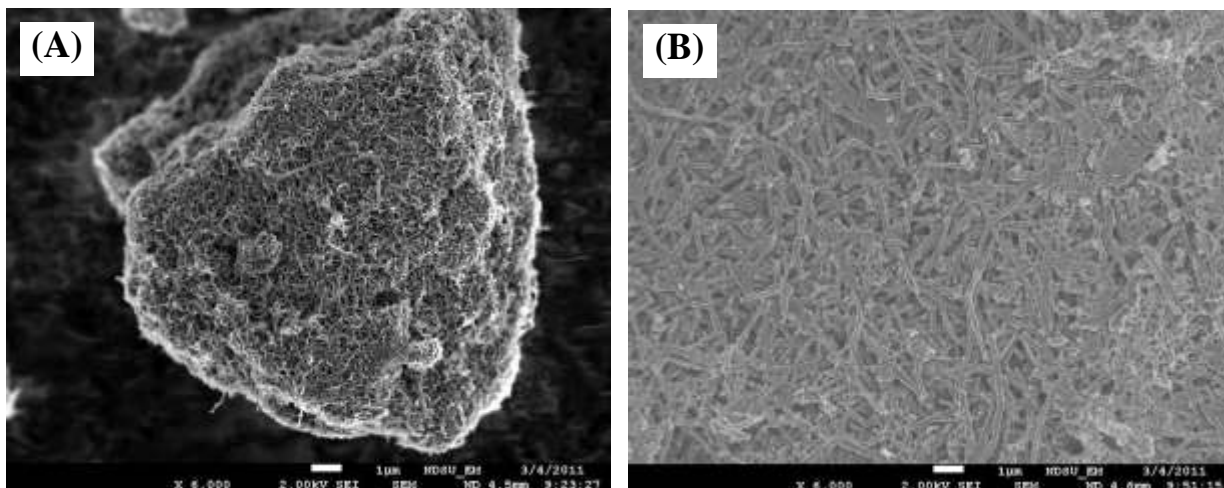
Figure 4.2. SEM micrographs of CNTs (A) and carbon black (B) coated with PANI.

Figures 4.3 (A) and (B) show the typical SEM micrographs of the CNF and CNT/CNF films synthesized in this study, respectively. The CNFs had a smooth surface with a nearly uniform diameter in the range of 200 to 300 nm. From Fig. 4.3 (C), it can be observed that the entangled CNTs with the diameter of 20-30 nm were randomly grown on the surface of CNFs. The length of CNTs was about a few micrometers. The diameter and length of the CNTs can be tailored by adjusting the material and process parameters such as the catalyst, carbon source, temperature, and the duration of the CVD (Lai et al., 2008; Zhou et al., 2012). It can also be founded from Fig. 4.3 (D) that CNFs and CNTs were interconnected, continuous, and not overlapped. Compared to the purified CNFs or CNTs, the present porous CNT/CNF films are expected to have advantages in transporting electrons over a large specific surface area. Furthermore, the CNT/CNF films also

play an important role in reducing CNT agglomeration in the aqueous solution. These results suggest that the CNT/CNF films could act as good templates for formation of the hierarchal porous PANI/CNT/CNF films.
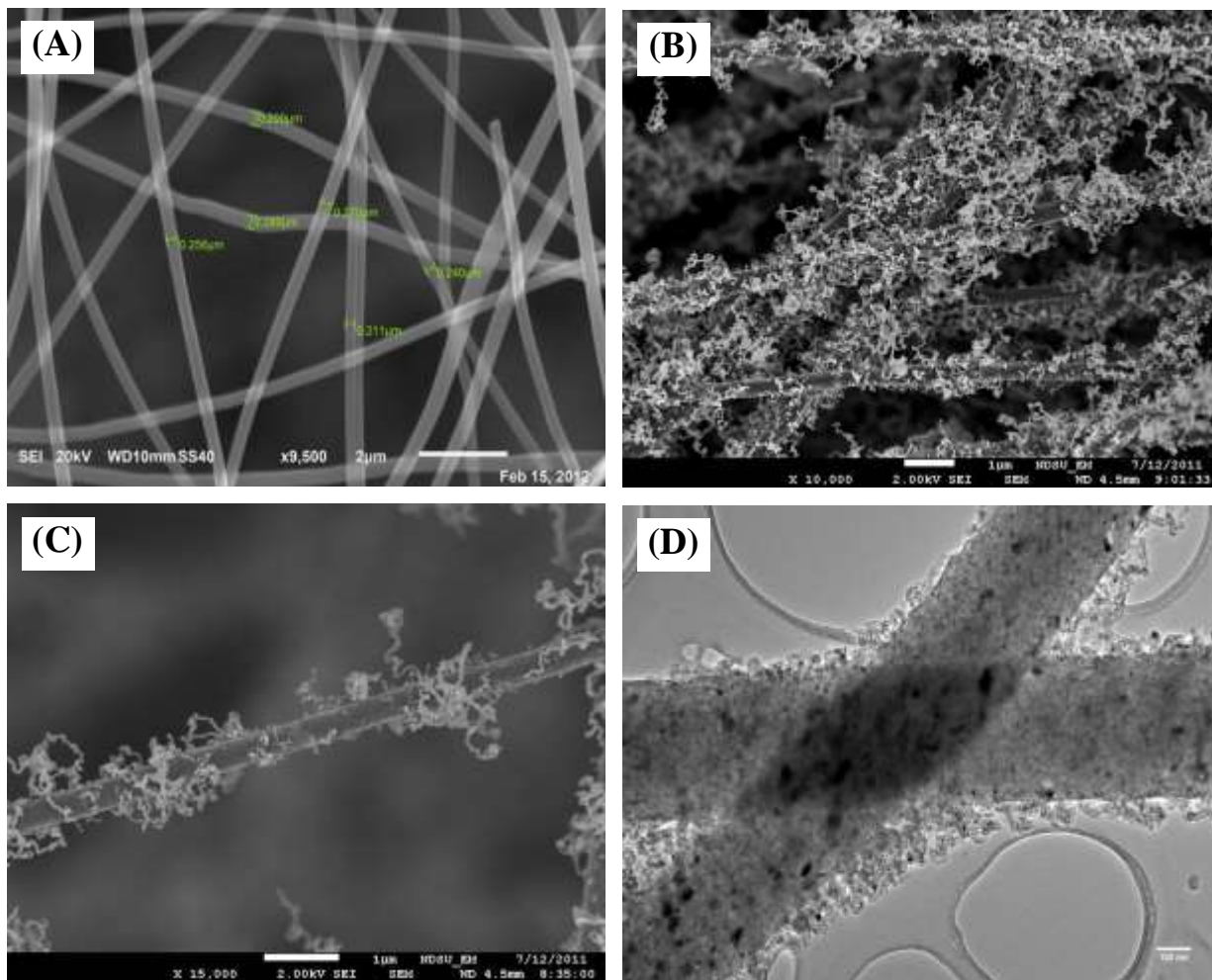
Figure 4.3. SEM micrographs of (A) purified CNFs, (B) CNT/CNFs, and (C) a typical CNT-grown CNF; TEM micrograph of (D) CNT/CNFs.

4.3.3. SEM and TEM micrographs of PANI/CNT/CNFs

It has been reported that the morphology and microstructure of PANI can be sensitively tailored by templates during *in situ* polymerization (Niu et al., 2012). In this process, CNF and CNT/CNF films were used as the 3D free-standing templates for growing ordered PANI

nanostructures. Due to the hydrogen bond effect of CNFs, some aniline molecules may be adsorbed on the surface of CNFs (Yan et al., 2010). Once APS was added, these adsorbed aniline molecules polymerized preferentially to form small PANI 'seeding dots'. These "seeding dots" further reacted to form PANI nanowires as shown in Fig. 4.4 (A) (Wei et al., 2013; Yan et al., 2011). These PANI nanowires carried needle-like morphology and vertically positioned on the surface of CNFs. The TEM micrograph of Fig. 4.4 (B) further reveals the formation of uniform needle-like PANI nanowires with a diameter in the range from 50 to 80 nm and a height up to 150 nm. In addition, the diameter and height of the PANI nanowires could be tuned via adjusting the concentration of aniline, temperature, and duration of polymerization (He et al., 2012; Wei et al., 2013; Yan et al., 2011).

Figure 4.4 (C) is the SEM micrograph of PANI-coated CNT/CNFs, which carried homogenous, ultrathin PANI layers on the surface. However, the needle-like PANI nanowires of PANI/CNFs were not observed in this SEM analysis. This is because the anilines were sufficiently adsorbed onto the surface of CNT/CNFs to form a thin PANI layer at the initial stage of polymerization, owing mainly to the rich hydroxyl and carbonyl groups existing on the surface of CNT whiskers as well as their high aspect ratio (Zhou et al., 2013; Peng et al., 2007). The PANI multilayers were further formed by reacting with the free aniline in solution. In addition, the TEM micrograph further validates the successful synthesis of the hierarchical porous PANI/CNT/CNF films (Fig. 4.4 D). The diameters of PANI/CNT nanowires were about 30-60 nm and the thickness of PANI layers coated on CNTs was about 10-30 nm, which were estimated from the above SEM micrographs. Compared to the nanostructured PANI prepared by polymerization of aniline with the aid of CNTs (Ghosh et al., 2013; Zhou et al., 2013; Peng et al., 2007; Hyder et al., 2011), the present PANI/CNT/CNF films provided a rougher surface with higher specific surface area, which

guaranteed the high-performance of the resulting supercapacitors. Meanwhile, the CNT/CNF networks functioned as the excellent current-delivery channels to suppress the electrical contact resistance of the electrodes due to their high electrical conductivity and excellent topological connectivity.
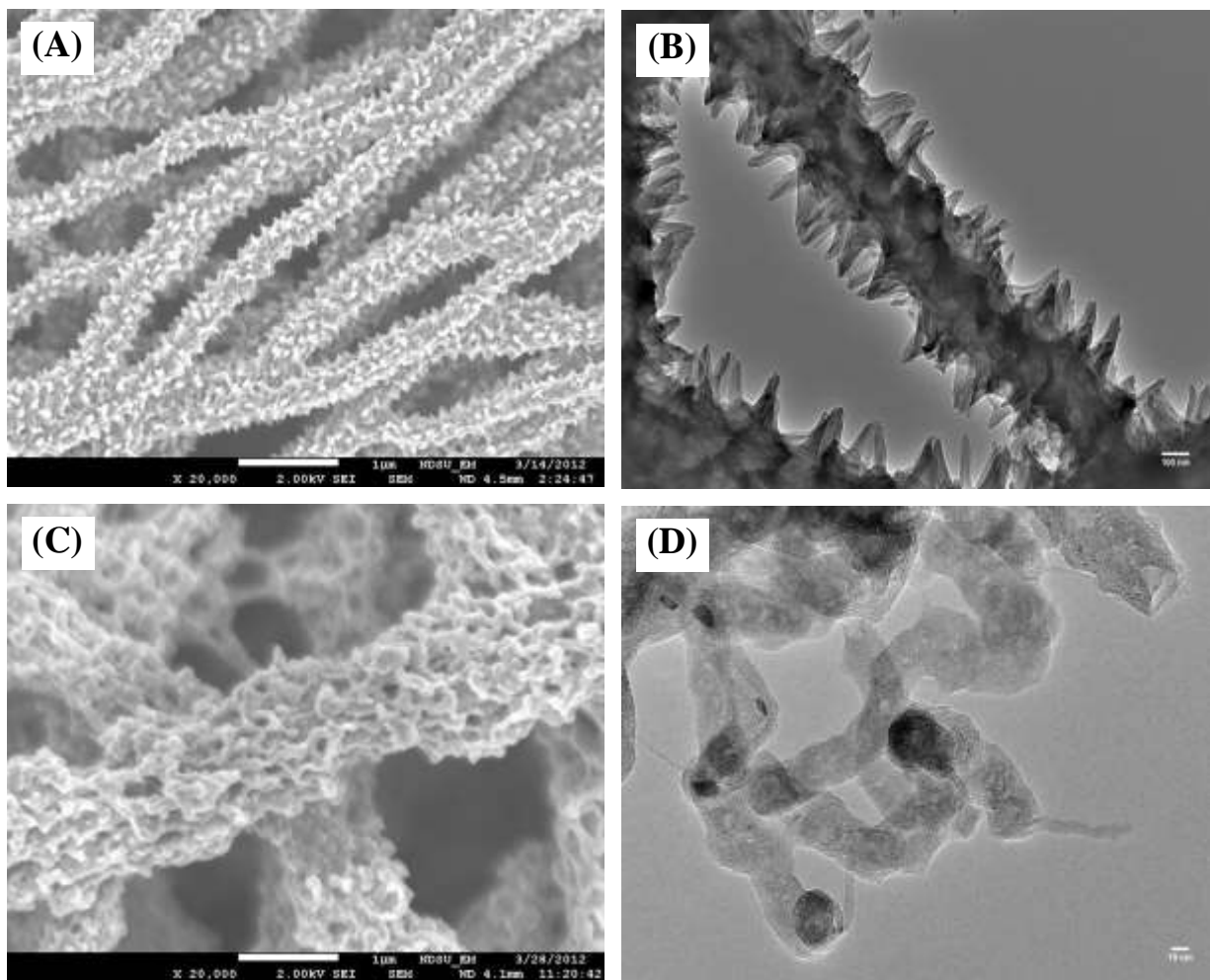
Figure 4.4. SEM micrographs of (A) PANI/CNFs and (C) PANI/CNT/CNFs; TEM micrographs of (B) PANI/CNFs and (D) PANI/CNT/CNFs.

4.3.4. Raman spectra of PANI/CNT/CNFs

The chemical microstructures of electrode materials were characterized by means of Raman spectroscopy, which can provide detailed information of their molecular structure and

further confirm the structure of PANI/CNT/CNFs. The Raman spectra of PANI/CNT/CNF and CNT/CNF films were carried out at an excitation wavelength of 632.8 nm as shown in Fig. 4.5. The curve of CNT/CNF film shows two typical characteristic peaks at 1,582 cm^{-1} (G bands) and 1,349 cm^{-1} (D bands), which were attributed to the phonon propagation along the graphitic structures and the disordered turbostratic structures or defects, respectively (Zhou and Wu, 2013). In the plot of the PANI/CNT/CNF films, the characteristic bands of PANI and some overlap bands with CNT/CNF films can be observed. The band located at 1,166 cm^{-1} was attributed to the C-H bending vibration of the benzenoid/quinoid ring; the peak located at 1,216 cm^{-1} was linked to the weak C-N stretching. The bands situated at 1,491 cm^{-1} and 1,582 cm^{-1} were corresponded to the C=N stretching of the quinoid ring and C-C stretching of the benzenoid ring of PANI, respectively (Li et al., 2012; Ghosh et al., 2013; Wei et al., 2013). Moreover, the peak of C-N*$^{+}$ at 1,333 cm^{-1} was resulted from the formation of a radical cation on the doping and co-doping of PANI (Ghosh et al., 2013). As shown, the PANI/CNT/CNF films yielded the similar Raman data as the PANI materials prepared by polymerization under acid condition, which is in a good agreement with those reported recently in the literature (Peng et al., 2007; Hyder et al., 2011; Zhou et al., 2013; Wei et al., 2013).
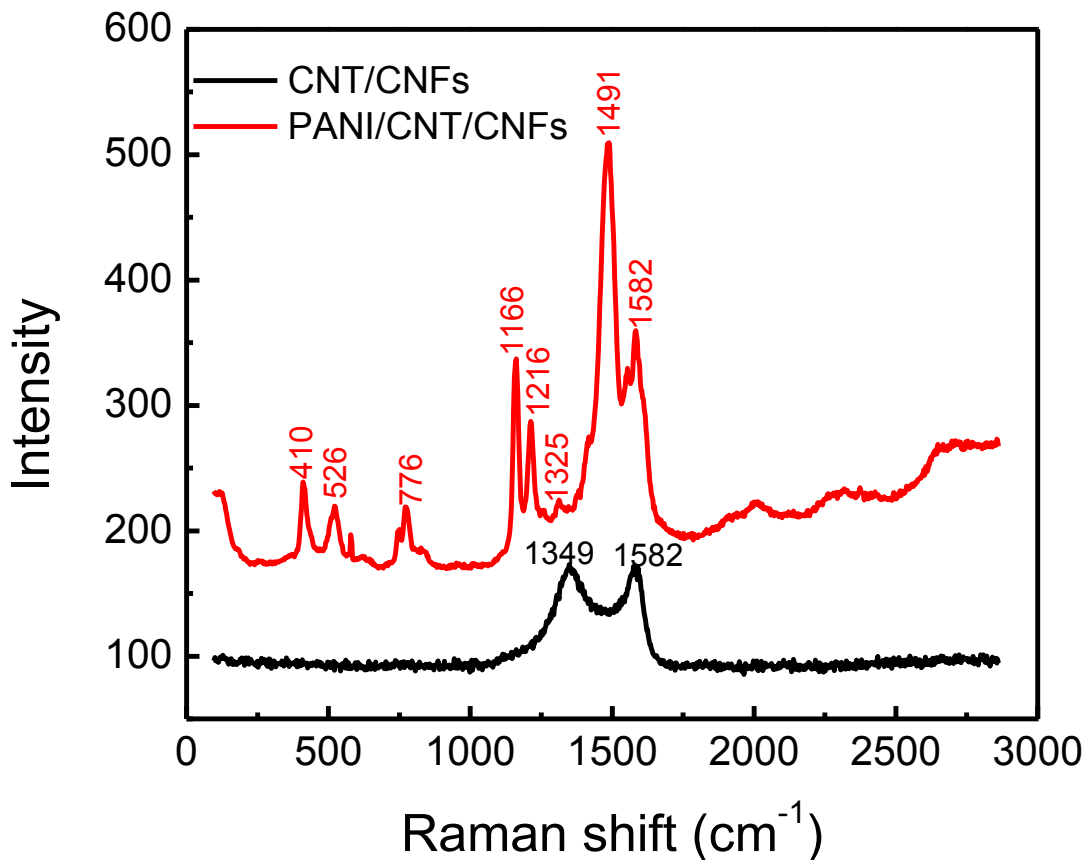
Figure 4.5. Raman spectra of CNT/CNF and PANI/CNT/CNF films.

4.3.5. FTIR spectra of PANI/CNT/CNFs

Figure 4.6 shows the typical Fourier transform infrared spectroscopy (FTIR) spectra of PANI/CNT/CNF and CNT/CNF films. The absorption peaks at 1,564 cm^{-1} and 1,465 cm^{-1} correspond to the C–C stretching deformation mode of the quinoid (Q) and benzenoid (N) rings of PANI, respectively (Tang et al., 2009). The peaks at 1,231 cm^{-1} and 1,294 cm^{-1} were attributed to the C-N stretching vibration of an aromatic conjugation. The N-Q-N stretching band at 1,087 cm^{-1} is the characteristic band of the PANI (Yuan et al., 2011). The intensities of these peaks imply

the formation of PANI layers onto the surface of CNT/CNFs. In contrast, a characteristic band of

CNT/CNFs associated with C-C symmetric stretching was observed at 790 cm^{-1}.
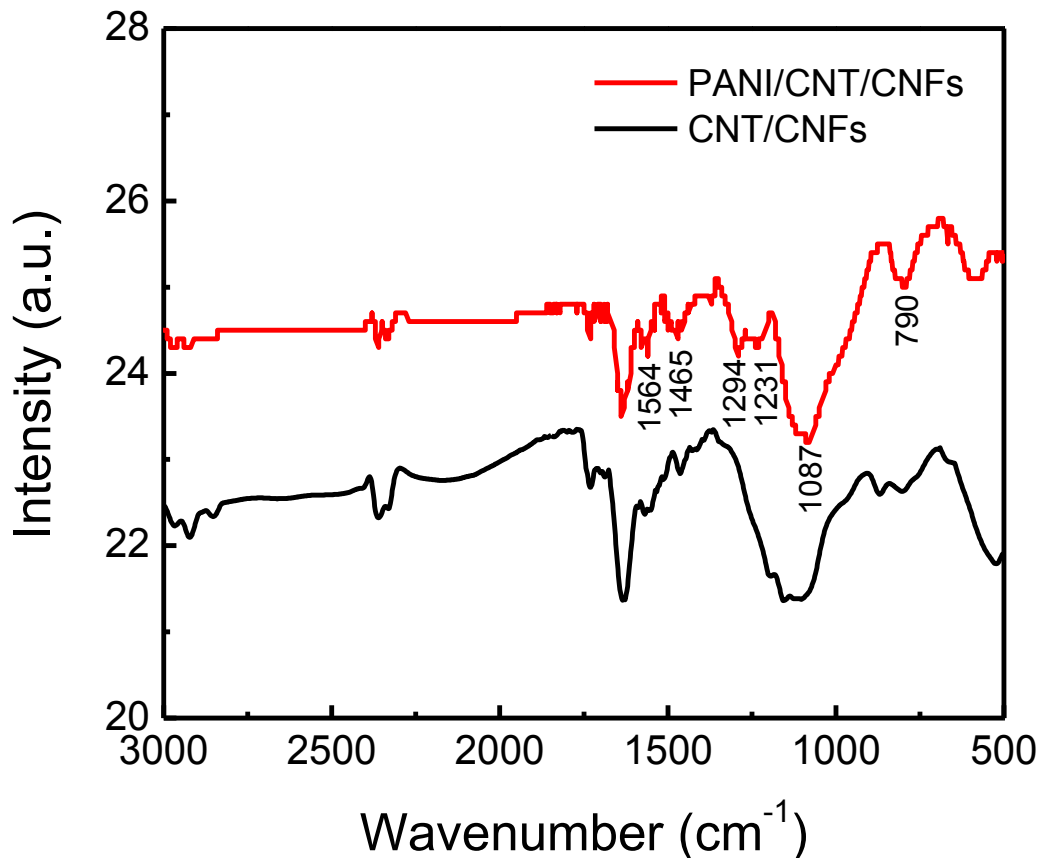
Figure 4.6. FTIR spectra of CNT/CNF and PANI/CNT/CNF films.

4.3.6. EIS characterizations

EIS has been considered as a very effective method for analyzing the electrochemical

impedance properties of a material, including the internal electrical resistance, charge transport in

electrode/electrolyte, and ion diffusion of electrochemical devices (Kötz and Carlen, 2000). In this

work, two patches of stainless steel mesh were used as the current collectors and a 1 M H_2SO_4

aqueous solution was utilized as the electrolyte. Figure 4.7 shows the Nyquist plots of PANI/CNF

and PANI/CNT/CNF film electrodes in the frequency ranging from 100 kHz to 0.01 Hz under an open circuit potential. As shown, both Nyquist plots consist of two distinct parts including a small semicircle at the high frequency region and an inclined line in the low frequency region. The x-intercept in the Nyquist plots represents the equivalent series resistance (ESR), which is corresponded to the electrical resistance of the electrolyte solution and the electrical contact resistance of the electrode/electrolyte (Ryu et al., 2002; Lai et al., 2012). As observed from the plots, the ESR values of PANI/CNF and PANI/CNT/CNF electrodes are about 1.50 and 1.46 Ω, respectively. Clearly, these electrodes had a small semicircle in the high frequency region, indicting a low interfacial charge-transfer resistance (R_{ct}). As calculated from the diameter of semicircles, the R_{ct} values are 0.50 and 0.55 Ω, respectively. Such a low R_{ct} indicates the very good interfacial conductivity between the PANI and carbon materials. Besides, the R_{ct} values of both PANI/CNF and PANI/CNT/CNF electrodes are much lower than the values reported for the CNF-PANI composite paper (9.2 Ω) (Yan, 2011), hybrid PANI-CNT/Ni electrode (10.0 Ω) (Li et al., 2012), and ordered mesoporous carbon/PANI composite (5.4 Ω) (Li et al., 2009). The inclined lines of the Nyquist plots were attributed to the ion diffusion in the electrode/electrolyte, known as the Warburg behavior (Wang et al., 2009). The PANI/CNT/CNF electrode with nearly vertical line exhibited higher accessibility of PANI surfaces for ion diffusion than that of PANI/CNF electrode. This is due mostly to the unique integrated nanostructure, in which the CNF network was utilized as current collector and the CNT-coated CNFs acted as charge channels of the PANI layers. All the EIS data further demonstrated the successful synthesis of PANI/CNT/CNF hybrids with enhanced ion diffusivity and conductivity.
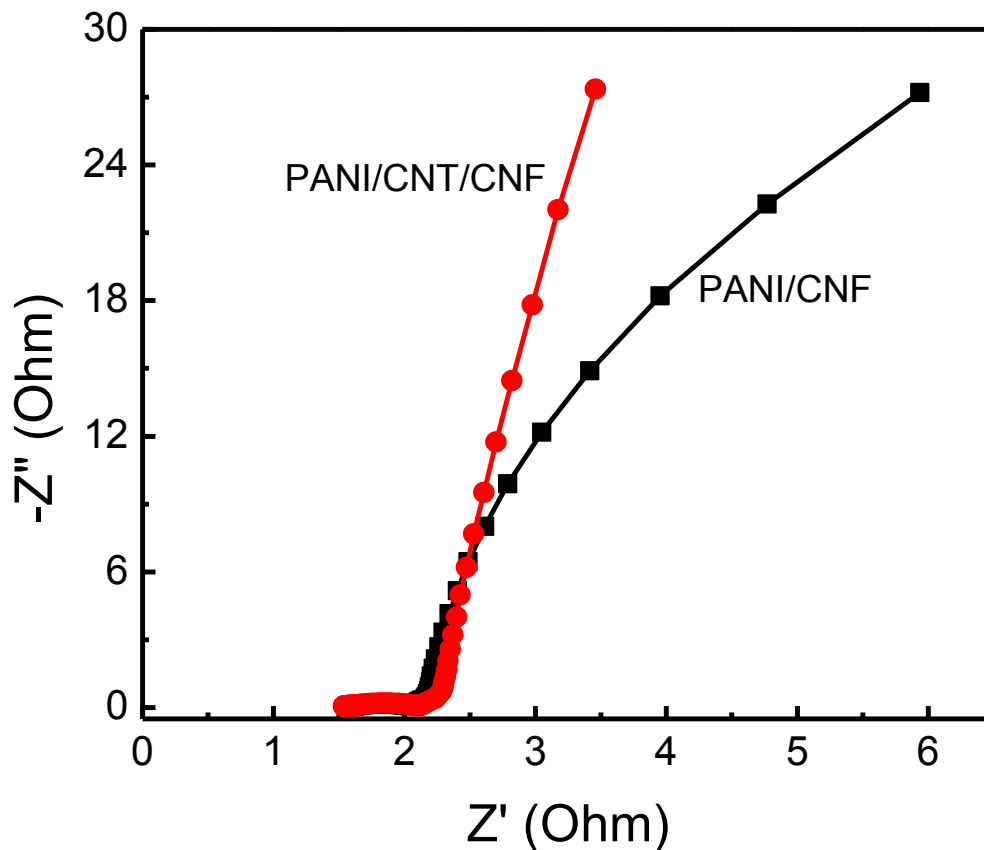
Figure 4.7. Nyquist plots of PANI/CNF and PANI/CNT/CNF film electrodes in 6 M KOH solution in the frequency range of 100 kHz - 0.01Hz. Z' and Z'' are the real and imaginary parts of the complex impedance, respectively.

4.3.7. CV characterizations

The electrochemical properties of the electrode materials were further characterized by CV and GCD in this study. Figure 4.8 shows the CV curves of the supercapacitors. The experiments were carried out at a potential scan rate of 5 mV/s in a wide potential range of -0.2 – 0.8 V. The background signal of the stainless steel mesh is negligible. Compared to the CNF electrode, the CV curve of CNT/CNF electrode exhibited a nearly rectangular shape along with the time-potential axis, indicating its excellent double-layer electrochemical performance. This observation

65

is due mostly to the unique structure of CNT/CNFs with enhanced specific surface area and conductivity. The PANI/CNF and PANI/CNT/CNF electrodes clearly demonstrated two pairs of typical redox peaks (C_1/D_1 and C_2/D_2), which are characteristic of PANI materials. The first pair of peaks C_1/D_1 can be ascribed to the redox transition from the leucoemeraldine form to the polaronic emeraldine form. The second pair of peaks C_2/D_2 is corresponded to the Faradaic transformation of emeraldine/pernigraniline (Wang et al., 2009; Wei et al., 2013; Zhou et al., 2013). Generally speaking, conducting polymer (e.g., PANI and PPy) stores and releases charges through redox transitions, which is associated with the π–conjugated polymer chains. During the oxidation process (also referred to as p-doping), electrolyte ions are transferred to the polymer surface. In contrast, during the reduction process (also known as un-doping), electrolyte ions are transported back into the solution. As expected, the current density of PANI/CNT/CNF electrode was much higher than that of the CNF, CNT/CNF, and PANI/CNF electrodes at the same scan rate of 5 mV/s, implying the superior electrochemical performance of PANI/CNT/CNF film. In addition, as the CV plot of the PANI/CNT/CNF electrode is distorted and carries an area larger than that of the PANI/CNF, it implies that the PANI/CNT/CNF electrode exhibits a strong synergistic effect between the PANI layers and CNT/CNF network.
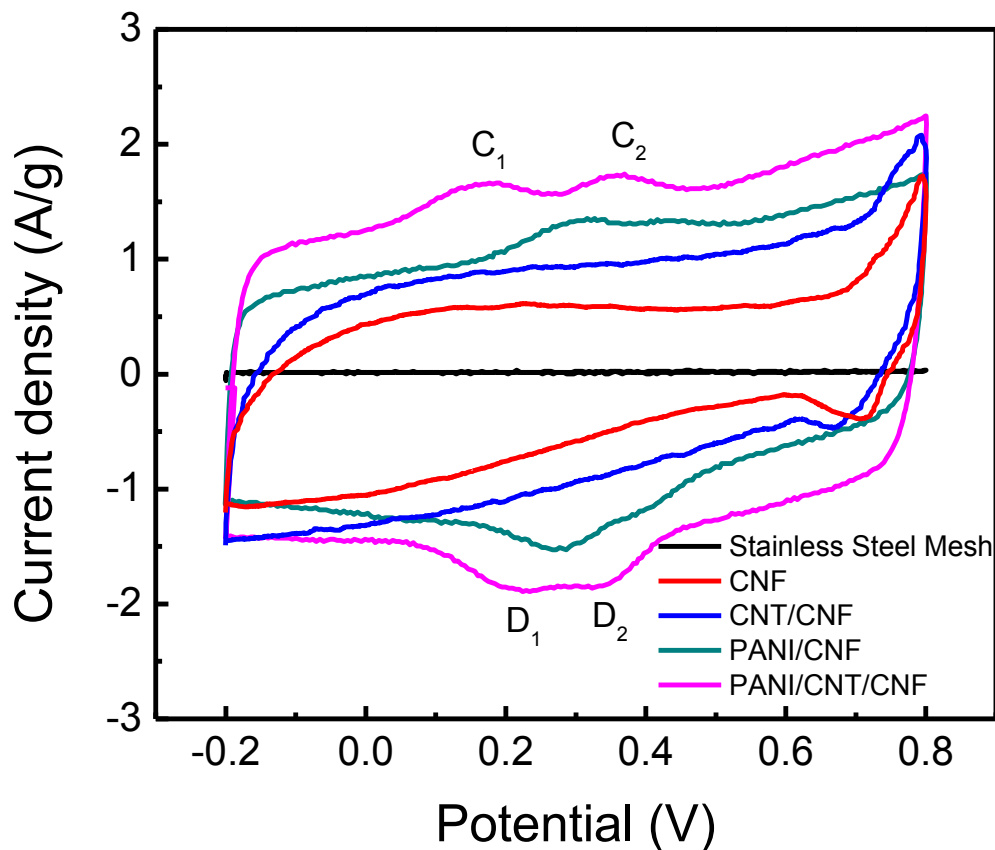
Figure 4.8. CV curves of the stainless steel mesh, CNF, CNT/CNF, PANI/CNF, and PANI/CNT/CNF film electrodes at a scan rate of 5 mV/s.

Figures 4.9 and 4.10 present the CV curves of PANI/CNF and PANI/CNT/CNF film electrodes at different scan rates from 5 to 100 mV/s, respectively. An obvious increase of the current density was observed for these electrodes with increasing scan rate. Meanwhile, it is notable that the cathodic peaks shifted positively, while the anodic peaks shifted negatively, which is attributed mainly to a slight increase of the electrode resistance at a high scan rate (Wang et al., 2006). The redox peaks even disappeared at a high scan rate of 100 mV/s, and the CV curves exhibit a symmetric and approximately rectangular shape, indicating the excellent charge transport

and low contact electrical resistance in the electrodes (Zhou et al., 2013; Cheng et al., 2013; Luo et al., 2013).
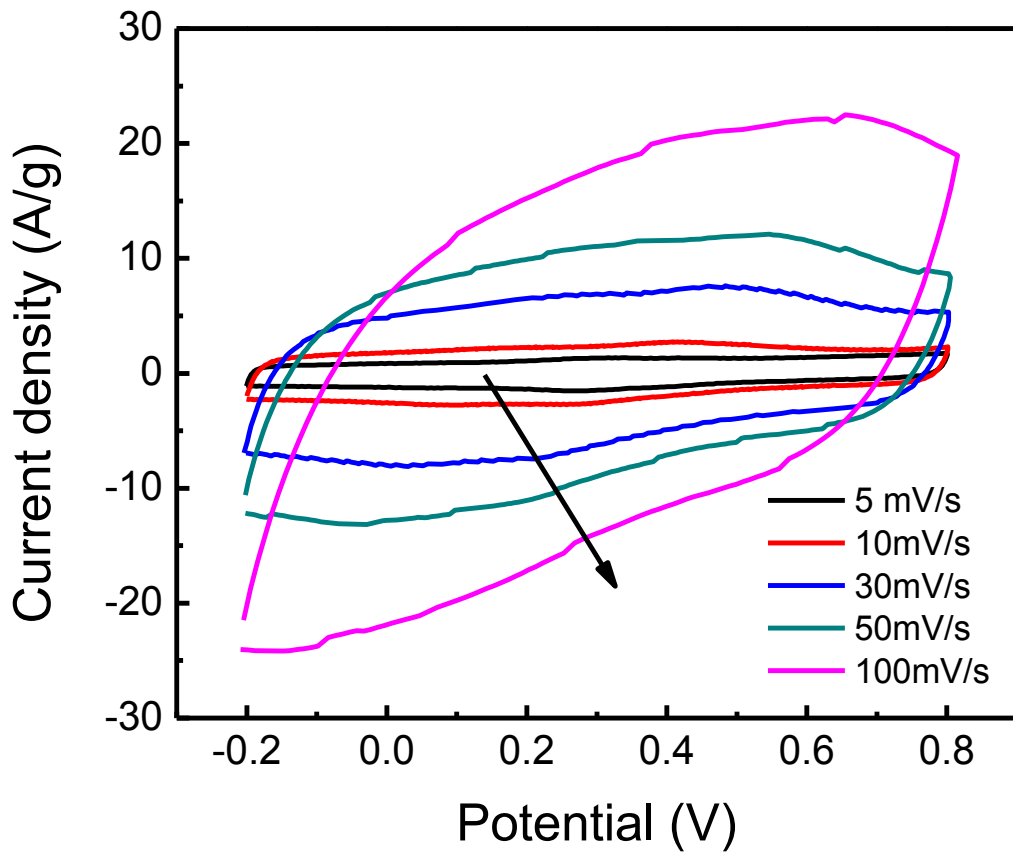
Figure 4.9. CV curves of the PANI/CNF film electrodes at different scan rate.
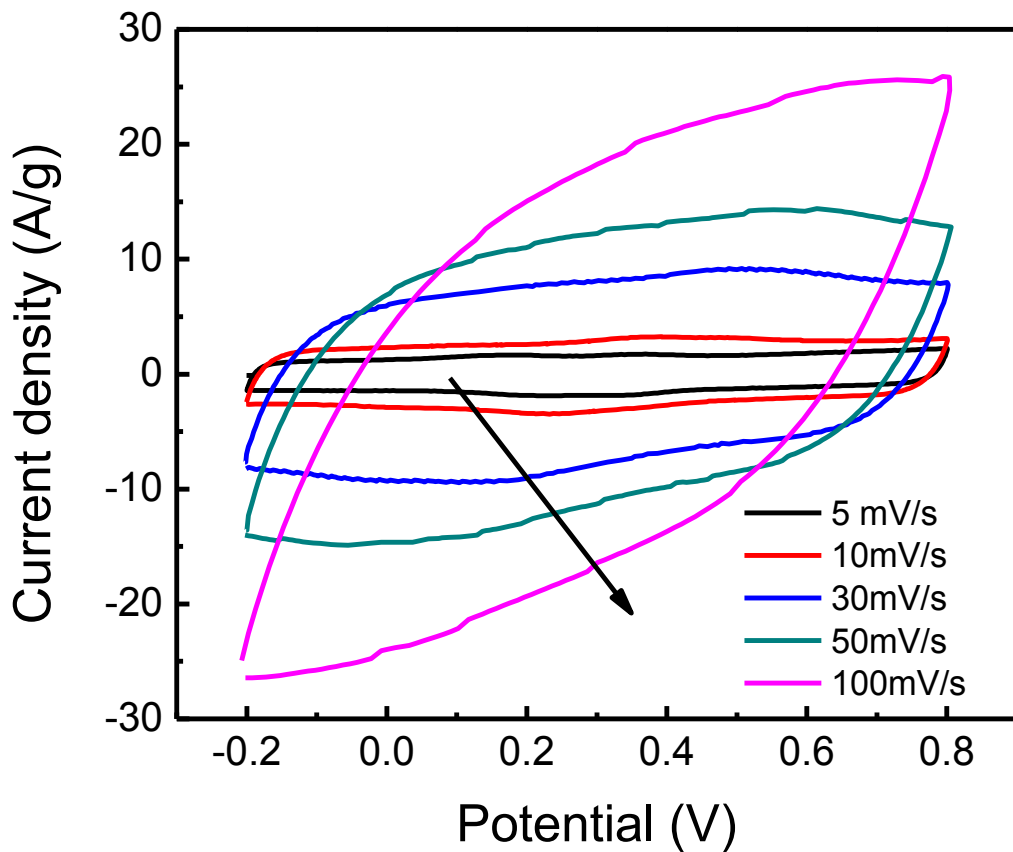
Figure 4.10. CV curves of the PANI/CNT/CNF film electrodes at different scan rate.

4.3.8. GCD characterizations

To further quantify the specific capacitance of the electrodes, GCD tests of the supercapacitor cells were performed in 1 M H_2SO_4 aqueous solution. Figure 4.11 shows the GCD curves of CNF, CNT/CNF, PANI/CNF, and PANI/CNT/CNF film electrodes at a current density of 0.3 A/g, respectively. In the case of CNF electrode, the GCD curve deviates from triangular shape during discharging, whereas in the case of CNT/CNF electrode, the GCD curve is a nearly triangular shape, indicating the reversible charge/discharge behavior of an ideal EDLC (Qu et al., 2012). The "IR drop" of the CNT/CNF electrode is lower than that of CNF electrode, which further

69

demonstrated that the internal resistance of the CNT/CNF electrode was largely suppressed by the grown CNTs. The GCD curves of PANI/CNF and PANI/CNT/CNF electrodes deviate from the linear shape owing to the existence of faradic pseudocapacitive effect of PANI (Biswas and Drzal, 2010; Li et al., 2011). As expected, due to its high capacitance, the PANI/CNT/CNF electrode exhibited a longer discharge time duration than that of the PANI/CNF electrode. This high capacitance further confirmed the favorable synergistic effect between the PANI layers and CNT/CNFs. It is worth to mention that the "IR" drops of the PANI/CNT/CNF and PANI/CNF electrodes are lower than those of the CNT/CNF and CNF electrodes, which is probably resulted from their low ion diffusion/transport resistance in the PANI surface.
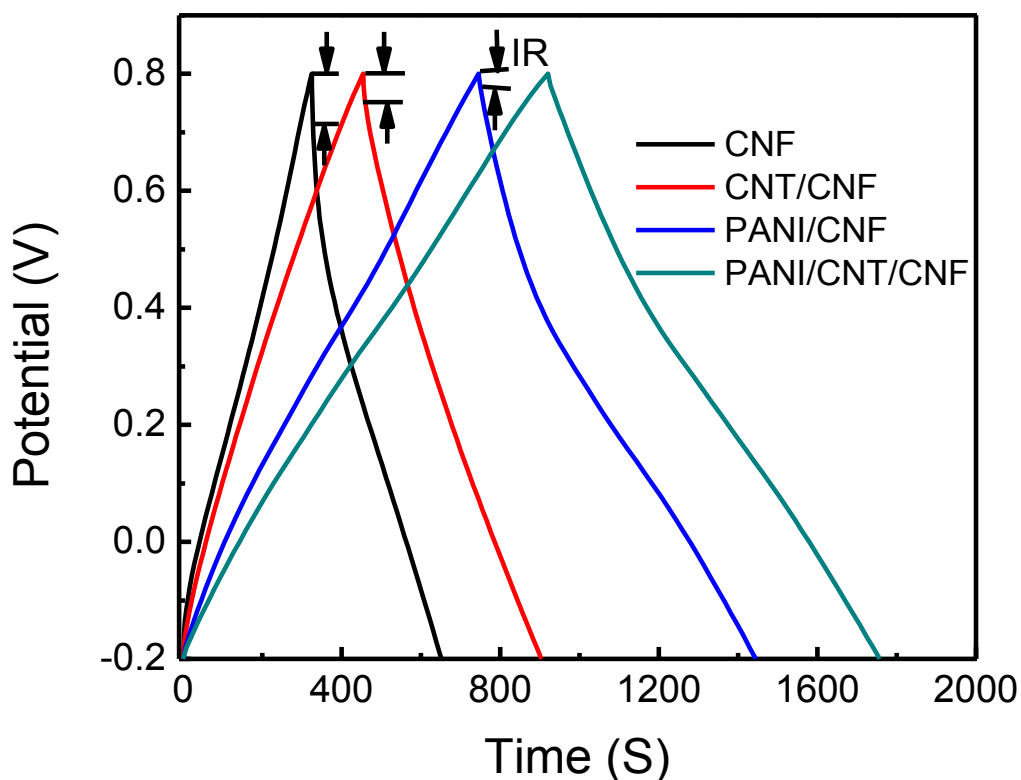
Figure 4.11. GCD curves of the CNF, CNT/CNF, PANI/CNF, and PANI/CNT/CNF film electrodes at a current density of 0.3 A/g, respectively.

The specific capacitance was calculated from the GCD curves according to the relation (2.4). At a current density of 0.3 A/g, the specific capacitance of PANI/CNT/CNF electrode is 503 F/g, much higher than that of PANI/CNF (422 F/g), CNT/CNF (270 F/g), and CNF (196 F/g) electrodes. As aforementioned, CNTs were wrapped by ultrathin PANI layers with the thickness of 10-30 nm, where the excellent electrical properties of CNTs such as high conductivity and specific surface area had been effectively activated. The CNT-coated CNFs played the important role as conductive channels of the PANI layers. As a result, it can be concluded that the improved capacitance is due mainly to the synergetic effect of the high specific surface area of PANI layers and the unique structure of CNT/CNFs. In this experimental study, the mass ratio of PANI is about 50 wt. % in the PANI/CNT/CNFs. With consideration of the synergistic effect between the PANI layers and CNT/CNFs, the real specific capacitance of PANI layers can be calculated as 736 F/g, i.e., {[(503 F/g (PANI/CNT/CNF) − 270 F/g (CNT/CNF)*50%] / 50%}. This capacitance is 2.26-4.36 times that of pure PANI nanofiber electrodes (169-326 F/g) (Zhou et al., 2004; He et al., 2012; Liu et al, 2013). It is also noticed that the capacitance of the novel PANI/CNT/CNF electrode in this study is competitive with those reported in the literature, for instance the PANI/SWCNT cloth composite (410 F/g at 0.5 A/g) (Niu et al., 2012), graphene/CNT-PANI composite (271 F/g at 0.3 A/g) (Cheng et al., 2013), PANI/MWCNT nanofiber (490 F/g at 0.5 A/g) (Zhou et al., 2013), PANI/MWCNT composite (560 F/g at 1 mV/s) (Zhou et al., 2010), CNT/PANI composite (424 F/g at 0.1 A/g) (Peng et al., 2007), PANI/CNT composite (528 F/g at 1.0 A/g) (Chen et al., 2013), core-shell MWCNT/graphene oxide nanoribbon (252.4 F/g at 50 mV/s) (Lin et al., 2013), and SWCNT/BiVO$_4$ composite (395 F/g at 2.5 A/g) (Khan et al., 2014).

The GCD curves of the PANI/CNT/CNF electrodes were examined at different current densities from 0.3 to 6.0 A/g as shown in Fig. 4.12. It can be observed that all the curves are nearly

linear and symmetrical in their shapes, indicating that the corresponding supercapacitor has an excellent electrochemical reversibility in a wide range of current density.
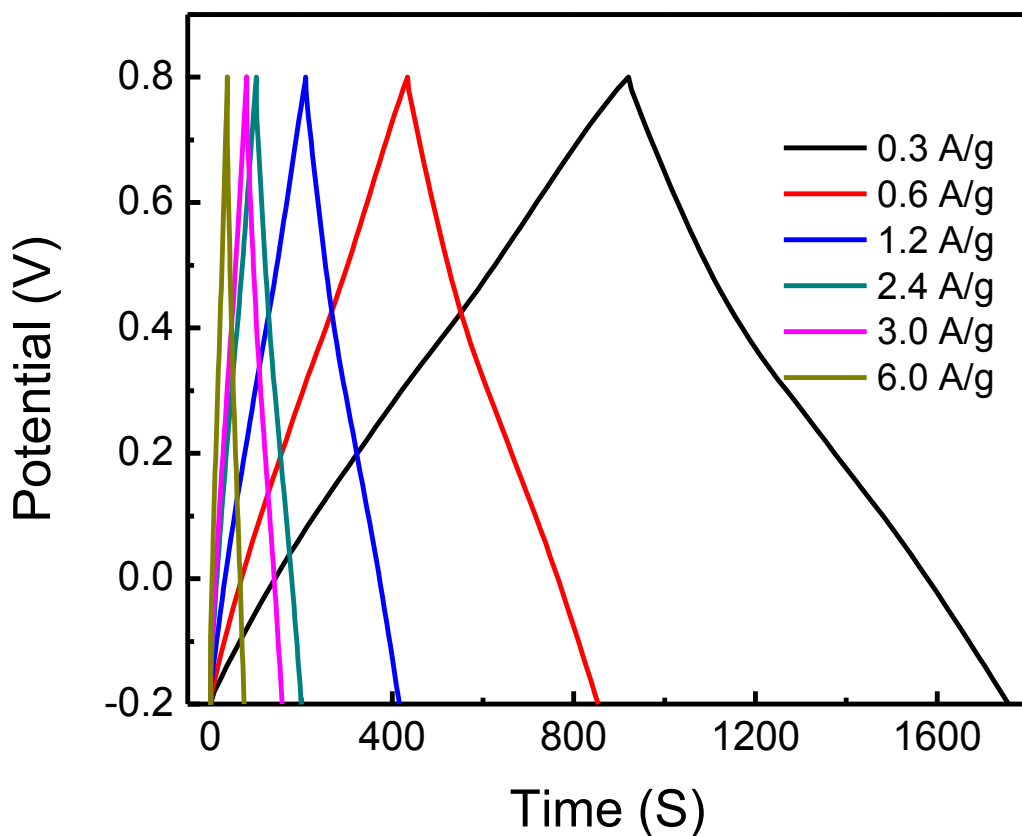
Figure 4.12. GCD curves of the PANI/CNT/CNF film electrodes at different current densities.

Figure 4.13 shows the influence of the specific capacitance of PANI/CNF and PANI/CNT/CNF electrodes upon the current densities. Interestingly, the capacitance values slightly increased at the low current densities and then decreased. For example, the capacitances of PANI/CNT/CNF electrode are 502, 503 and 504 F/g at the current densities of 0.15, 0.3 and 0.6 A/g, respectively, which demonstrated the superior rate capability. When the current density is increased to 3 A/g, the capacitance of PANI/CNT/CNF can still be maintained as high as 471 F/g, only 6% decrease compared to the capacitance at 0.3 A/g. On the contrary, up to 13% of

capacitance was dissipated for the PANI/CNF electrode. Besides, about 28% of the maximum capacitance of PANI/CNT/CNF electrode was decayed at a high current density of 15 A/g.
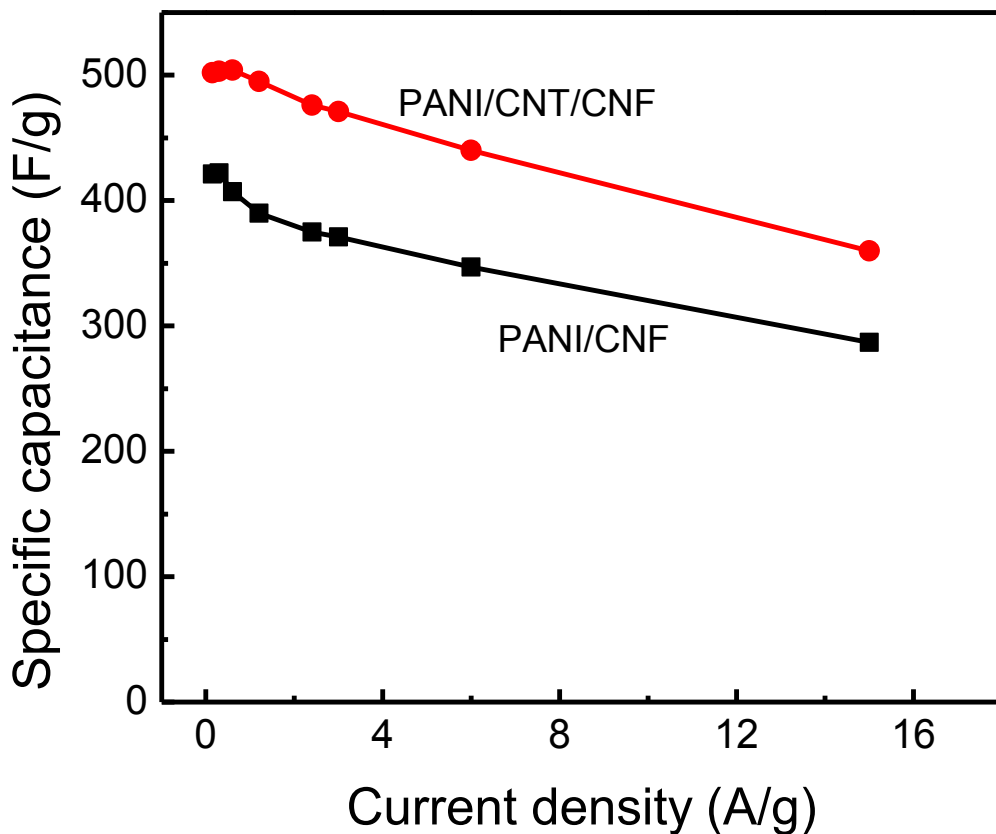
Figure 4.13. Variation of the specific capacitance *vs.* the current density for the PANI/CNF and PANI/CNT/CNF film electrodes.

4.3.9. Cycling capability and energy and power densities

To evaluate the cycling capability of the PANI/CNT/CNF supercapacitor, the GCD curves were obtained for 1,000 cycles at a high current density of 15 A/g as shown in the inset of Fig. 4.14. It is observed that the capacitance value only dropped ~8% from 360 to 332 F/g after 1,000 cycles, revealing the remarkable cycling stability of the PANI/CNT/CNFs for potential use as electrode material of high-performance electrochemical supercapacitors. Furthermore, the energy

and power densities of the new supercapacitors were calculated from the GCD curves gained at various current densities. Figure 4.14 shows the Ragone plot of PANI/CNF and PANI/CNT/CNF supercapacitors. It can be found in Fig. 4.14 that the PANI/CNT/CNF supercapacitor delivered a high energy density of ~50 Wh/kg at a high power density of ~15 kW/kg. This energy density is ~25% higher than that of the PANI/CNF supercapacitor. In addition, the highest energy density of ~70 Wh/kg at a power density of 600 W/kg was obtained from the PANI/CNT/CNF supercapacitor, which is almost one order higher than the values of commercially available supercapacitors that have the energy densities of 1-10 Wh/kg (Zhao et al., 2011). It should be pointed out that their characteristics were performed at a potential window of -0.2 to 0.8 V in 1 M H_2SO_4 aqueous electrolyte. As a result, it can be expected that the PANI/CNT/CNF material could be combined with suitable battery electrode materials to form battery-supercapacitor hybrids (BSHs) to realize high-performance energy storage devices. All the experimental results reported in this chapter have been published in *RSC Advances* in 2014 (Zhou et al., 2014).
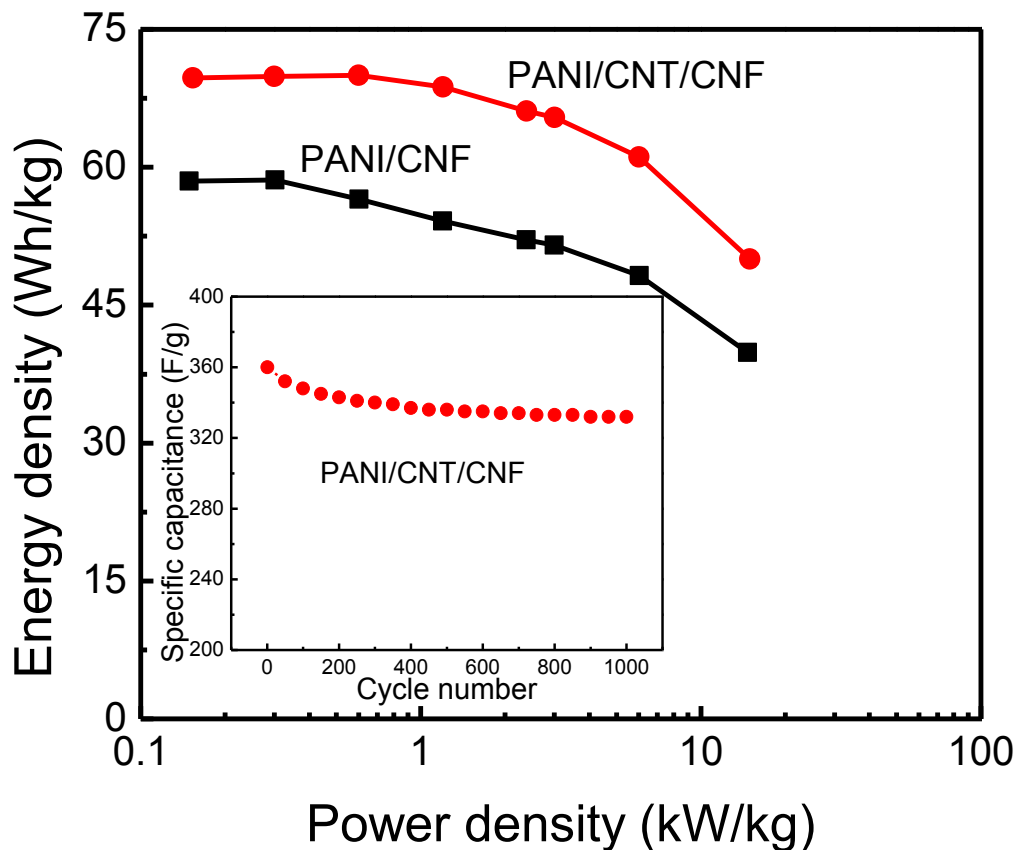
Figure 4.14. Ragone plot of the PANI/CNF and PANI/CNT/CNF supercapacitors, respectively; the inset of charging/discharging cycling stability of PANI/CNT/CNF film electrodes at a current density 15 A/g.

4.4.   Summary

Ordered, flexible PANI/CNT/CNF films have been successfully synthesized *via* three sequential steps: electrospinning, CNT growth, and *in situ* polymerization. Incorporation of the continuous CNT/CNF films has significantly enhanced the electrochemical properties of PANI/CNT/CNF film electrodes, such as the high interfacial charge-transfer conductivity and ion diffusivity. Such observation is due mostly to their unique integrated nanostructure, in which the CNF network was utilized as a current collector and the CNT-coated CNFs acted as charge

channels of the PANI layers. Supercapacitors based on PANI/CNT/CNF film electrodes exhibited a high specific capacitance of 503 F/g at a current density of 0.3 A/g and a superior cycling stability of ~92% specific capacitance retention after 1,000 cycles of charges and discharges. The highest energy density of ~70 Wh/kg and maximum power density of ~15 kW/kg have been achieved. Due to the effective synergistic effect between the PANI layers and CNT/CNF networks, such high-performance supercapacitors are expected for broader applications in electrochemical energy storage.

CHAPTER 5. FABRICATION AND CHARACTERIZATION OF GRAPHENE-BEADED CNFS FOR USE IN SUPERCAPACITORS

5.1.   Introduction

In this chapter, a new route was devised for synthesis and characterization of an innovative porous electrode material based on hierarchically continuous graphene-beaded CNFs (G/CNFs) for use in supercapacitors. The goal was to comprehensively exploit the advantages of electrospun CNFs (e.g., continuity and electrical conductivity) and graphene (e.g., large specific surface area and high electrical conductivity) for the purpose of electrical energy storage. The porous G/CNF films were produced via electrospinning PAN/DMF solution dispersed with oxidized graphene nanosheets and consecutive carbonization; the chemical structure and electrochemical properties of the novel G/CNF-based electrodes were characterized and compared with those based on pure electrospun CNFs (without graphene). The rest of the chapter is formulated as follows. Section 5.2 delineates the experimental details to produce and characterize the novel porous G/CNF electrode material. Section 5.3 describes the experimental measurements and relevant discussions. Consequently, Section 5.4 addresses the conclusions and prospect of the present study.

5.2.   Experimental

5.2.1. Materials

Commercial, as-grown, highly graphitic graphene nanosheets supplied by XG Sciences, Inc. (Michigan, USA) were employed in this study. The graphene nanosheets containing oxygen (<1 wt. %) had an average thickness of approximately 6 to 8 nm and a typical surface area of 120

to 150 m^2/g. PAN powder and solvent DMF were purchased from Sigma Aldrich, Inc. (MO, USA). All the materials were used as received without any further purification or change.

5.2.2. Preparation of continuous G/CNFs

To produce PAN/G nanofibers by means of electrospinning technique, the solutions for electrospinning containing graphene nanosheets and PAN in DMF were prepared using the following route. PAN powder was dissolved in DMF to prepare a 15 wt. % PAN/DMF solution. The dispersed graphene nanosheets in DMF were then added into the as-prepared PAN/DMF solution to achieve a graphene-dispersed PAN/DMF solution with the concentration of 10 wt. % PAN and 1 wt. % graphene nanosheets. Both the PAN/DMF and graphene-dispersed PAN/DMF solutions were prepared at a temperature of 80 $^{\circ}$C with continuous stirring for 24 h. The two as-prepared solutions were respectively placed into 10 ml plastic syringe installed with a spinneret, which was connected to a positive high-voltage DC power supply purchased from the Gamma High Voltage Research, Inc. (Ormond Beach, FL). A laboratory-made aluminum rotary plate with a diameter of 33 cm was connected to a grounded electrode as the nanofiber collector. The electrospinning process was performed in a high electric field of 80 kV/m, which was generated by applying a positive voltage 20 kV to a 25 cm gap between the spinneret and the collector plate. The flow rate of the electrospun solution was fixed at 1.0 ml/h using a digital flow controller. After electrospinning, randomly oriented PAN/G nanofiber films were obtained and peeled off from an aluminum foil which was attached onto the aluminum rotary plate. The gained PAN and PAN/G nanofibers were dried at 100 °C in oven for 6 h prior to the stabilization treatment.

The stabilization and carbonization of the as-prepared PAN/G nanofiber films were performed in a tubular furnace (Atomate, Inc., Santa Barbara, CA). The electrospun PAN/G

nanofiber nanosheets were first heated up at a rate of 1 °C/min and kept at 215°C for 1 h in air for the oxidative stabilization of PAN. The PAN/G nanofibers were then carbonized as the temperature was increased from 215 to 800 °C under Ar atmosphere at a rate of 5 °C/min and annealed at 800 °C for 30 min. Thereafter, the furnace was cooled down to 400 °C in Ar and then kept at this temperature by introducing air for 1 h to activate the carbonized PAN/G nanofibers. As a result, novel hierarchical graphene-beaded CNFs (G/CNFs) were obtained and used as the novel electrode material of supercapacitor.

5.2.3. Characterization of morphology and structure

The surface morphology of G/CNFs was analyzed by SEM. For the purpose of comparison, CNFs synthesized in Chapter 3 were also used as the control samples. In addition, TEM was used to characterize the microstructure of the G/CNF samples. Before measurements, the samples were dispersed in acetone and then deposited on a Cu grid. The structural variations of the G/CNF specimens were identified by a laser confocal Raman spectrometer (Nicolet NXR 9650 FT-Raman spectrometer, 632.8 nm).

5.2.4. Electrochemical measurements

Electrochemical characterization can be performed using a symmetrical two-electrode cell because it provides the most accurate evaluation of the electrochemical performance of the resulting electrode material for supercapacitors (Zhao et al., 2011). During fabrication of the supercapacitors, two pieces of 1.0 cm^2 G/CNFs were tailored into wire cloth, mesh, and perforated nickel-copper sheets, which functioned as the current collectors. A 6 M KOH aqueous solution was used for the electrolyte in this study. The two current collectors were used to conduct the

electrical current from each electrode. The electrochemical performance of the supercapacitor cells was evaluated by cyclic voltammetry (CV), galvanostatic charge/discharge (GCD). The CV and GCD curves were used to investigate the capacitive behavior and calculate the specific capacitance of G/CNF electrodes using Arbin Instruments' BT-2000 (TX, USA). The CV and GCD measurements of the G/CNF electrodes were recorded at the potential rage of 0 to 0.8 V by varying the scan rate from 5 to 100 mV/s.

5.3.   Results and Discussions

5.3.1. Morphology and structure characterization

5.3.1.1.   *SEM micrographs*

Digital optical image of the synthesized G/CNF film is shown in Fig. 5.1(A), from which it can be observed that the carbonized G/PAN nanofibers made from the precursor G/PAN nanofibers still keep the high structural flexibility and in-planar extensibility. With consideration of the unique topological connectivity and high electrical conductivity of the G/CNF network, the synthesized G/CNF films are suitable for potential use as interconnects and electrodes in stretchable electronic devices. Figures 5.1(B) and 1(C) are the typical SEM micrographs of the CNFs and G/CNFs, respectively. These electrospun CNFs with the diameter ranging from 300 to 400 nm were prepared via carbonization of the precursor as-electrospun PAN nanofiber at 800 °C, and these CNFs carried very smooth surface. In addition, Figure 5.1(D) is the high-resolution SEM micrograph of the G/CNFs, from which it can be clearly observed that the graphene nanosheets were closely jointed to the CNF segments after carbonization of the precursor as-electrospun G/PAN nanofibers. These platelet-shaped graphene nanosheets have an average in-planar size of 1–5 microns and an average thickness of 6–8 nm. In general, graphene nanosheets can attain a

large surface area and very high electrical conductivity, which may eliminate the need of conductive fillers and result in thinner electrodes.
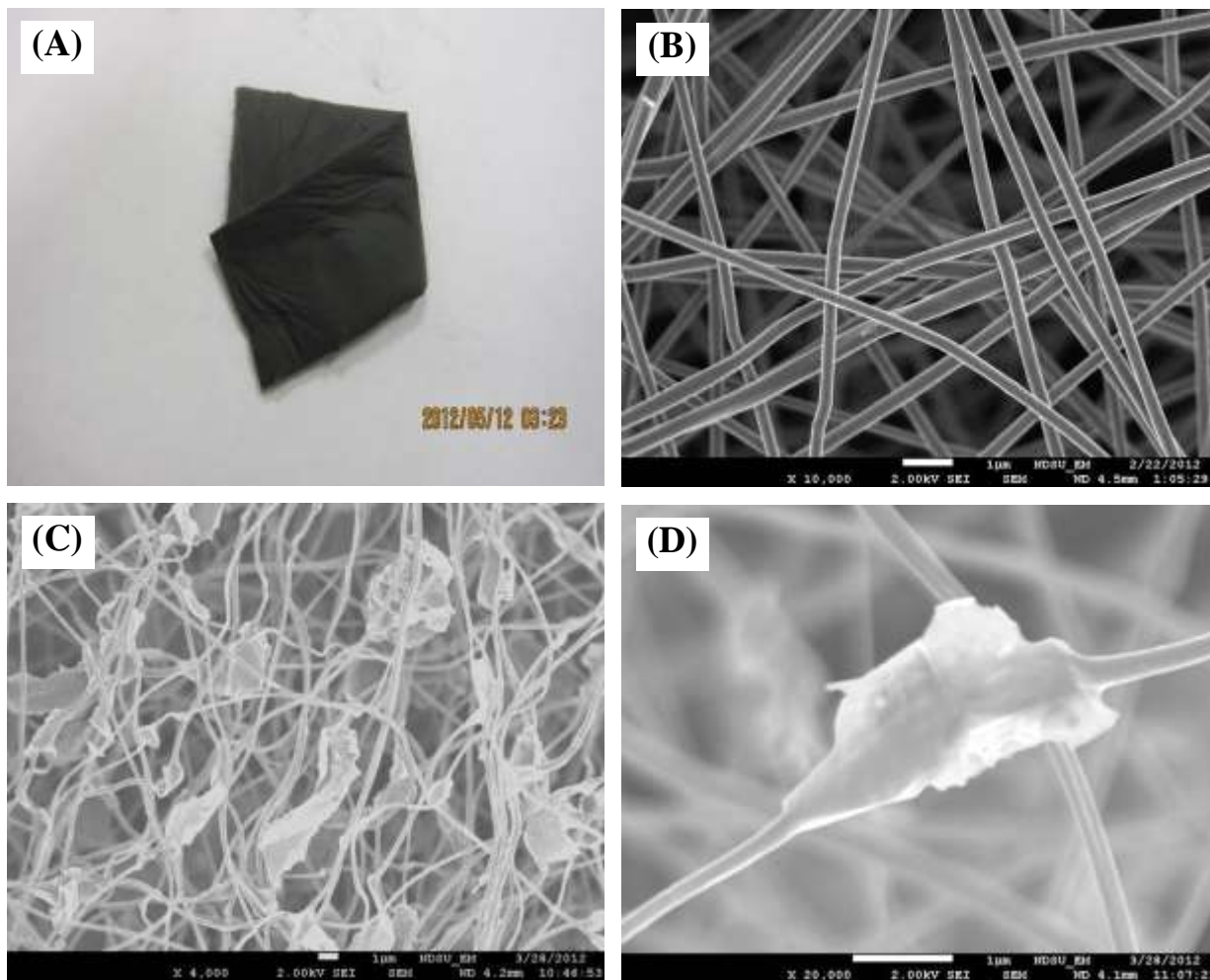
Figure 5.1. (A) Digital photograph of a piece of G/CNF film, (B) SEM micrograph of CNFs, and (C) low-magnification and (D) high-magnification SEM micrographs of G/CNFs.

5.3.1.2. TEM micrographs

Figures 5.2 (A) and (B) are the TEM micrographs of an as-electrospun G/PAN nanofiber segment and the corresponding graphene platelet, respectively. Figures 5.2 (C) and (D) are the TEM micrographs of the G/CNF nanofiber segments and the corresponding graphene platelet after carbonization, respectively. Obvious difference of the surface morphology between the G/PAN

nanofibers and G/CNFs can be identified such that the graphene nanosheets after carbonization exhibited sharper and cleaner edges because the graphene platelets in the as-electrospun G/PAN nanofibers might be covered dusts or solution residues after drying, which were burnt off during the process of carbonization. In addition, as shown in Figs. 5.2 (A) and (C), the graphene nanosheets are firmly connected at two ends with the nanofiber segments before and after carbonization. It is known that the graphene nanosheets were electrospun to form the G/PAN nanofibers, which consequently formed into the G/CNFs after carbonization. It needs to be emphasized that the connection between the graphene nanosheets and the CNF segments could be the strong covalent C–C bonds. Besides, Figure 5.2 (D) shows a typical linkage between a graphene nanosheet and its substrate amorphous CNF. At the edge of the graphene nanosheet, the graphene plane was detected onto the surface of the nanofiber segment (Balaya, 2008). Such a unique morphology would contribute to stabilization of the three-dimensional (3D) structure of the electrodes during the charge/discharge cycling and enhancement of the specific capacitance and cycling life span.
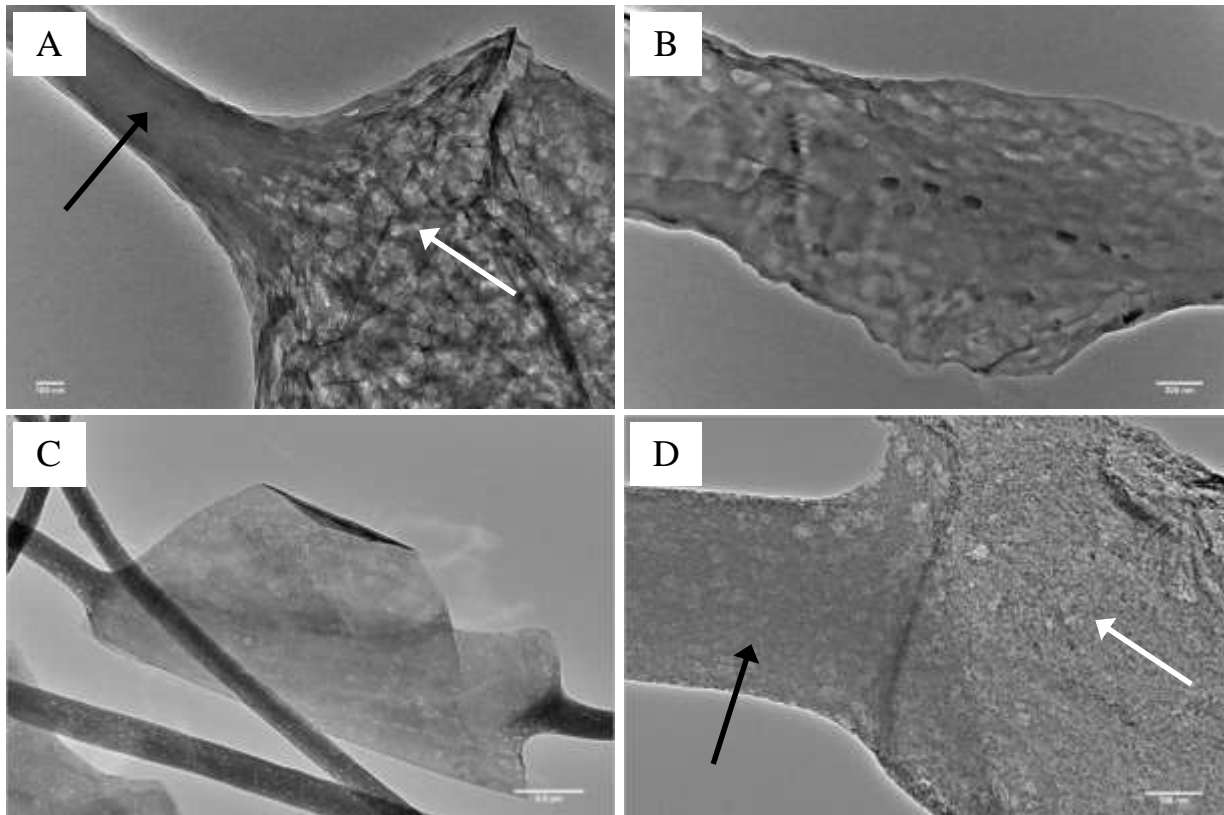
Figure 5.2. (A) & (B): TEM micrographs of an electrospun G/PAN nanofiber segment and a graphene nanosheet in G/PAN nanofiber segment before carbonization, respectively; (C) & (D): G/CNF segments at low and high magnifications after carbonization, respectively. The black arrows in micrographs (A) and (D) indicate a precursor PAN nanofiber and a carbon nanofiber, respectively; the white arrow marks the graphene nanosheet.

5.3.1.3.   *Raman spectra*

In this study, the chemical microstructure of the as-prepared CNFs was characterized by means of Raman spectroscopy. Figure 5.3 shows the comparative Raman spectra of CNFs (black, solid) and G/CNFs (red, dotted) in the region of 800–2,200 cm^{-1}. The Raman spectra of both the G/CNFs and pure CNFs exhibit two well-known bands of carbon at ~1,342 cm^{-1} and ~1,567 cm^{-1}, i.e., the "D-band" and "G-band", respectively. The D-band is attributed to the disordered turbostratic structures or defects in the curved graphene nanosheets (Geim, 2009); the G-band is related to the phonons propagating along the graphitic structures (Katsnelson, 2007). The intensity ratio of the

D peak to the G peak, denoted by $R=I_D/I_G$, represents the amount of ordered graphite crystallites in the CNFs. The *R* value of G/CNFs is 0.81, much lower than that of CNFs of 1.04. This difference indicates that the G/CNF films have more ordered graphite crystallites than the pure CNF films due to addition of the highly ordered graphitic (graphene) nanosheets (~20 wt.% in the final G/CNFs). Furthermore, addition of graphene nanosheets into PAN could potentially enhance the transition ratio of disordered carbon into ordered graphite carbon in CNFs during the process of carbonization. The above results on the chemical microstructure clearly demonstrate that the G/CNF films have higher electrical conductivity than the pure CNF films as shown in Fig. 5.4.
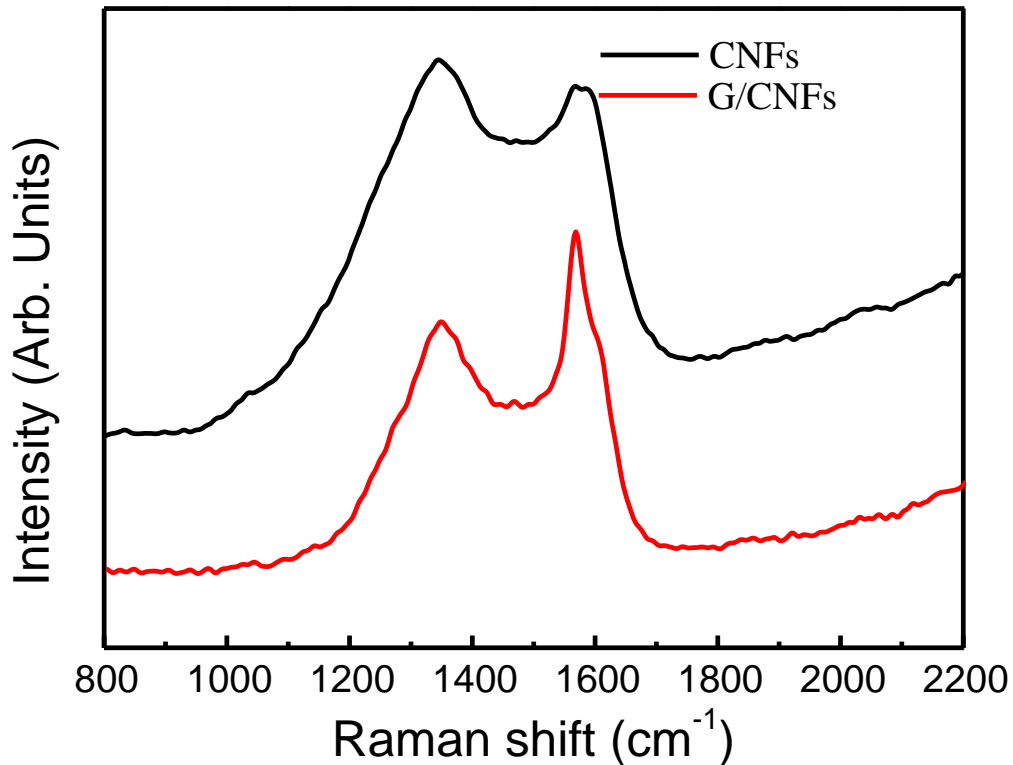
Figure 5.3. Raman spectra of CNFs (black) and G/CNFs (red), respectively.

5.3.2. Electrochemical characteristics

5.3.2.1.　　　*EIS characterizations*

The electrochemical impedance properties of the electrode materials based on CNFs and G/CNFs were investigated by EIS using a three-electrode cell. EIS is a very effective method to analyze the internal resistance, charge transfer in the electrode materials/electrolyte, and ion diffusion process of electrochemical devices (Kötz and Carlen, 2000; Ryu et al., 2002; Lai et al., 2012). Figure 5.4 shows the typical Nyquist plots of CNFs and G/CNF electrodes in the frequency range from 100 kHz to 0.01 Hz under open circuit potential. Both of the plots include two main parts: 1) a small incomplete semicircle at the high frequency region represents the charge transfer resistance of the electrode; 2) a nearly vertical line in the low frequency region corresponds to the diffusion behavior of ions in the electrode pores and the electrolyte (Ryu et al., 2002; Lai et al., 2012; Kim et al., 2007). As calculated from the intercept in the Fig. 5.4 insert, the internal electrical resistances of the CNF and G/CNF electrodes are 1.1 Ω and 0.8 Ω, respectively. These results imply that the graphene nanosheets suppressed the electrode resistance, corresponding to a smaller IR drop as observed in Fig. 5.7. The G/CNF electrode shows a nearly vertical line, which implies an ideal capacitive behavior with faster diffusion of ions in electrolyte than that of CNF electrode. Moreover, the improved electrolyte ion accessibility is associated with the lower resistance.
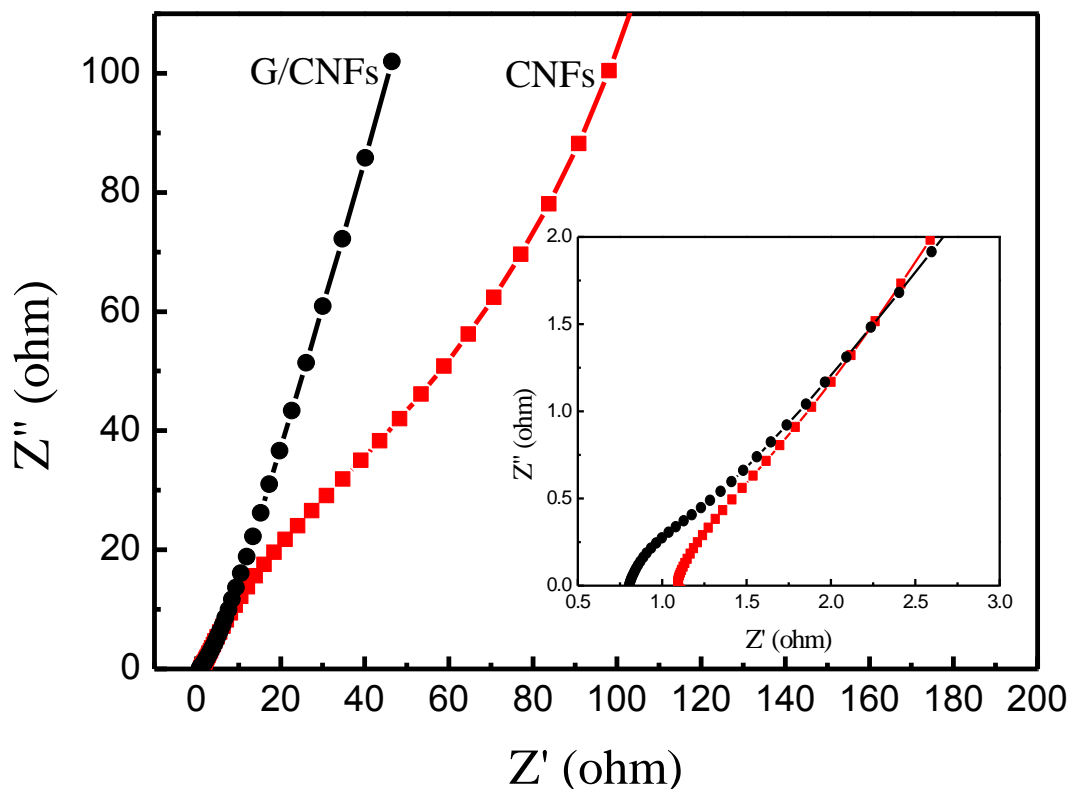
Figure 5.4. Nyquist plots for the CNF and G/CNF cells in 6 M KOH solution in the frequency range of 100 kHz - 0.01 Hz. $Z^{/}$ and $Z^{//}$ are the real and imaginary parts of the complex impedance, respectively.

5.3.2.2.   *CV characterizations*

To evaluate the electrochemical performance of the pure CNFs and G/CNFs, CV measurements were tested on the CNFs and G/CNFs as the electrodes of supercapacitors in a 6 M KOH aqueous solution, respectively. Figure 5.5 shows the typical CV curves of the tested CNF and G/CNF electrodes at a scan rate of 5 mV/s and a potential window of 0 $-$0.8 V. The CV curve of the G/CNF electrodes exhibits a nearly rectangle-shaped profile without obvious redox peaks, which is the characteristic of an ideal electrochemical double-layer capacitor. In contrast, the CV

curve of the control CNF electrodes becomes relatively distorted rectangular shape. This difference can be partially attributed to the improved internal electrical conductivity of G/CNF electrodes via graphene nanosheets interlaying. Figure 5.6 shows the CV curves of the G/CNF electrodes tested at different potential scan rates of 5, 10, 30, 50, and 100 mV/s and at the same electrolyte and potential window. With increasing potential scan rate, the CV profiles still retain a relatively rectangular shape without obvious distortion, even at the scan rate up to 100 mV/s.
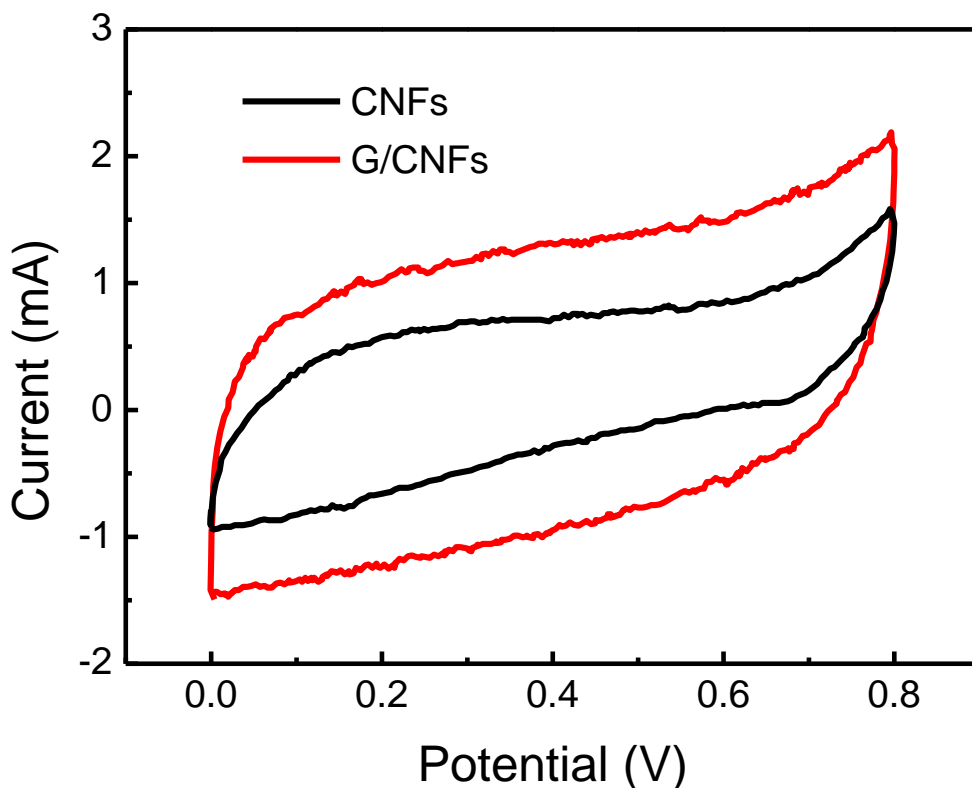
Figure 5.5. CV cureves of CNFs (black) and G/CNFs (red) samples at a scan rate of 5 mV/s in 6 M KOH.
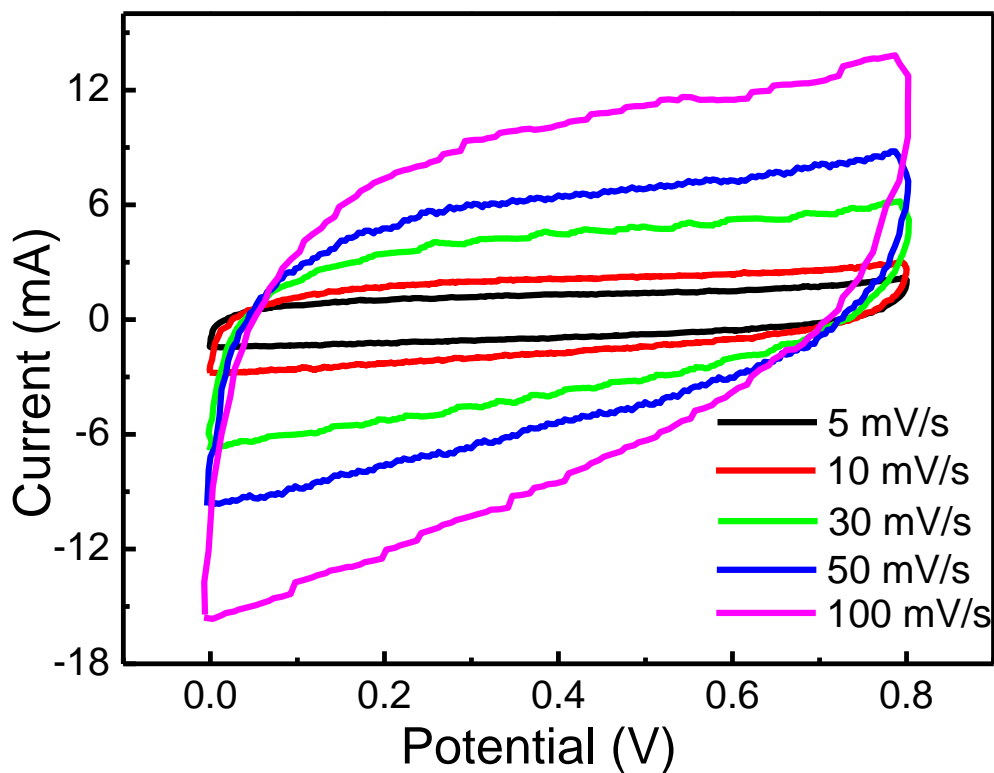
Figure 5.6. CV curves of the G/CNFs samples at different scan rate from 5 to 100 mV/s.

5.3.2.3. *GCD characterizations*

To accurately determine the electrochemical performance of the novel supercapacitors, the GCD performance of both the CNFs and G/CNFs as electrodes was characterized at several constant current densities. The average specific capacitance (C_s) of the electrodes in the prototype supercapacitor is calculated according to the relation (2.4). Figure 5.7 shows the representative charge/discharge curves of both the pure CNF and G/CNF electrodes at a constant current density of 500 mA/g. From these curves, the specific capacitance of the G/CNF electrodes is calculated as 226.2 F/g, twice that of the pure CNF electrodes (114.6 F/g). It can be observed that a voltage drop

existed at the beginning of the discharge curve, i.e., the IR drop due to the internal resistance of electrodes. Obviously, large internal resistance and contact resistance between the CNFs existed, as evidenced by a noticeable IR drop in the discharge curve in the CNF electrode as shown in Fig. 5.7. However, the IR drop is significantly lower than that of the CNF electrode. These results indicate that the unique interlaying graphene nanosheets effectively suppressed the internal electrical resistance of the electrodes.
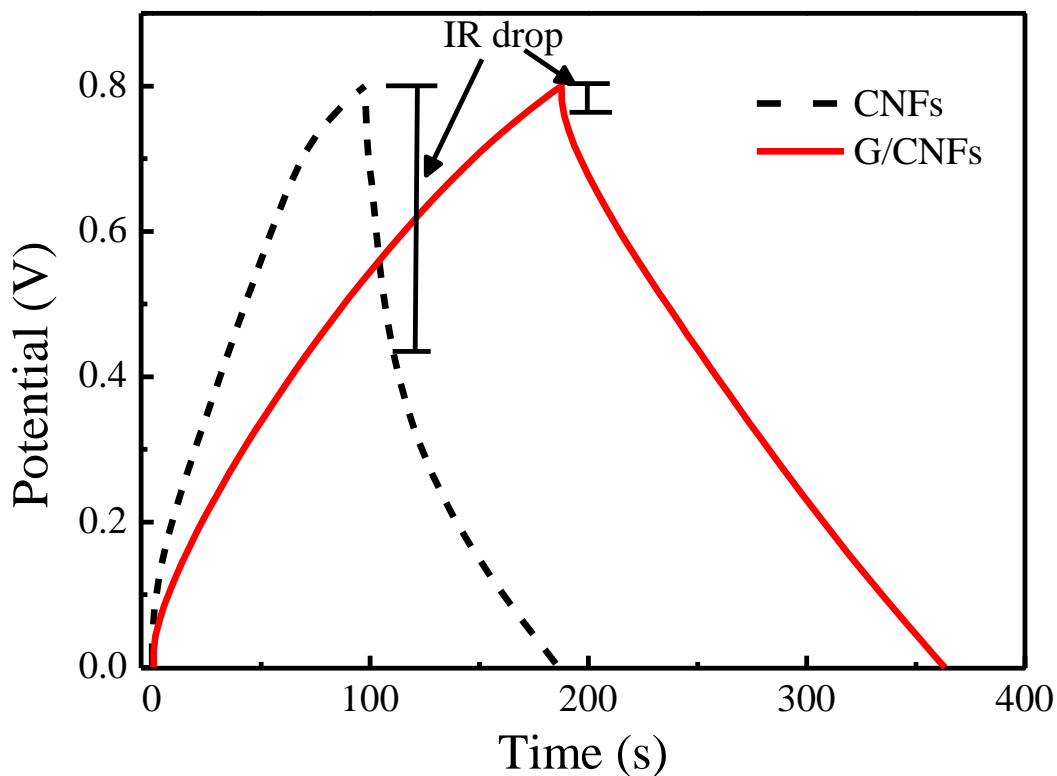
Figure 5.7. Charge-discharge curves of CNFs (black) and G/CNFs (red) at a constant current density of 500 mA/g.

Figure 5.8 shows the variation of the specific capacitance of the G/CNF electrodes with respect to the discharge current density from 100 mA/g to 5 A/g . In general, the specific

capacitance decreases slightly with increasing discharge current density. The maximum value of the specific capacitance of G/CNF electrodes reached 263.7 F/g at a discharge current density of 100 mA/g. It is noteworthy that the specific capacitance of the G/CNF electrodes still remained a high value of 131.25 F/g even at a high discharge current density up to 2.5 A/g. Also, the measured highest specific capacitance of G/CNF electrodes (263.7 F/g) is higher than the estimated specific capacitance (~175 F/g) based on the mass ratio (~50%) of graphene in G/CNFs and the specific capacitances of CNFs (~150 F/g) and graphene nanosheets (~200 F/g) as reported in the literature. It needs to be mentioned that the specific capacitance of graphene nanosheets reported in the literature was measured using randomly stacked graphene electrodes, in which the graphene nanosheets could be commonly stacked each other and thus charges could not be fully stored on all the surfaces of the individual nanosheets. Thus, the specific capacitance of stacked graphene nanosheets would be much smaller than that of nearly free-standing individual graphene nanosheets, like the ones in G/CNFs.
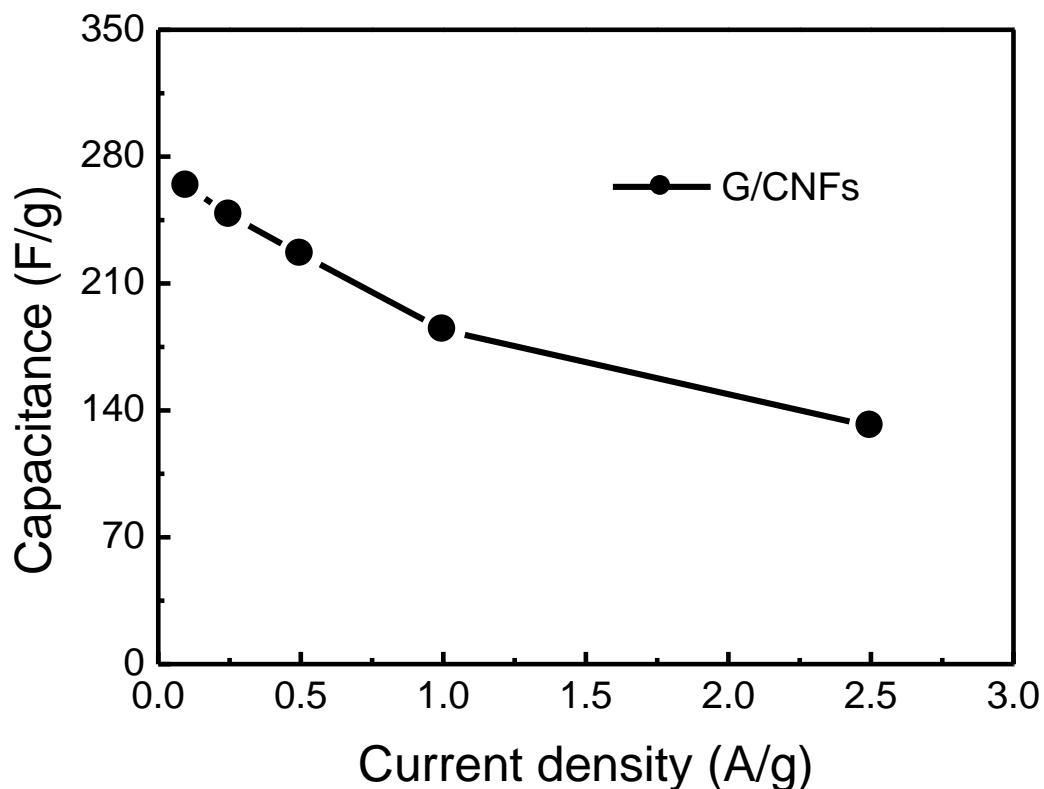
Figure 5.8. Variation of the specific capacitance of G/CNFs with the varying current density.

Furthermore, electrochemical stability is one of the crucial factors of supercapacitors for consideration of any practical use (Novoselov, 2011). The cycling life test of the CNF and G/CNF based supercapacitors had been performed in a 6 M KOH aqueous solution over 2,000 cycles. Constant current cycling was performed at a current rate of 2.5 A/g between 0 and 0.8 V. Figure 5.9 shows the specific capacitance retention ratio of the CNF and G/CNF electrodes as a function of the cycle number. The supercapacitor retention ratios of CNF and G/CNF electrodes were 75.6% and 86.9% after 2,000 cycles, respectively. This implies that incorporation of graphene nanosheets into the carbonized PAN nanofibers had a significant influence on the cyclic durability of the supercapacitor during the cycling charge/discharge process. Within the G/CNFs, graphene

91

nanosheets acted as interconnectors for improving the internal electrical conductivity and enhancing the specific surface area of the electrodes for charge storage. Meanwhile, the substrate CNFs also acted as frameworks to bridge the graphene nanosheets and prevent the nanosheets from severe swelling and shrinking during the cycling process (Stoller et al., 2008). Also, the retention ratio (86.9%) of the G/CNF electrodes after 2,000 cycles is lower than that of activated carbon (~95%) after the similar cycles though the G/CNF electrodes still carry the specific capacitance than that of activated carbon. The possible reconfiguration of the nearly free-standing graphene nanosheets in the G/CNF electrode at a high current density (2.5 A/g) could be responsible the fast decrease of the retention ratio of the G/CNF electrodes with the cycle number in the present study. Thus, further investigation is still desired for exploring the potential mechanisms of such a fast retention decrease and finding new routes to optimize the material design and selection for enhanced capacitive performance of the novel G/CNF electrodes in this study. All the experimental results reported in this chapter have been published in *Journal of Power Sources* in 2013 (Zhou and Wu, 2013).
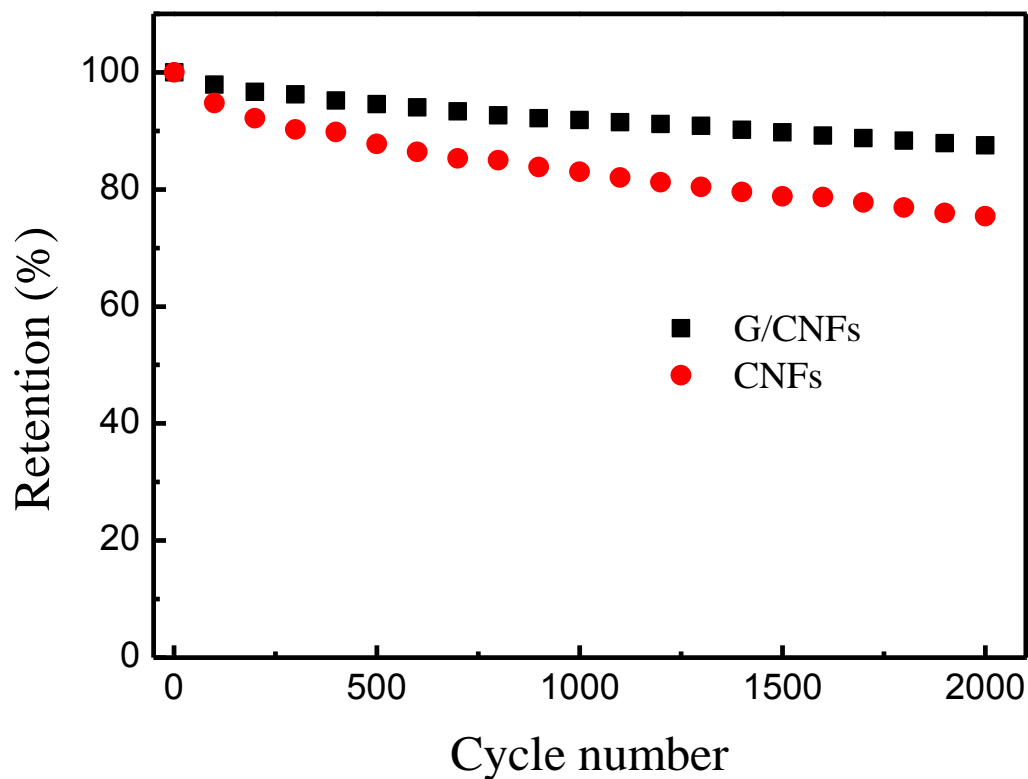
Figure 5.9. Cycling performance of the G/CNFs at a constant current density of 2.5 A/g.

5.4.   Summary

Successful synthesis and structural/electrochemical characterization of a novel porous G/CNF-based electrode material for use in high-performance supercapacitors has been demonstrated. During the process, the porous G/CNFs have been successfully synthesized by electrospinning the solution of PAN/DMF dispersed with oxidized graphene nanosheets, followed by carbonization in a tubular quartz furnace. One of the major benefits of the study is that the graphene nanosheets with excellent 2D nanostructures and electrical properties can be embedded along with CNFs to achieve attractive chemical structure and superior surface morphology. The

excellent connectivity of the graphene nanosheets embedded in carbonized PAN nanofibers significantly improved the specific surface area and electrical conductivity of the resulting G/CNFs. These free-standing, flexible nanofiber mats can be directly used as electrodes in supercapacitors without the aid of polymer binder. The novel porous G/CNF films exhibit superior electrochemical properties for potential use in high-capacitance EDLCs. New technical routes are still needed to enhance the capacitance retention ratio of such novel G/CNF-based supercapacitors for potential use in electrical energy conversion and storage.

CHAPTER 6. HIGH-PERFORMANCE POROUS ELECTRODES FOR PSEUDOSUPERCAPACITORS BASED ON GRAPHENE-BEADED CARBON NANOFIBERS SURFACE-COATED WITH NANOSTRUCTURED CONDUCTING POLYMERS

6.1.   Introduction

Novel hierarchical continuous G/CNF films had been successfully synthesized and characterized Chapter 5 for use as electrode materials of supercapacitor. In this chapter, a rational technical route was further devised to introduce the unique pseudocapacitive effect to the G/CNF-based electrode materials via coating an ultrathin layer of thorn-like PANI nanorods onto the G/CNFs to form a ternary multifunctional electrode material: PANI-coated G/CNFs (PANI-G/CNFs). Such porous, multifunctional PANI-G/CNF films were expected to carry noticeable pseudocapacitive effect due to the synergetic interaction of nanostructured PANI and CNT/CNF substrate, superior intrinsic connectivity, and very high specific surface area. SEM was employed to characterize the unique morphology and microstructure of the G/CNFs and PANI-G/CNFs. The electrochemical behavior of the novel electrode materials was characterized based on a two-electrode cell, which was made of a pair of electrodes 1.0 cm^2 G/CNFs and PANI-G/CNF films. The electrochemical performance was tested in a 1 M H_2SO_4 aqueous solution. Cyclic voltammetry (CV) and galvanostatic charging/discharging (GCD) behavior were studied on a BT-2000 battery tester (Arbin Instruments, TX) to evaluate the capacitive behavior and specific capacitance of the hierarchical electrodes, respectively. The microstructural and electrochemical results of the G/CNF and PANI-G/CNF electrodes are discussed in consequence.

6.2. Experimental

6.2.1. Materials

Source materials of PAN powders, graphene nanosheets, ammonium persulfate (APS), and DMF solvent utilized for synthesis of G/CNFs and PAN-G/CNFs in this chapter have been described in Chapters 4 and 5. No further purification and treatments have been applied before use.

6.2.2. Preparation of G/CNF and PANI-G/CNF films

Successful fabrication of the precursor graphene-beaded CNFs (G/CNFs) has been described in Chapter 5. In this study, the as-synthesized precursor G/CNFs (~0.38 g) was coated with thorn-like PANI nanorods to form ternary porous PANI-G/CNFs via *in-situ* polymerization of aniline monomer in aqueous solution as described in Chapter 4. During the process, as-prepared G/CNF mats were first immersed into 200 mL aniline (0.03 M) / H_2SO_4 (1 M) solution for 6 h in an ice bath (~0 – 5 °C). Then, APS dissolved in another 50 mL 1 M H_2SO_4 solution was slowly added dropwise into the mixture. The molar ratio of aniline/APS was adjusted to 4:1. The mixture had been continuously stirred for 12 h, and the color of the solution slowly changed to dark green. After polymerization, the resulting precipitates were filtered out and washed sequentially with deionized water and acetone. Finally, the wet product had been dried in a vacuum oven at 80 °C for 10 h. The areal mass density of PANI-G/CNFs was calculated about 1.5 mg/cm^2. The mass of PANI was about 52% based on the weight difference of the G/CNFs before and after polymerization.

6.2.3. Microstructural and electrochemical characterization

The surface morphology of as-synthesized G/CNFs and PANI-G/CNFs was analyzed by utilizing SEM. Electrochemical characterization was performed using a two-electrode cell setup. 1 M H_2SO_4 aqueous solution and stainless steel wire mesh were used as the electrolyte and the current collector, respectively. The electrochemical performance of the supercapacitor cells was evaluated by CV, GCD, and EIS as used in the previous chapters. The CV and GCD curves were obtained by using a BT-2000 battery tester (Arbin Instruments, TX), which were further used for evaluation of the capacitive behavior and calculation of the specific capacitance of the porous G/CNF and PANI- G/CNF electrodes. The CV response of the synthesized porous electrodes was determined at varying scan rate from 5 to 50 mV/s; the galvanostatic charge/discharge testing was performed in the potential range of -0.2 - 0.8 V at varying current density from 0.15 to 15 A/g. The three-electrode EIS setup was employed for the electrochemical impedance measurements in this study. A saturated calomel electrode was used as the reference electrode. The measurements were taken over a frequency range of 100 kHz - 0.01 Hz by an Electrochemical Multiplexer ECM8 (Gamry Instruments, Inc., PA).

6.3. Results and Discussions

6.3.1. SEM micrographs

The surface morphologies and microstructures of electrospun G/CNFs and PANI-G/CNFs were characterized by SEM. Compared to the Figs. 6.1 of discrete graphene coated with PANI, Figs. 6.2 (A) and (B) show the typical SEM micrographs of G/CNFs with unique continuous nanostructural configuration at low and high magnifications, respectively. As shown in Fig. 6.2 (B) and discussed in Chapter 5, G/CNFs apparently consisted of two constituents, i.e., carbonized

PAN nanofibers and unfolded, opened graphene nanosheets with porous structures. It can be observed that all the graphene nanosheets were firmly connected to the CNF segments at two ends. The graphene nanosheets and CNF segments could be connected by the covalent C-C bonds, which can noticeably enhance the electrical conductivity and specific surface area as shown in the experimental results in Chapter 5 (Zhou and Wu, 2013). The graphene nanosheets were typically 6-8 nm in thickness and 1-5 micron in-planar size, while the CNFs had an average diameter of 200 - 400 nm.
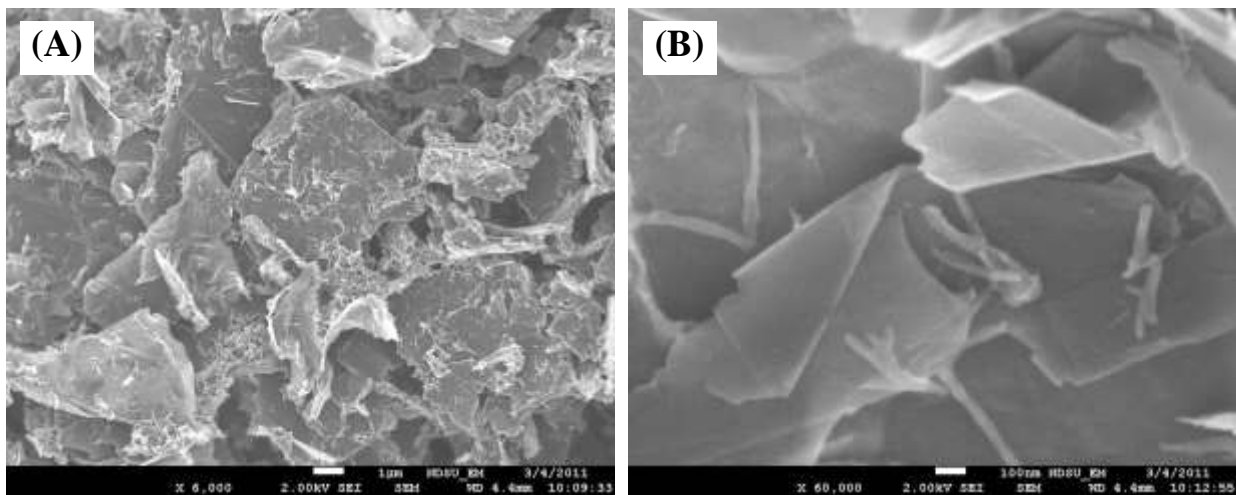
Figure 6.1. SEM micrographs of graphene coated with thin PANI layers.
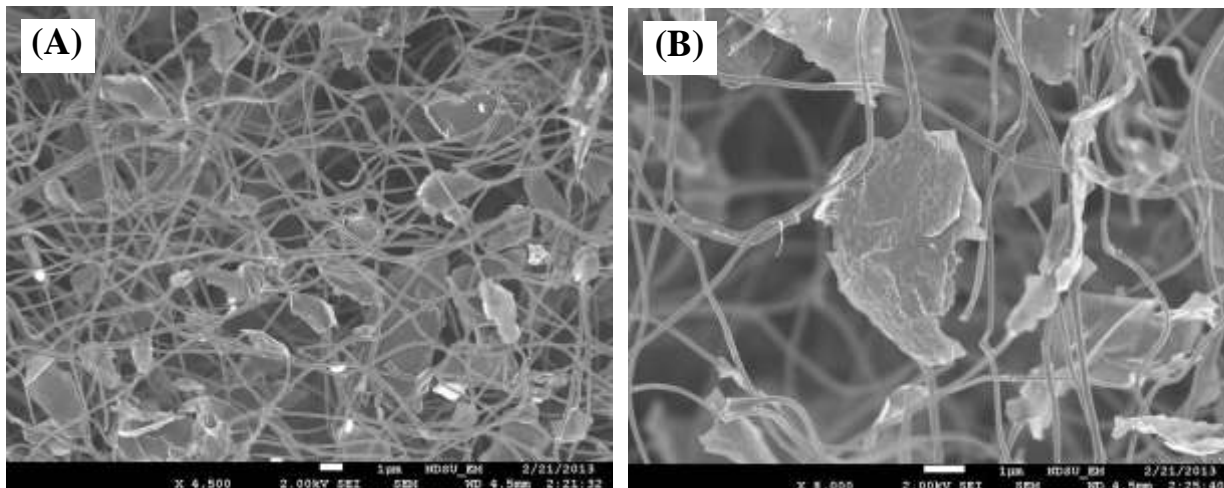
Figure 6.2. SEM micrographs of carbonized electrospun G/CNFs nanofibers at low (A) and high (B) magnification, respectively.

The hierarchical nanostructure of PANI-G/CNFs was obtained via *in situ* polymerization of aniline monomer onto the G/CNFs in aqueous solution as shown in Fig. 6.3. It can also be found from Fig. 6.3 (C) that the dense thorn-like PANI nanorods were coated evenly onto the surfaces of both the CNFs and graphene nanosheets. The diameter of the coated PANI nanorods was about 30-50 nm as estimated from the high-resolution SEM micrograph as shown in Fig. 6.3 (D). According to Kaner's mechanistic study (Huang and Kaner, 2004), the diameter of PANI nanorods can be tailored by adjusting the concentration of aniline used in the polymerization process.
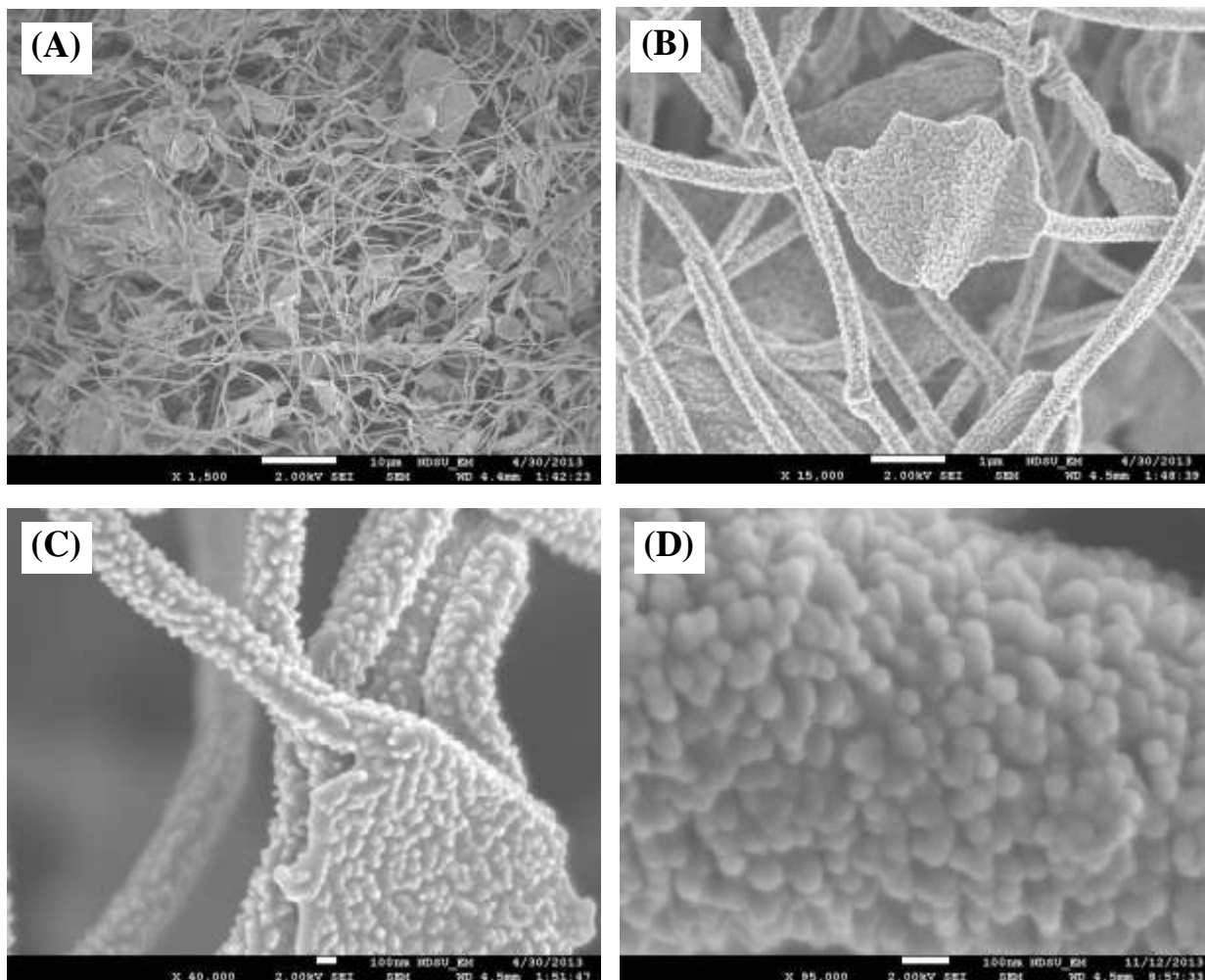
Figure 6.3. SEM micrographs of graphene-CNFs coated PANI nanorods at low (A and B) magnifications and high (C and D) magnifications, respectively.

In addition, the densely stacked PANI nanorods were interconnected each other to form a highly porous ultrathin surface layer, resulting in high surface area and very efficient contact with the electrolyte solution. Serving as the supporting template for deposition of PANI nanorods, G/CNFs can be exploited as the conductive filler and electrically-conductive channels of the electrodes in supercapacitors. Thus, such unique microstructure of G/CNFs can improve the electrochemical performance and mechanical stability of PANI-G/CNFs when used as porous electrodes in supercapacitors.

6.3.2. EIS characterizations

Similar to the EIS tests performed in Chapters 4 and 5, the EIS method was further employed to characterize the electrochemical impedance properties of the porous electrode materials based on G/CNFs and PANI-G/CNFs based on a three-electrode cell. Figure 6.4 shows the typical Nyquist plots of both the G/CNF and PANI-G/CNF electrodes. The Nyquist plots consist of one incomplete semicircle and a nearly vertical line, which represent the charge transfer resistance of the electrode (R_{ct}) and the diffusion behavior of ions in the electrode pores, respectively (Ryu et al., 2002; Lai et al., 2012). As estimated from the intercept in the Fig. 6.4 insert, the equivalent series resistance (R_s) of G/CNF and PANI-G/CNF electrodes is about 1.6 and 2.0 Ω, respectively. In the mid- to low-frequency region, the vertical lines of G/CNF and PANI-G/CNF electrodes represented an ideal capacitive behavior with the faster diffusion of ions in electrolyte. As calculated from the diameter of semicircles on the real axis in the Fig. 6.4 insert, the R_{ct} values of G/CNF and PANI-G/CNF electrodes are about 0.7 and 0.9 Ω, respectively. The R_{ct} resistance of PANI-G/CNF electrode is much lower than the values of resistance reported in the literature for graphene nanosheets and PANI nanoworms (20.0 Ω) (Luo et al., 2013), nanorod-PANI-graphene composite (7.5 Ω) (Hu et al., 2012), and PANI/graphitized electrospun carbon fibers (PANI/GECFs) (2.4 Ω) (He et al., 2012). The low R_{ct} resistance is attributed to the unique graphene-beaded structure (Fig. 6.2 (B)) and excellent electrical conductivity of G/CNFs.
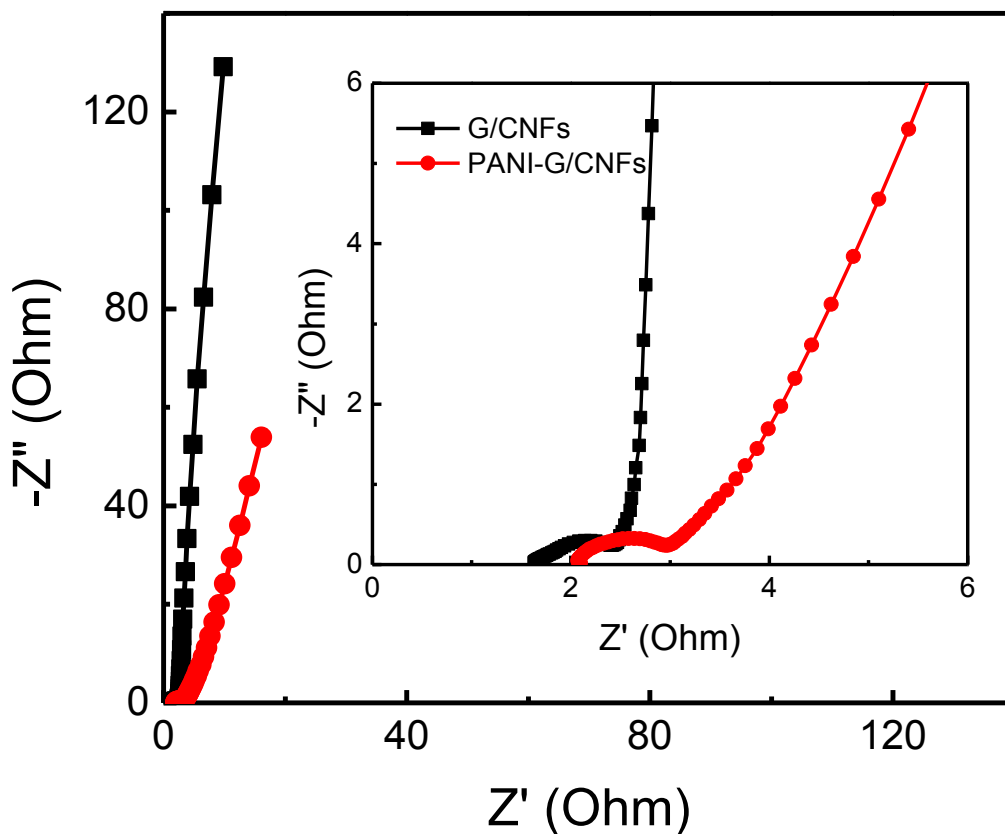
Figure 6.4. Nyquist plots for G/CNF and PANI-G/CNF cells in 1 M H_2SO_4 solution in the frequency range of 100 kHz - 0.01 Hz. Z' and Z'' are the real and imaginary parts of the complex impedance, respectively.

6.3.3. CV characterizations

Similar to the electrochemical characterizations performed in the previous chapters, CV and GCD measurements were further utilized to characterize the electrochemical performance of G/CNFs and PANI-G/CNFs in a two-electrode supercapacitor cell. Figure 6.5 shows the typical CV curves of G/CNFs, PANI-G/CNFs, and stainless steel mesh in a potential range from -0.2 to 0.8 V at a scan rate of 10 mV/s. The CV shape of G/CNFs was nearly rectangular along the time-potential axis and exhibited a rapid current response to voltage reversal, which occurred at each

end of the potential, indicating that G/CNFs had an excellent double-layer electrochemical capacitance.
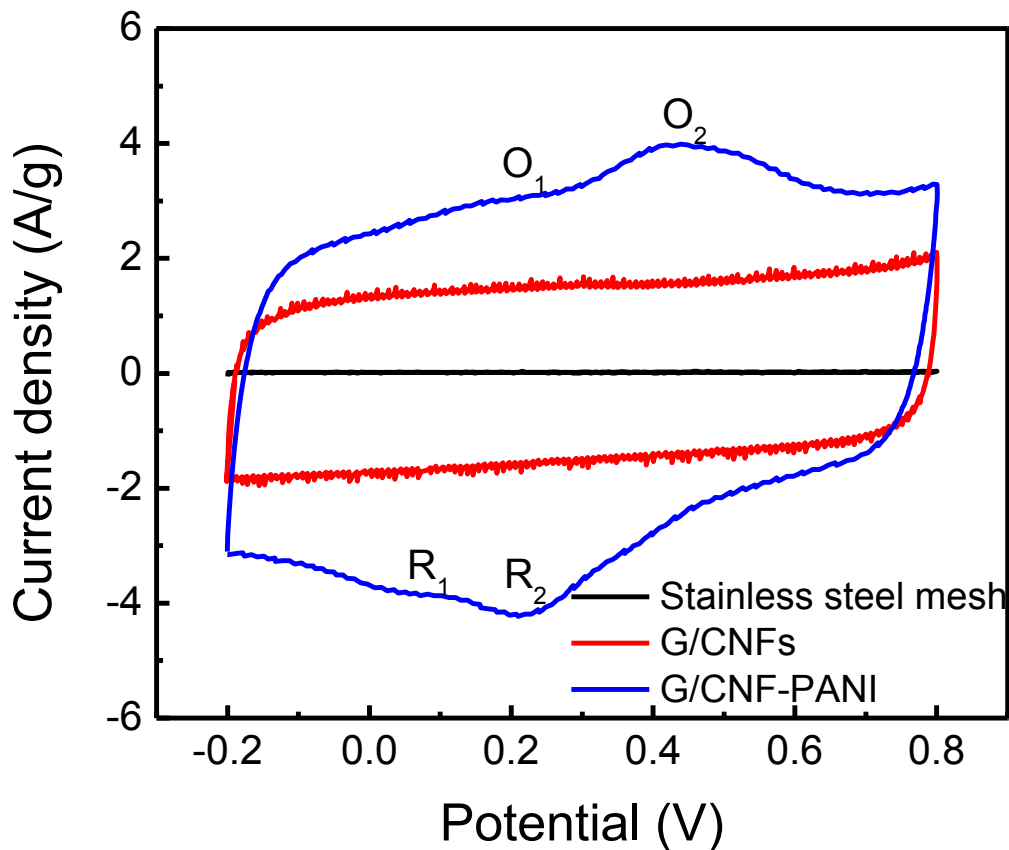
Figure 6.5. CV curves of the G/CNFs, PANI-G/CNFs, and stainless steel mesh at a scan rate of 10 mV/s in 1 M H_2SO_4 solution in the potential range from -0.2 to 0.8 V.

Similar to these of PANI-CNT/CNF electrodes in Chapter4, the CV curves of PANI-G/CNFs clearly exhibited two pairs of redox peaks (O_1/R_1 and Q_2/R_2), revealing the pseudocapacitive behavior of PANI, which is different from these of G/CNF electrodes. The peaks of O_1/R_1 were attributed to the reversible redox transition of PANI between the leucoemeraldine and polaronic emeraldine forms; whereas the peaks of O_2/R_2 represented the reversible Faradaic transformation of PANI between the emeraldine and pernigraniline forms (Fan et al., 2013; Wang

et al., 2006; Li et al., 2013). Although substantial quantities of PANI nanorods were coated onto G/CNFs, nearly rectangle-shaped CV curves of PANI-G/CNFs indicated that the resulting ternary PANI-G/CNFs carried excellent electrochemical capacitive behavior in supercapacitors (Numao et al., 2009).

Furthermore, the reversibility of the redox reactions was determined by the potential difference between the oxidation and reduction peaks ΔE_{OR} (Wang et al., 2007). The values of 0.11 and 0.18 V were obtained for $\Delta E_{O_1 R_1}$ and $\Delta E_{O_2 R_2}$ of PANI-G/CNFs, respectively. These values are lower than the values of 0.25 and 0.50 V for pure PANI fibers (Liu et al., 2013). This observation indicates a high reversibility for the PANI-G/CNF electrodes, which can be attributed to the low R_{ct} resistance. It is also noted that the area formed by the CV loop and the current density of PANI-G/CNFs are both much larger than those of G/CNFs at the same scan rate, indicating a higher specific capacitance. The remarkable increases for the PANI-G/CNFs are obviously associated with the doping of PANI nanorods onto the surface of G/CNFs and the presence of G/CNFs acting as the electrically conductive channels. Figure 6.6 presents the CV curves of the PANI-G/CNFs in 1 M H_2SO_4 aqueous solution at varying scan rates. As the scan rates increased from 5 to 50 mV/s, the cathodic peaks of these curves shifted to the side of higher positive potentials, while the anodic peaks shifted to the side of lower negative potentials. These shifts could be attributed to a slight increase of the internal resistance at a high scan rate (Wang et al., 2006; Fan et al., 2013; Luo et al., 2013). At a high scan rate, once the electrolyte ions fast diffuse to electrode to react, the response current will substantially increase. Furthermore, the current-density response of PANI-G/CNFs clearly increased with increasing scan rate, which indicates a good rate capability for the PANI-G/CNF electrodes in supercapacitors.
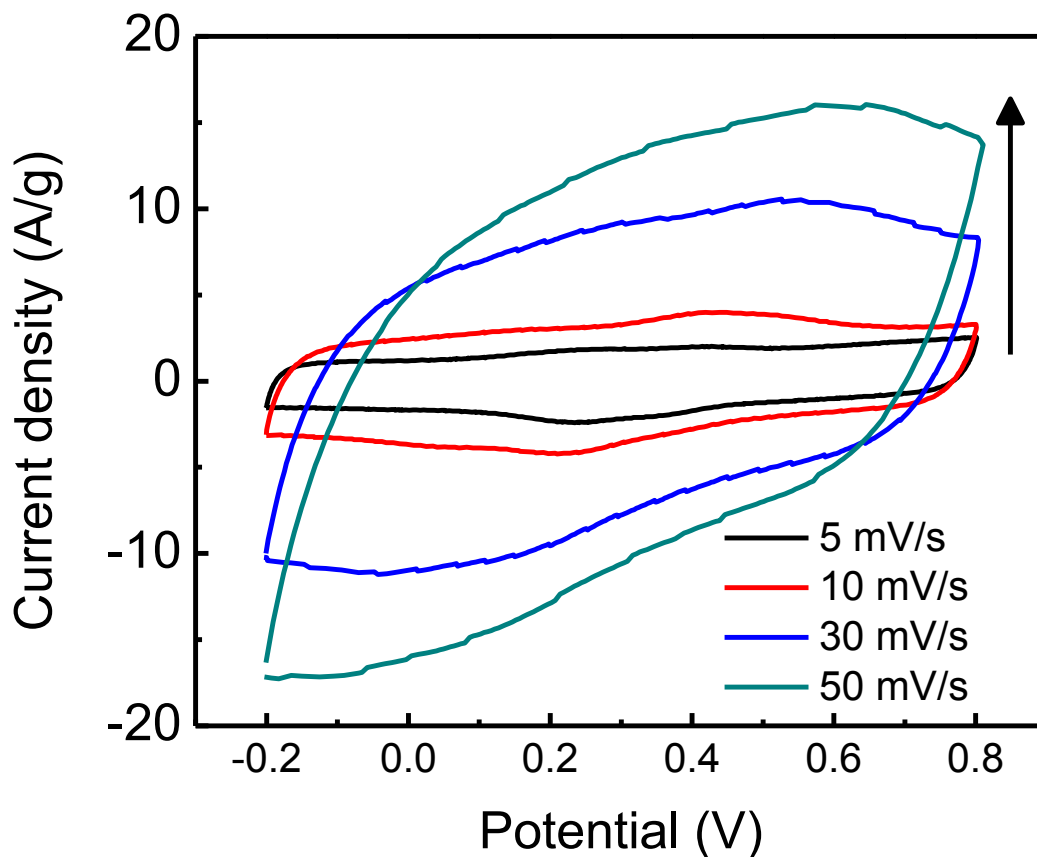
Figure 6.6. CV curves of the PANI-G/CNFs at different scan rates in 1 M H_2SO_4 solution in the potential range from -0.2 to 0.8 V.

6.3.4. GCD characterizations

To calculate the specific electrochemical capacitance, the GCD plot was used to evaluate the synthesized electrode materials at a constant current density of 0.3 A/g with a potential window of -0.2 to 0.8 V, as shown in Fig. 6.7. The curve of the G/CNFs exhibits a linear and symmetrical shape, which implies that the electrode has excellent electrochemical reversibility as of an ideal EDLC. In contrast, the GCD plot of the PANI-G/CNFs shows a little deviation from linearity due to the Faradaic charge-transfer accompanied with the double-layer charging/discharging process. The voltage jump at the beginning of the discharge curve is related to the internal resistance (also

called IR drop) of the electrode material. No obvious IR drops on the discharge curve of G/CNFs were measured, but a little IR drop was observed from the discharge plot of PANI-G/CNFs, representing the low internal electrical resistance of the capacitors as shown in Fig. 6.4.
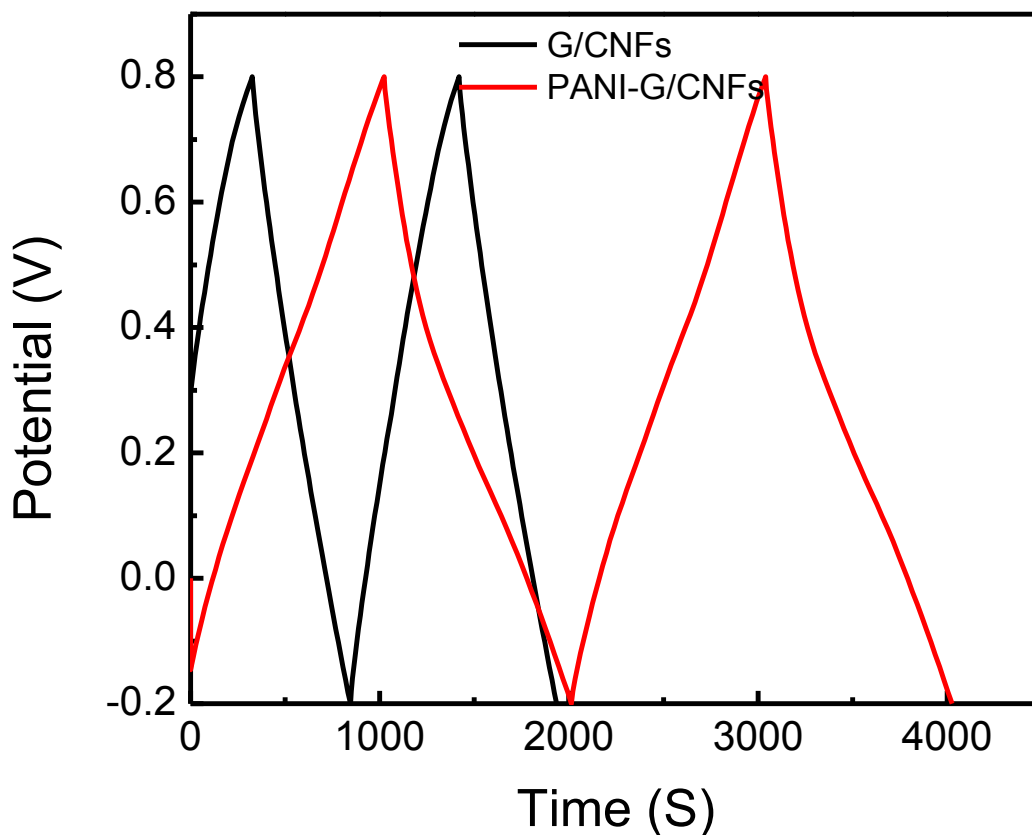
Figure 6.7. GCD curves of G/CNFs and PANI-G/CNFs at a constant current density of 0.3 A/g.

The above electrochemical measurements clearly demonstrated that the porous G/CNF backbone networks effectively suppressed the internal electrical resistance of the PANI-G/CNF electrodes, resulting in an improved electrochemical reversibility and charge-discharge efficiency compared to those of the traditional graphene/PANI electrode materials (Yan et al., 2010; Zhou and Wu; 2013; Lai et al., 2012; Luo et al., 2013; Li et al., 2013; Wang et al., 2007; Basnayaka et

al., 2013). The average specific capacitance values, C_{avg} (F/g), of the resulting electrode materials were calculated from the discharge process according to the relation (2.4).

The C_{avg} of PANI-G/CNFs was calculated as high as 591 F/g at a current density of 0.3 A/g, which is much higher than the capacitance value of 309 F/g for G/CNFs. Such a high value of pseudocapacitance of PANI-G/CNFs may be derived from the high theoretical value of pseudocapacitance (750 F/g) of PANI and the synergistic effect between the thorn-like PANI nanorods and G/CNFs (Lota et al., 2004; Kumar et al., 2012). A high value of pseudocapacitance (520 F/g) of pure PANI film on Pt electrode has been measured by Cong et al. (Cong et al., 2013). In the present study, 52 wt. % of PANI coated the G/CNFs. Without consideration of the synergistic effect between the PANI nanorods and G/CNFs, the theoretical specific capacitance of the PANI-G/CNFs can be calculated as high as 419 F/g, i.e., [309 F/g (G/CNFs) × 48 wt. % + 520 F/g (pure PANI) × 52 wt.%]. Thus, the specific capacitance increased by 172 F/g, i.e., (591 F/g-419 F/g), reaching 41% enhancement compared to the theoretical capacitance. Figure 6.8 shows the variation in the specific capacitance of PANI-G/CNFs as a function of the current density. It is noted that the specific capacitance of PANI-G/CNFs decreased with increasing current density. The maximum specific capacitance of 637 F/g is obtained at the low current density of 0.15 A/g. PANI-G/CNFs still maintained a high value of specific capacitance of 478 F/g (only 25% of decrease from 637 F/g) even at a high current density of 6 A/g. Furthermore, the value of capacitance of PANI-G/CNFs is larger than those of previously reported graphene/PANI composites (Lai et al., 2012; Luo et al., 2013; Li et al., 2013; Kumar et al., 2012). The reason is that the graphene-beaded CNF backbone networks not only aided the charge pathway inside the PANI-G/CNFs, but also enhanced the specific surface area and electrical conductivity of the electrode.
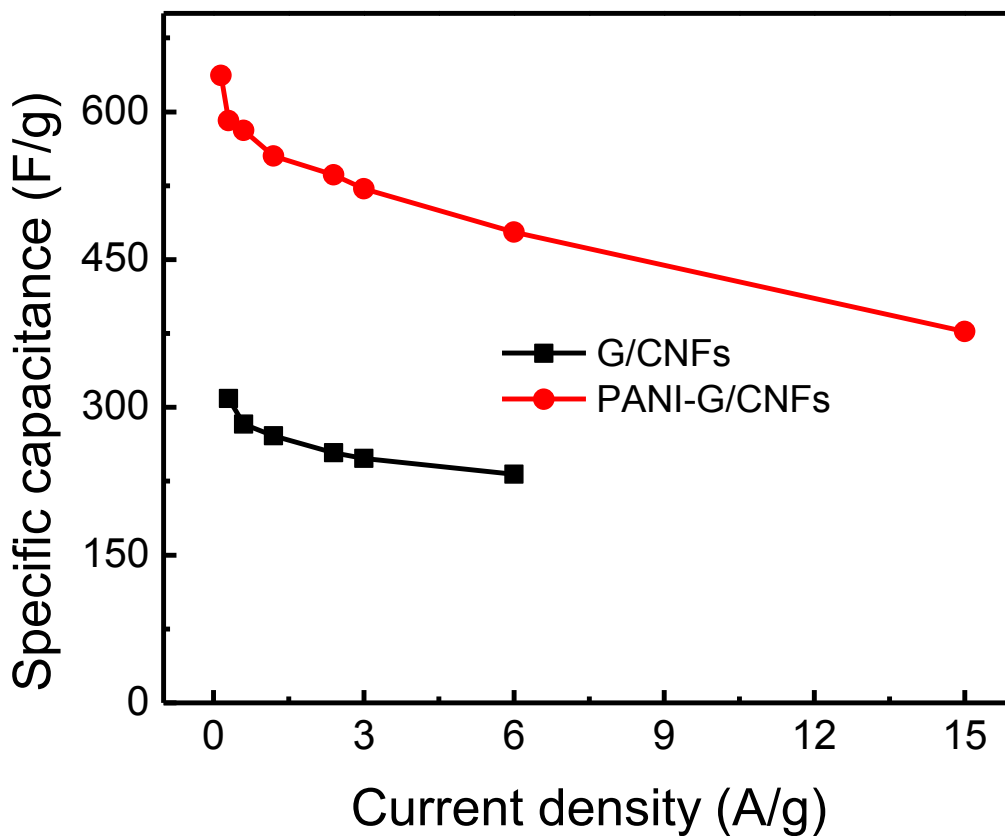
Figure 6.8. Specific capacitance of PANI-G/CNFs as a function of current density.

6.3.5. Energy and power densities

In all the electrochemical energy storage devices, energy and power densities are two major measures of their performance. Energy density describes the amount of energy that can be stored per unit mass while power density represents how fast the energy can be stored or released. The energy density, E_d (Wh/kg), and power density, P_d (W/kg), delivered by the electrodes of a supercapacitor are calculated by the relations (2.5) and (2.6).

Figure 6.9 is the Ragone plot of the supercapacitors with G/CNFs and PANI-G/CNFs as electrode materials, respectively. The maximum energy density of PANI-G/CNF-based

supercapacitors is as high as 88 Wh/kg at a power density of 150 W/kg, and the highest power density of G/CNFs is 6 kW/kg at an energy density of 32 Wh/kg. The PANI-G/CNF based supercapacitors also kept an excellent rate capability, with the energy density of 54 Wh/kg even at a high power density of 4.9 kW/kg. The measured power and energy densities of PANI-G/CNFs were much higher than those of current commercially available supercapacitors of 1 - 10 Wh/kg and 1,000 - 2,000 W/kg (Zhao et al., 2011).
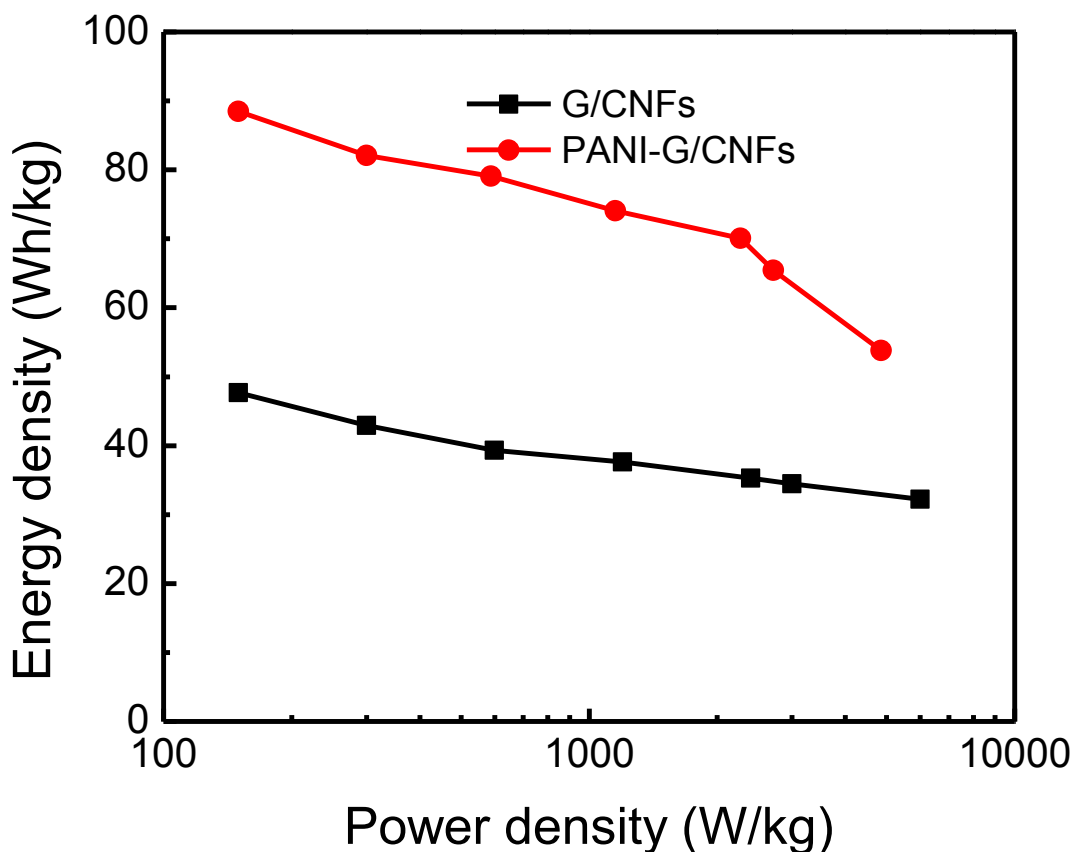
Figure 6.9. Ragone plots of G/CNF and PANI-G/CNF electrodes.

6.3.6. Cycling performance

Figure 6.10 further shows the cycling performance of the PANI-G/CNF based pseudosupercapacitors at a current density of 15 A/g. The capacitance only dropped about 13%

from 377 to 327 F/g after 1,000 cycles, which is competitive with the cycling stabilities of supercapacitors reported recently in the literature (Yan et al., 2010; Fan et al., 2013; Cong et al., 2013; Cheng et al., 2013).
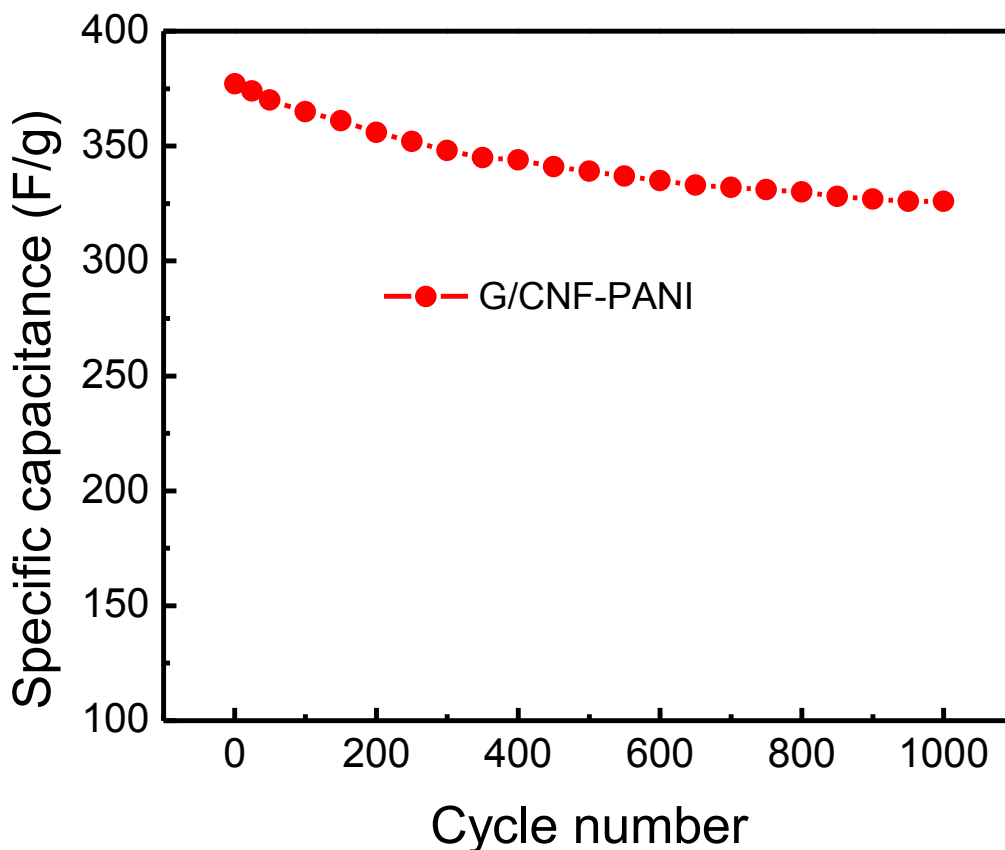
Figure 6.10. Cycle life tests of the PANI-G/CNF electrodes measured at a constant current density of 15 A/g.

The loss of specific capacitance of PANI-G/CNF based pseudosupercapacitors may be attributed to the increasing electrolyte solution resistance, the contact resistance between electrode and electrolyte, and the deterioration of ion diffusion (Cong et al., 2013). All the experimental results reported in this chapter have been published in *Journal of Power Sources* in 2014 (Zhou and Wu, 2014).

6.4. Summary

A rational experimental route has been successfully formulated for synthesis of heterogeneous, porous PANI-G/CNFs for use as low-cost high-performance electrode materials for supercapacitors. Electrochemical characterization indicated that such novel nanofibrous electrode materials possessed the high specific capacitance of 591 F/g at the current density of 0.3 A/g and the high energy density of 54 Wh/kg at the high power density of 4.9 kW/kg. These experimental results demonstrated that the hybrid, porous, multifunctional PANI-G/CNFs exhibited excellent electrochemical performance for use in electrochemical energy storage. In particular, the present PANI-G/CNFs can be utilized as low-cost, flexible, high-performance electrodes of supercapacitors without the need of conductive binders. Comparative study indicated that the excellent electrochemical performance of the PANI-G/CNFs was resulted from the unique heterogeneous G/CNF network backbones coated with thorn-like PANI nanorods. The G/CNFs provided a conductive network with a high specific area, while the coated PANI nanorods further increased the specific area and activated the excellent pseudocapacitive effect. The synergistic effect of the heterogeneous conductive G/CNF network backbones and the pseudocapacitive PANI nanorods substantially enhanced the energy and power densities of the resulting flexible, nanofibrous electrode materials. Since the synthesis of the present electrode material only consisted of three consecutive low-cost processes of electrospinning, controlled pyrolysis and *in situ* polymerization, manufacturing of the present high-performance electrode materials can be conveniently scaled up. This would greatly benefit the potential industrial applications of the present porous, flexible, multifunctional electrode materials in broad electrochemical energy storage devices.

CHAPTER 7. EXPERIMENTAL STUDY ON PARAMETER DEPENDENCY OF CONIC ANGLE IN ELECTROSPINNING AND SCALABLE FABRICATION OF CORE-SHELL NANOFIBERS

7.1.   Introduction

This chapter is divided into two sections. The first section is the experimental study on the dependency of conic angle of an electrospun jet upon the process and material parameters. Based on a simple needle-based electrospinning setup, PAN/DMF solutions with varying PAN concentrations were used as the model systems and electrospun into nanofibers at different high DC voltages, flow rates, and needle diameter. The variations of jet conic angle with the PAN concentration and flow rate were determined via digital image analysis, and the potential electrohydrodynamic mechanisms were explored. In addition, the dynamic and transient shear viscosities of the PAN/DMF solutions were characterized by using a parallel-plate rheometer (TA Instruments, New Castle, DE) at varying shear rates; related shear thinning phenomenon was observed and rationally explained. The study provided the experimental evidence useful for understanding the scaling properties of the electrohydrodynamic jet motion for controllable electrospinning and process modeling.

The second section is to describe a novel needleless emulsion electrospinning method for scale-up fabrication of ultrathin core-shell fibers, in which PAN and isophorone diisocyanate (IPDI) were used as the model chemicals for producing such core-shell fibers. These ultrathin core-shell fibers can be incorporated at the interfaces of polymer composites for interfacial toughening and self-repairing due to polymerization of IPDI triggered by environmental moisture.   Optical microscopy, SEM, and FT-IR spectroscopy were used to characterize the core-shell nanostructures.

Dependencies of the fiber diameter on the PAN/IPDI concentration, wire spacing, and wire diameter were examined. Discussion of the experimental results and prospective of the research were made.

7.2. Parameter Dependence of Conic Angle of Nanofibres during Electrospinning

7.2.1. Experimental

7.2.1.1. Preparation and characterization of PAN/DMF solution

The present experimental study was to correlate the conic angle of the electrospun jet envelope (see Fig. 7.1) to the process and material parameters employed in electrospinning, including polymer concentration in the electrospinnable solution, applied DC voltage, flow rate and needle diameter. The study of such correlations and parameters is important to understand the fundamental phenomenon of the electrospinning process, controllable nanofiber fabrication and related process modeling. In this study, PAN/DMF solutions with varying PAN concentration were utilized as the model solutions for electrospinning nanofibers at different high DC voltages, flow rates, and needle inner diameters. Particular selection of the PAN/DMF solutions was due to the fact that PAN nanofibers are technically important, since they could be used as the precursor for producing CNFs with superior mechanical properties (Liu et al., 2009).
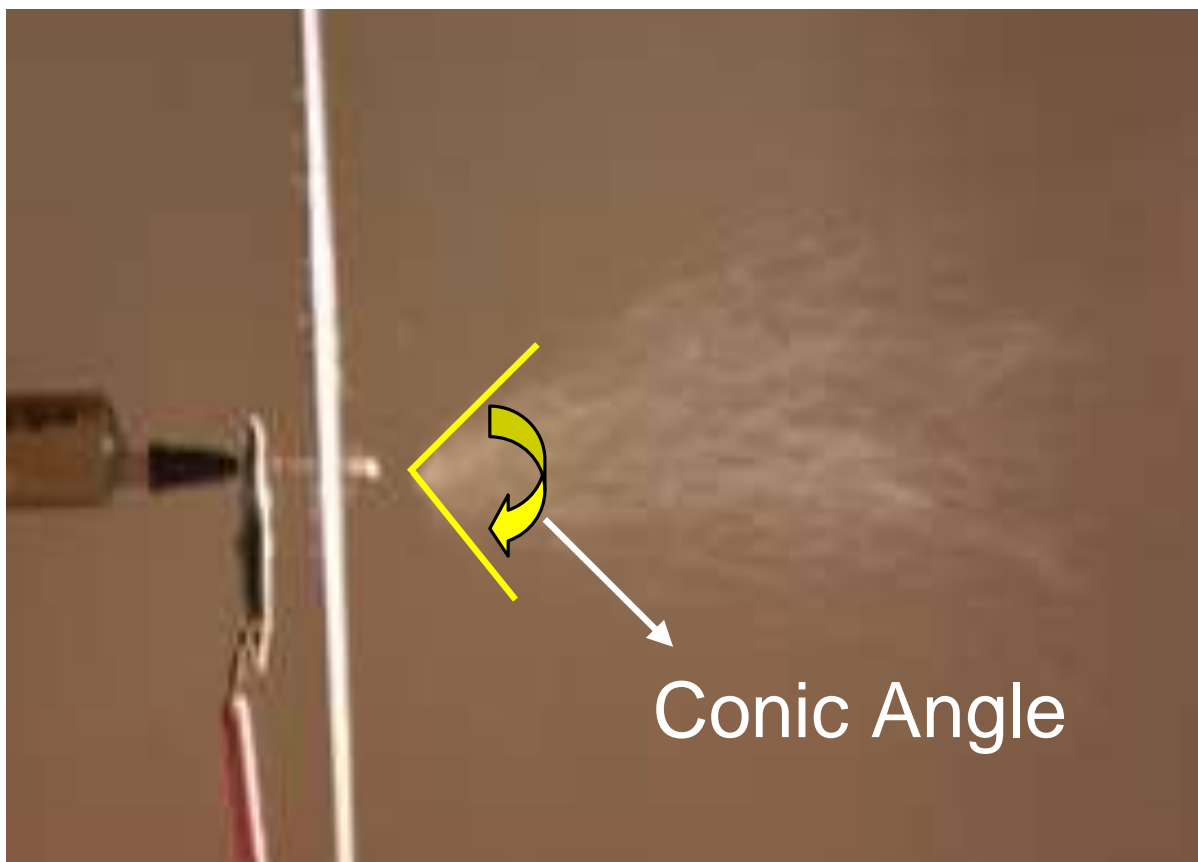
Figure 7.1. The formation of conic angle of nanofiber envelope during electrospinning of a PAN/DMF solution with PAN concentration of 16 wt. %.

In this study, nine PAN/DMF solutions with varied PAN concentration in the range of 12 to 20 wt. % were prepared and used for electrospinning at different high DC voltages. Prior to electrospinning, the PAN powder was dissolved in DMF using a magnetic stirrer installed with a hotplate; each mixture with a particular PAN concentration had been stirred at 80 °C for 6 h to prepare a well-electrospinnable solution. The dynamic and transient shear viscosities of the PAN/DMF solutions were characterized using a TA ARG2 Rheometer (TA Instruments, New Castle, DE) in the ranges of circular frequency from 0.06 to 300 rad/s in the case of dynamic oscillating test mode and the shear rate from 1 to 1,000 s^{-1} in the case of transient shear test mode, respectively; the measured dynamic shear viscosity data were plotted in Fig. 7.2.

7.2.1.2.   *Measurement of conic angles of the electrospinning PAN/DMF nanofibers*

During the electrospinning process, a PAN/DMF solution was placed into a 10 ml plastic syringe installed with a blunt-end stainless steel needle with the size of 20-gauge or 22-gauge (inner diameters: 0.48 mm for 22-gaue needle and 0.65 mm for 20-gauge needle), and the syringe was fixed onto a digitally controlled syringe pump (Fisher Scientific Inc., Pittsburgh, PA); two laboratory-made rectangular aluminum plates (51 cm×31 cm) were placed in parallel with a distance of ~28 cm, of which one plate was electrically grounded and served as the nanofiber collector, and the other was isolated and used to generate a uniform electrostatic field in the space between the two plates. The latter was machined with an aperture letting the needle tip of the syringe pass through. Once a high DC voltage was applied between the needle and the grounded nanofiber collector through a positive high-voltage DC power supply (Gamma High Voltage Research, Inc., Ormond Beach, FL), a nearly uniform electrostatic field with the DC voltage in the range of 0 - 30 kV was established. The flow rate of the solution was varied to study its influence on the conic angle of the nanofiber envelope. Once a stable conic angle was formed under certain processing and material parameters, the nanofiber (jet) envelope was captured by using a digital camera. The conic angles were then measured digitally from the micrographs of the nanofiber envelopes and tabulated in Tables 7.1 and 7.2 and plotted in Figs. 7.3-7.5.

7.2.2. Results and discussions

7.2.2.1.   *Dynamic and transient shear viscosities of the PAN/DMF solutions*

Figure 7.2 shows the dynamic and transient shear viscosities of the PAN/DMF solutions as a function of shear rate at five typical PAN concentrations. In the case of either dynamic oscillating test mode or transient shear test mode, given a shear rate, the experimental viscosity

increases with increasing PAN concentration as commonly observed in other polymer systems. At a fixed PAN concentration, the dynamic or transient shear viscosity is almost constant at relatively low PAN concentrations (e.g., 12%, 14% and 16%), while both viscosities decrease with increasing shear rate at the high PAN concentrations (e.g., 18% and 20%). In particular, when the shear rate is higher than 100 s^{-1}, the transient shear viscosity of the solutions with PAN concentrations of 18% and 20% decreases significantly and is even lower than those of the solutions with low PAN concentrations as shown in Fig. 7.2 (b). This phenomenon was mainly induced due to the shear-thinning effect typically observed in polymer solutions at high shear rate (Bird et al., 1987). In this case, the macromolecular chains of PAN are aligned and have no sufficient time to relax. Even though the liquid of electrospinning jet was under extensional stretching, the measured dynamic or transient shear viscosity could be justified to qualitatively estimate the dynamic extensional viscosity via a positive correlation between the two viscosities (Barnes and Roberts, 1992). One conclusion that can be drawn from the rheological measurements is that highly aligned molecular chains in polymer nanofibers can be achieved through spinning high-concentration polymer solutions (even polymer melts) at high transient drawing rate.
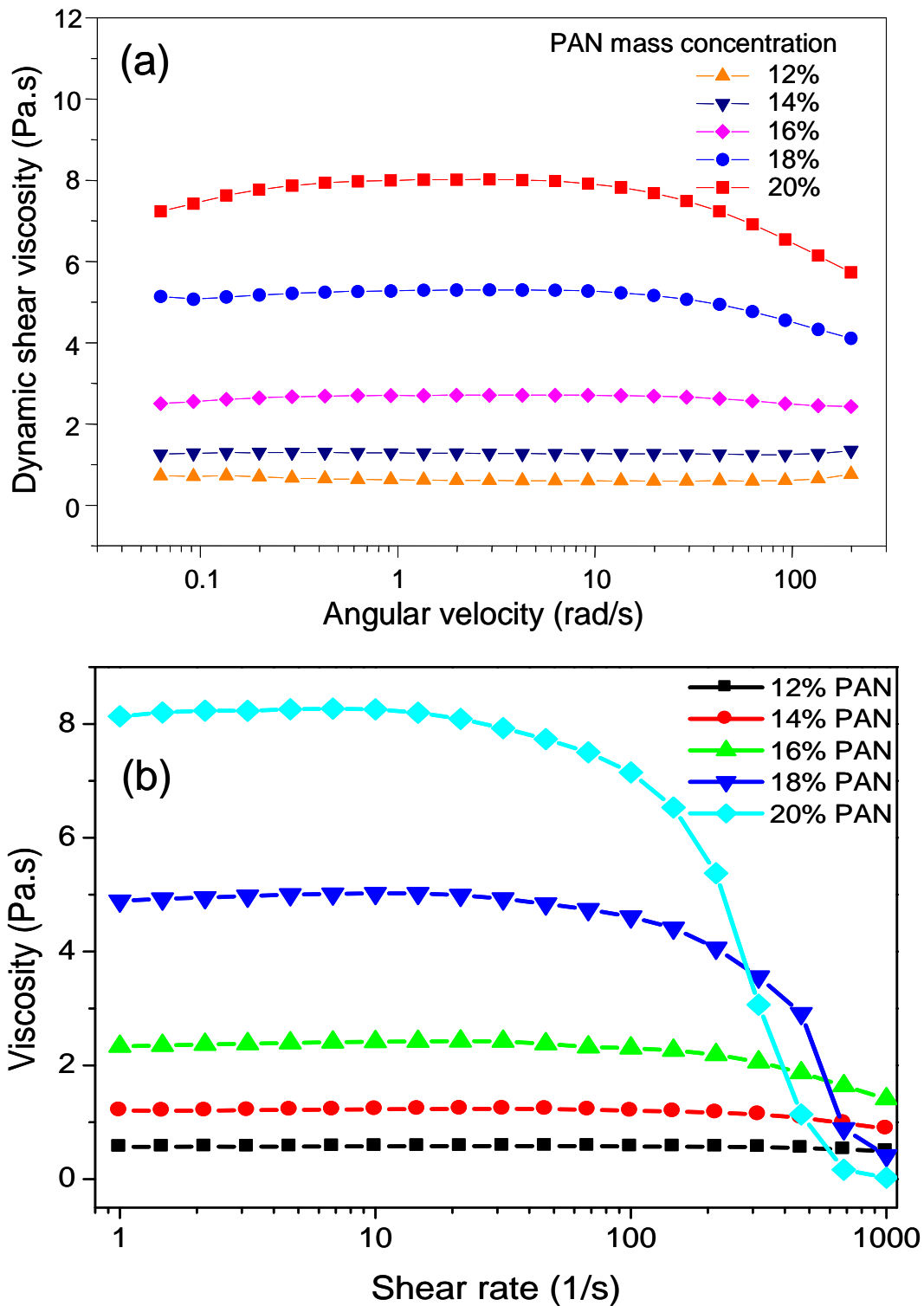
Figure 7.2. Variation of the dynamic and transient shear viscosities with varying angular velocity (a) and shear rate (b) for PAN/DMF solutions at different PAN concentrations.

7.2.2.2. *Effect of electric field on electrospinning conic angle*

Figure 7.3 shows that, for the PAN/DMF solution at a fixed PAN concentration of 16 wt. % and fixed flow rate of 0.6 ml/h, the conic angle increases nonlinearly with the increase of DC voltage. When installed with a needle with the inner diameter of 0.48 mm (22-gauge needle), the measured conic angle is from ~36.3° at the electric field of ~50 kV/m to ~160° at the electric field of 140 kV/m (Table 7.1). In contrast, when installed with a large-size needle with the inner diameter of 0.65 mm (20-gauge needle), the conic angle first increases with increasing electric field till 90 kV/m and then decreases with the further increase of electric field. This phenomenon could be induced due to the fact that at a large spinning area (i.e., the cross-sectional area of the needle) and fixed flow rate, the electrohydrodynamic behavior of an electrospinning jet was limited by the insufficient flow supply at high electric field.
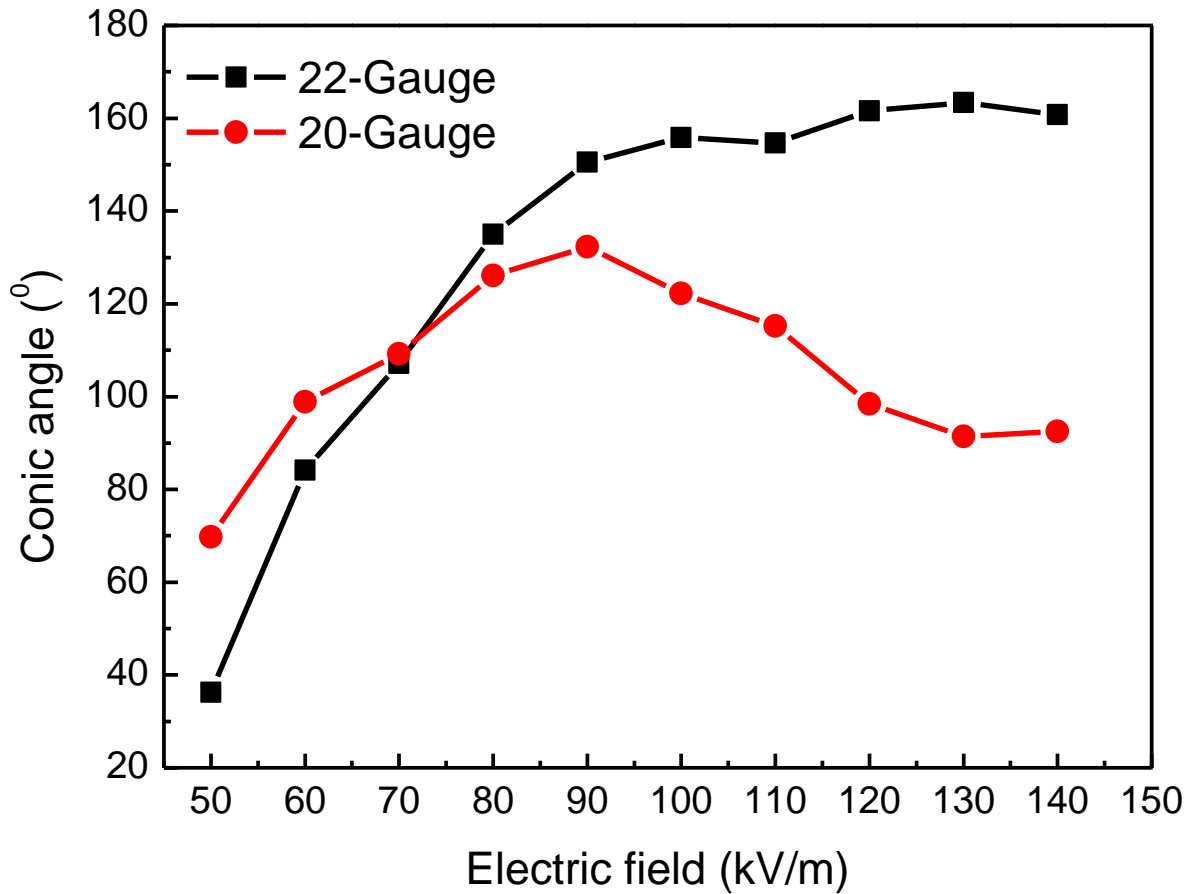
Figure 7.3. Experimental measurements of variation of the conic angle formed by PAN nanofibers with varying electric field (kV/m) at a constant PAN concentration of 16 wt.% and two needle inner diameters of 20- and 22-gauge, respectively.

In general, charges induced on an electrospinning jet increase with increasing electric field. From the micrographs listed in Table 7.1, it can be concluded that a higher DC voltage enhanced the electrostatic shielding effect of the charged whipping/bending jet, leading to a larger conic angle. To estimate the magnitude of axial electrostatic stress in a whipping/bending jet, as a simplified approach, consider a liquid torus with evenly distributed surface charge Q, torus radius r, and the axisymmetric axis of the torus parallel to the electrostatic field. The Coulomb's law determines the axial electrostatic stress of the jet as

$$\sigma = Q^2 / (4\pi\varepsilon_a V_0 r) \tag{7.1}$$

119

where ε_a is the dielectric constant of air, V_0 is the volume of the torus. This electrostatic stress decreases with increasing torus radius r. The difference of the electrostatic stress and the jet viscoelastic stress is the driving stress to stretch/thin the jet. Interestingly, this simple estimate shows that the axial electrostatic stress is independent on the jet cross-sectional area. In reality, the dynamic extensional viscosity of the liquid in the jet grows rapidly with solvent evaporation. Thus, it can be expected that the vigorous jet stretching would occur at the very beginning range of jet whipping/bending, where both the torus radius r and the jet viscosity are low, and they significantly decay with solvent evaporation. This has been validated by experimental observations using high-speed imaging techniques. A more detailed phenomenological description based on the discrete-bead models (Reneker et al., 2000; Yarin et al., 2001) gave the similar conclusions.
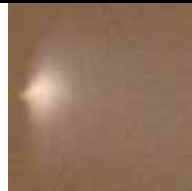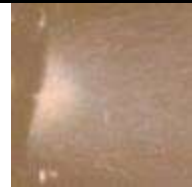
Table 7.1. Experimental measurements of variation of the conic angle for electrospinning PAN/DMF solution (16 wt. %) with varying electric field (needle inner diameter: 0.48 mm).

Electric Field (kV/m)	50	60	70	80	90
Micrographs					
Conic angle (º)	36.3	84.1	107.1	135	150.5
Electric Field (kV/m)	100	110	120	130	140
Micrographs					
Conic angle (º)	155.8	154.7	161.6	163.4	160.8

7.2.2.3.   *Effect of PAN concentration on the electrospinning conic angle*

Furthermore, given an electric field (~80 kV/m), measured conic angle of the nanofiber envelope decreases nonlinearly with increasing PAN concentration from ~160° at 12 wt. % to ~71° at 20 wt. %, as shown in Table 7.2 and Fig. 7.4 (with 22-gauge needle). In this case, the PAN/DMF solution with a low PAN concentration corresponds to a low viscosity. This means that the jet can be easily stretched under electrostatic interaction of the induced charges, i.e., a large conic angle can be detected accordingly. Though recent theoretical models (Reneker et al., 2000; Yarin et al., 2001) can predict the initial conic angle in some extent with simplified electrostatic interactions based on limited number of beads, a generalized scaling law is still desired to correlate the conic angle to the processing and material parameters.

Table 7.2. Experimental measurements of variation of the conic angle for electrospinning PAN/DMF solutions at different PAN concentrations (wt. %) under a constant electric field of 80 kV/m (needle inner diameter: 0.48 mm).

PAN concentration (wt. %)	12	13	14	15	16
Micrographs					
Conic angle (°)	158.6	164.8	165.7	155.8	135
PAN (wt. %)	17	18	19	20	
Micrographs					
Conic angle (°)	116.1	106.5	91.2	71.3	
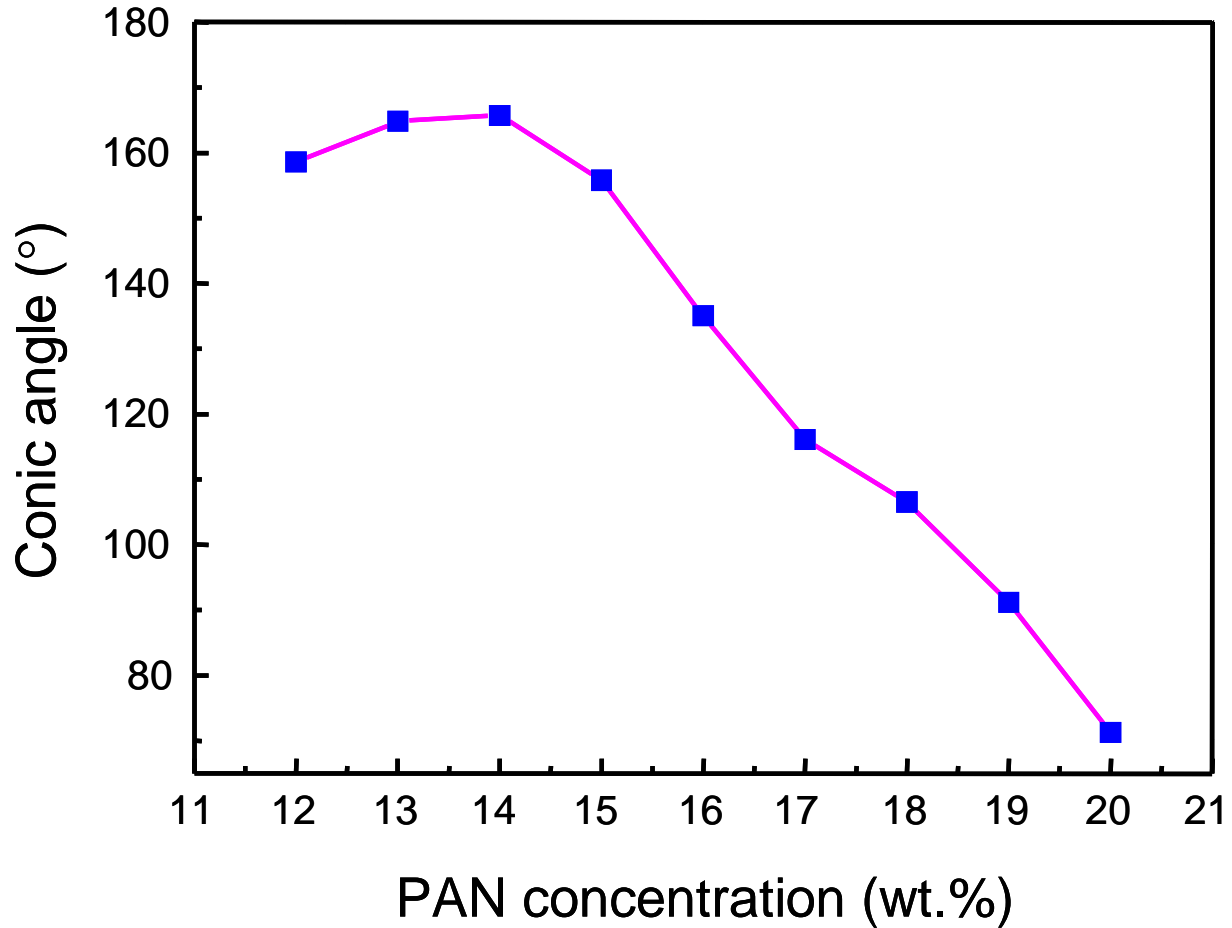
Figure 7.4. Experimental measurements of variation of the conic angle formed by PAN nanofibers with varying PAN concentration (wt. %) at a constant electric field of 80 kV/m (needle diameter: 0.48 mm).

7.2.2.4. *Effect of flow rate on electrospinning conic angle*

Finally, to investigate the effect of flow rate on the conic angle, the electrospinning was performed at the PAN concentration of 16 wt. %, applied electric field of 80 V/m, and needle inner diameter of 0.48 mm (22-gauge needle). Figure 7.5 shows the variation of the conic angle with respect to the flow rate in the range of 0.4 to 1.0 ml/h. The experimental measurements show that the conic angle increases from 95° at the flow rate 0.4 ml/h to 155° at the flow rate 1.0 ml/h. Therefore, the flow rate has a significant effect on the conic angle. Such effect is due mainly to the formation of a varying Taylor's cone in the electrospinning process when the flow rate is changed.

Typically, a large flow rate corresponds to a large droplet at the needle outlet, which alters the jet initiation (e.g., the initial jet diameter, jet velocity, etc.) and finally the conic angle of nanofiber envelope. All the results discussed in this section have been published in *Journal of Physics D: Applied Physics* in 2011 (Zhou et al., 2011).
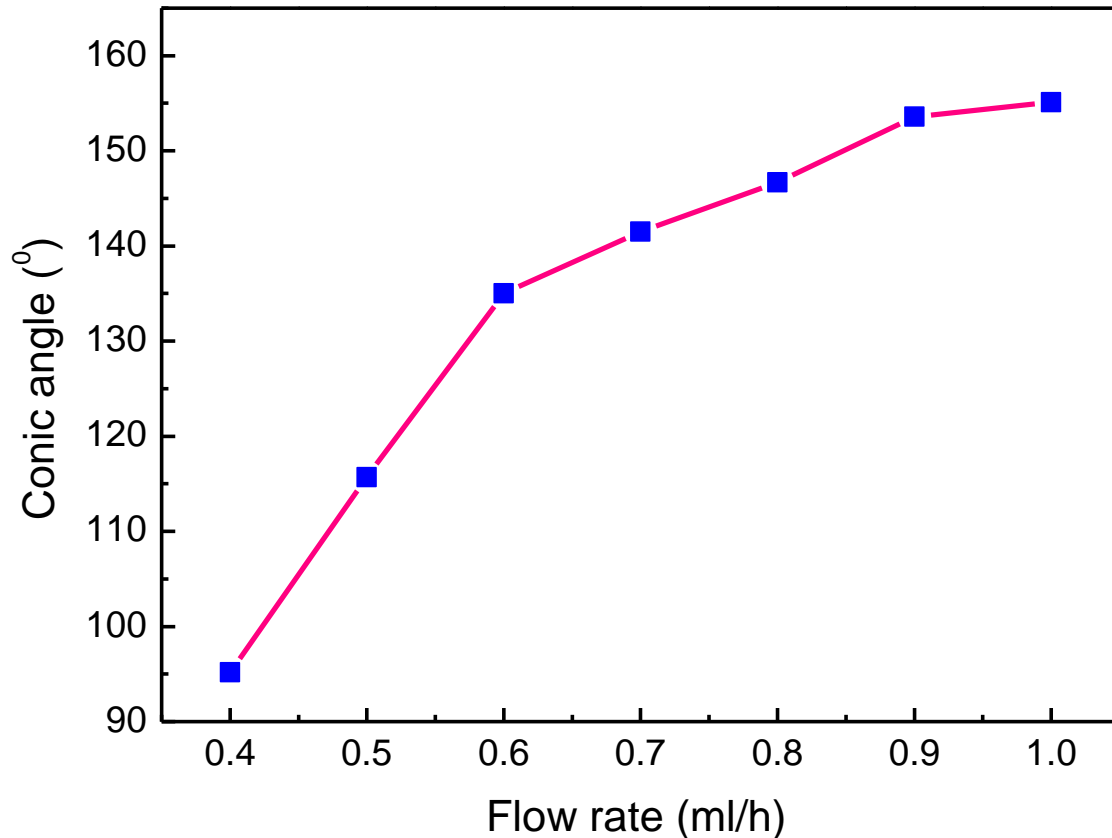
Figure 7.5. Experimental measurements of variation of the conic angle formed by PAN nanofibers with varying flow rate at a constant PAN concentration of 16 wt.% and electric field of 80 kV/m (needle diameter: 0.48 mm).

7.3.   Needleless Emulsion Electrospinning for Scalable Fabrication of Core-Shell Nanofibers

7.3.1.   Experimental

7.3.1.1.   Experimental setup of dual-wire emulsion electrospinning

Figures 7.6 (B) and (C) illustrate the setup of dual-wire emulsion electrospinning, which consists of a dual-wire spinneret (two closely aligned copper wires with a small spacing in this study), a rotary aluminum disk (diameter: 25 cm and thickness: 2.5 mm) as the fiber collector, and two high voltage DC power supplies (Gamma High Voltage Research, Inc., Ormond Beach, FL) installed with the positive and negative voltage outputs, respectively. Use of a DC power supply with a negative voltage output as illustrated in Fig. 7.6 (C) was to ensure that the potential of the fiber collector was always below the potential of grounded surrounding apparatuses such as the equipment and lab utilities and thus to avoid the possible nanofibers flying off the fiber collector during electrospinning process.

As illustrated in Figs. 7.6 (A) and (B), two closely positioned straight copper wires form a capillary microchannel (dual-wire spinneret) that can be utilized to manipulate and deliver a small quantity of liquid via capillary effect or mechanical motion through an emulsion reservoir back and forth (Bedarkar et al., 2010; Guceri et al., 2004; Princen, 1970; Wu et al., 2010). Droplets sitting between the wires can form either barrel-shaped droplets, which completely enwrap the two wires, or droplet-bridges, which partially wet the two wires, depending upon the wetting characteristic curves of the system (Bedarkar et al., 2010; Wu et al., 2010). Superior to droplets sitting on a single wire, when the wire spacing of the dual-wire spinneret is very small, the micro-channel between the two thin wires can generate sufficient capillary force to pump the droplets to move along the wires in the form of droplet-bridge, i.e., wetting the wires or wicking. Recent

124

experimental study (Guceri et al., 2004) indicated that the wicking kinetics of droplet spreading on a dual-wire spinneret roughly obeyed the simple Lucas-Washburn law (Lucas, 1918; Washburn, 1921), i.e., given a wire spacing, the meniscus displacement is proportional to the complete wicking time (i.e., the time interval from the start of droplet spreading to its disappearance). When applying a high DC voltage between the dual-wire spinneret and the fiber collector, the electrostatic force acting on the liquid can destabilize the liquid-bridge and form multiple droplets as illustrated in Fig. 7.6 (B); each droplet may initiate one or multiple jets as illustrated in Fig. 7.6 (C) due to the complex morphology of the droplets. When the two ends of the dual-wire spinneret are connected to an emulsion reservoir or a digitally controlled syringe pump, the capillary force can drive the emulsion to the jetting zone as shown in Fig. 7.6 (C). This pumping process can also be realized via oscillating the dual-wire through the emulsion reservoir (mechanical translation). Thus, scalable continuous emulsion electrospinning can be sustained using the present setup. In addition, use of dual-wire spinneret can significantly suppress fast evaporation of volatile solvent via reducing exposure of the emulsion to open air.
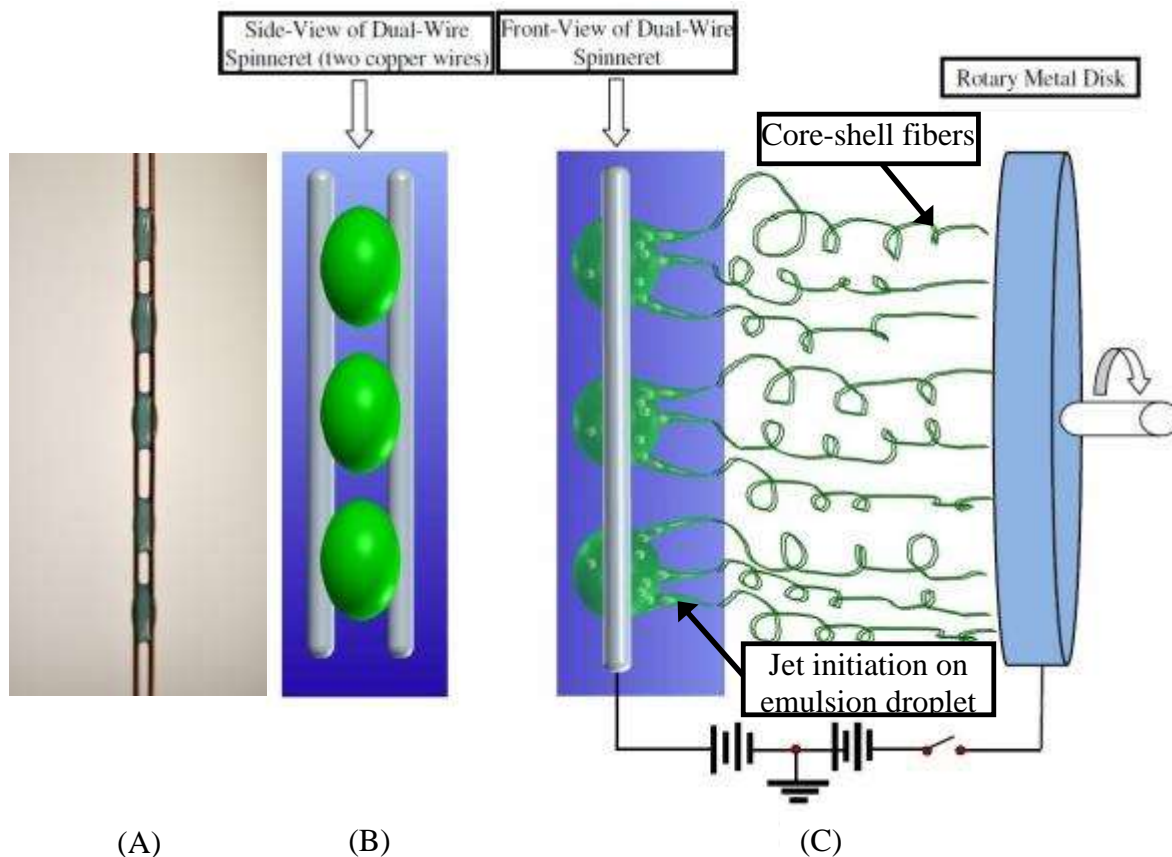
Figure 7.6. (A) Droplets of 10 wt. % PAN/IPDI/DMF emulsion wetting on two closely aligned copper wires (the diameter of the copper wires: 0.78 mm; the volume of the emulsion droplet: ~0.1 ml; a small quantity of dye was dissolved into the emulsion for better visualization). (B) Side view and (C) front view of the schematic setup of dual-wire emulsion electrospinning for scale-up fabrication of ultrathin core-shell fibers. During dual-wire emulsion electrospinning, droplets of the second polymer solution are enwrapped within the master droplets of the first polymer solution; multiple jets ejaculate from the master droplet due to electrohydrodynamic destabilization; enwrapped droplets within the jets are stretched and thinned under electrostatic force and eventually form the core material after drying.

7.3.1.2. *Preparation and characterization of PAN/IPDI/DMF emulsion*

To form the emulsions, two precursor solutions, i.e., the PAN/DMF solutions with the mass concentration of 6%, 8%, 10%, 12%, and 14% PAN and IPDI/DMF solutions with the equal mass concentrations of IPDI, were first prepared separately via dissolving the PAN powder and liquid IPDI in DMF, respectively. Each pair of as-prepared PAN/DMF and IPDI/DMF solutions with the identical mass concentration was continuously stirred on a hot-plate at 75 °C for 4 h, and then

126

blended together at the mass fraction 1:1. The resulting ternary PAM/IPDI/DMF mixture was stirred on a hot-plate at 75 °C for another 4 h and then stirred slowly at room temperature till the electrospinning test. Furthermore, the transient shear viscosity of the PAN/IPDI/DMF solutions was characterized using a TA ARG2 Rheometer (TA Instruments, New Castle, DE) in the range of shear rate from 0 to 1000 s^{-1} at room temperature. In addition, morphologies of as-prepared emulsions were characterized using an optical microscope (IX 71 Olympus with the objective magnification of ×40) as shown in Fig. 7.7, from which it can be observed that well-formed droplets (IPDI/DMF solution) dispersed in PAN/DMF solution.
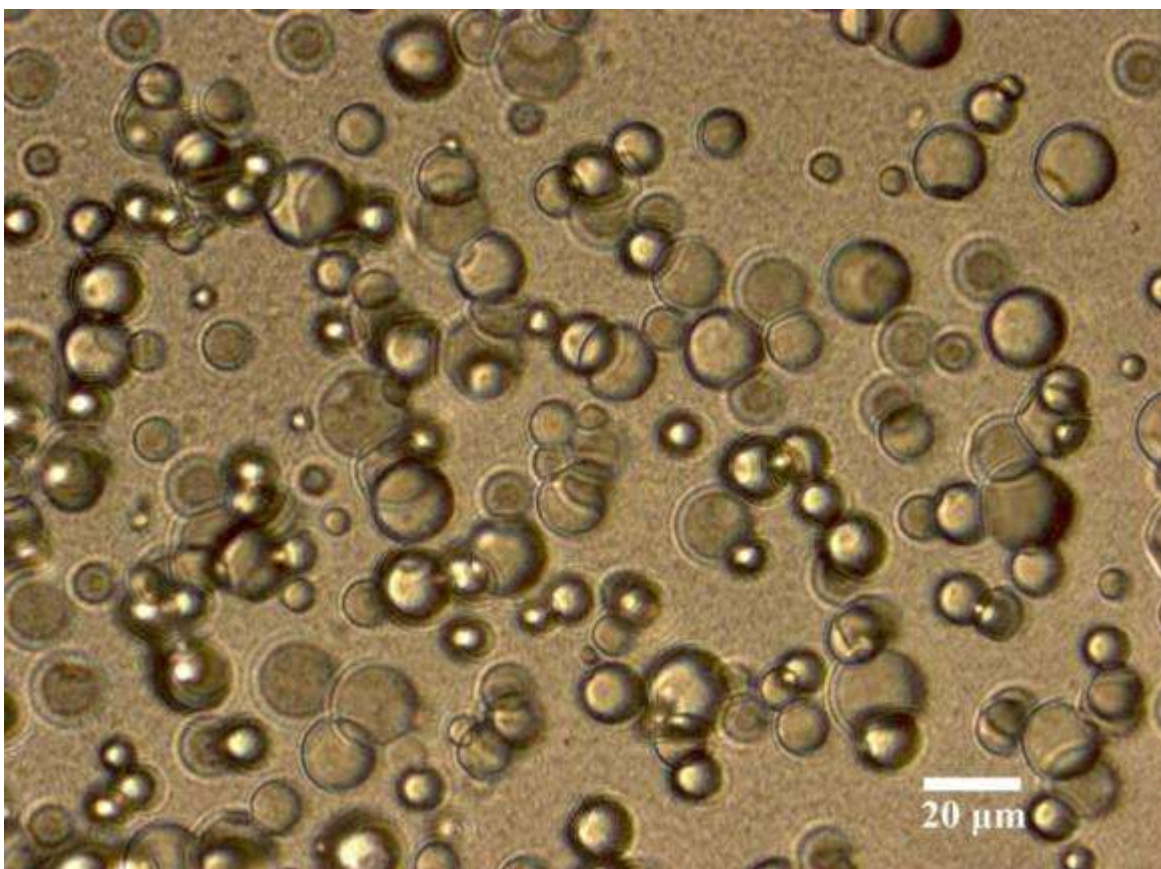
Figure 7.7. Optical micrograph of an IPDI/PAN/DMF emulsion. The emulsion was prepared via blending 10 wt. % PAN/DMF solution with 10 wt. % IPDI/DMF solution and placed in laboratory at room temperature without disturbance for 2 days.

127

7.3.1.3. Needleless emulsion electrospinning for scale-up fabrication of core-shell PAN/IPDI nanofibers

As illustrated in Fig. 7.6 (C), during the electrospinning process, the rotary disk was placed over the dual-wire plane with a vertical distance ~25 cm and powered by a DC electrical motor with adjustable angular velocity. For the purpose of comparative study, in the case of the PAN/DMF and IPDI/DMF solutions with the mass concentration of 10 wt. %, the copper wires with two different diameters (0.28 mm and 0.78 mm) and two different values of spacing (0 and 0.30 mm) were chosen for the dual-wire spinneret. In addition, to investigate the effect of mass concentration of the PAN/IPDI/DMF solution on the diameter of core-shell PAN/IPDI fibers, PAN/IPDI/DMF emulsions with five mass concentrations were used for the needleless emulation electrospinning test (i.e., 6%, 8%, 10%, 12%, and 14%). In each electrospinning test, the diameter and spacing of the two copper wires were fixed as 0.28 and 0.30 mm, respectively.

In the present study, the dual-wire emulsion electrospinning test was performed at room temperature. Prior to the test, the two copper wires of the spinneret were wiped with acetone to clean and maintain constant surface energy. Given a set of parameters (i.e., the wire diameter and spacing) of the dual-wire spinneret, the emulsion was first delivered to the spinneret manually to form multiple droplet-bridges as shown in Fig. 7.6 (A). Once the spinneret potential was increased up to +25 kV and the fiber collector potential was decreased down to -20 kV, jets started to initiate from the droplet bridges as illustrated in Fig. 7.6 (C). Figure 7.8 shows the snapshots of a typical jetting process of an emulsion droplet sitting on the dual-wire spinneret, where the DC voltage between the dual-wire spinneret and fiber collector was gradually increased. The electrospinning process can be maintained with continuous supply of emulsion via electrocapillary pumping or mechanical translation of the emulsion. The morphology of the electrospinnable emulsion and the

core-shell structure of the resulting ultrathin PAN/IPDI fibers were characterized by means of optical microscopy (IX 71 Olympus with the objective magnification of ×40), SEM, and FT-IR spectroscopy characterizations.
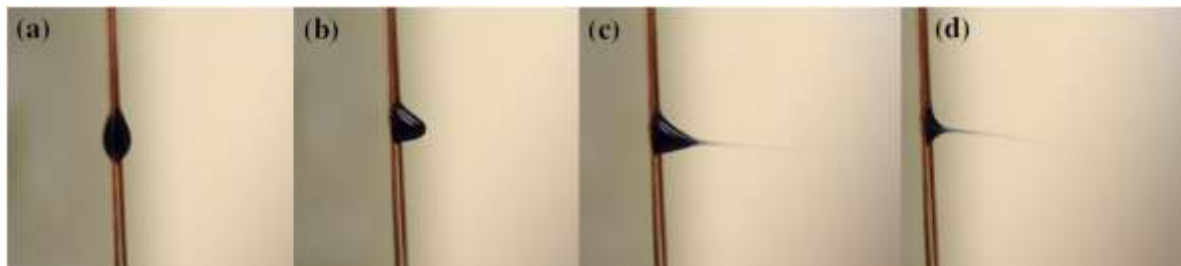
Figure 7.8. Snapshots of dual-wire emulsion electrospinning process with gradually increasing DC voltage of the wires (a) 0 kV; (b) ~10 kV; (c) & (d) ~15 kV. (The diameter of the copper wires: 0.78 mm; the volume of the droplet: ~0.1 ml; the distance between the dual-wire spinneret and the fiber collector: 20 cm; the emulsion was prepared via blending 10 wt. % PAN/DMF solution with 10 wt. % IPDI/DMF solution; a small quantity of dye was dissolved in the solution for better visualization).

7.3.2. Results and discussions

7.3.2.1. *Optical micrographs of core-shell PAN/IPDI fibers*

The optical micrographs as shown in Fig. 7.9 are the typical ultrathin core-shell PAN/IPDI fibers produced by using the present emulsion electrospinning method based on the PAN/IPDI/DMF emulsion with the PAN/IPDI mass concentration 10 wt. % at varying process parameters as follows. To produce the PAN/IPDI fibers as shown in Figs. 7.9 (A) and (B), the dual-wire spinneret consisted of two identical copper wires of the diameter 0.28 mm and wire spacing 0.30 mm. It can be observed from Figs. 7.9 (A) and (B) that the core-shell nanostructures were well formed with uniform morphologies of the interior liquid IPDI core and exterior solid PAN shell.
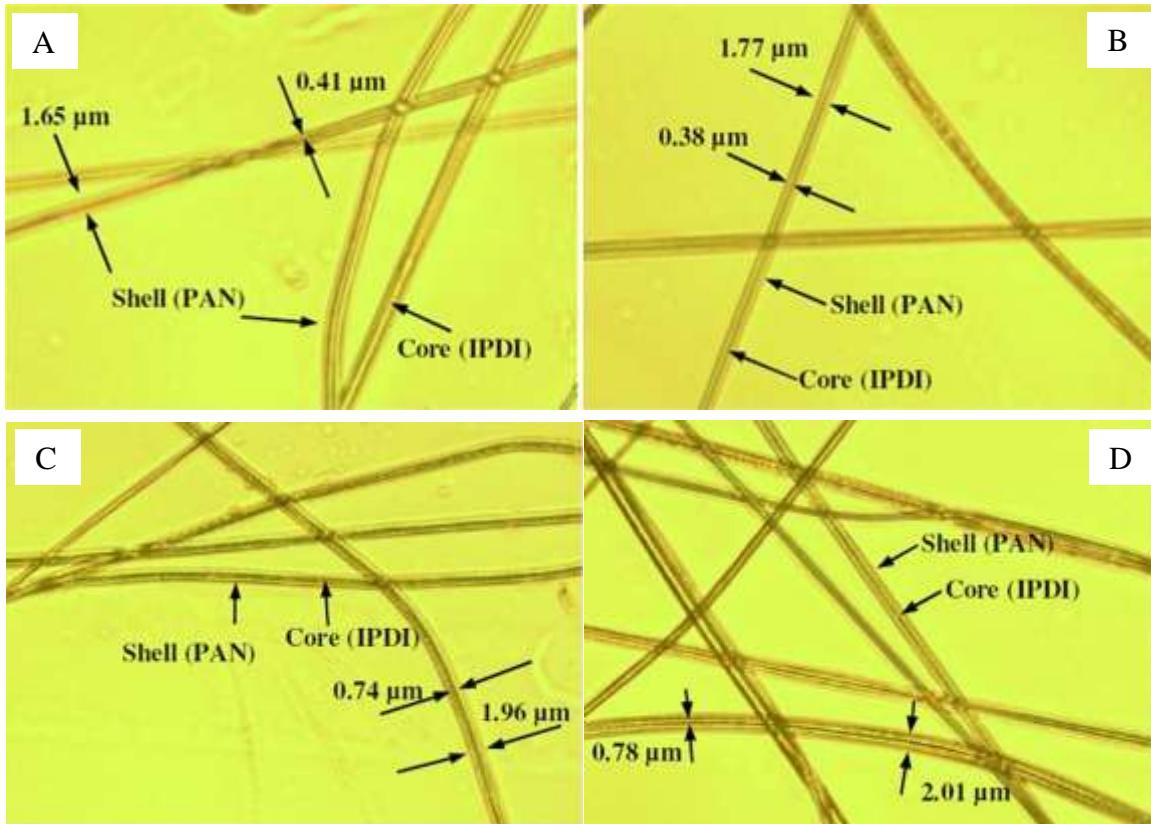
Figure 7.9. Optical micrograph of emulsion-electrospun core-shell PAN/IPDI fibers based on a dual-wire spinneret: (A, B) The diameter of copper wires was 0.28 mm and wire spacing was 0.30 mm; (C) the diameter of copper wires was 0.28 mm and there was free wire spacing; (D) the diameter of copper wires was 0.78 mm and wire spacing was 0.30 mm.

7.3.2.2.   *Effect of wire spacing on the morphology of the core-shell PAN/IPDI fibers*

To examine the effect of wire spacing on the morphology of core-shell PAN/IPDI fibers, a dual-wire spinneret with zero spacing was further utilized, whereas the rest process parameters were unaltered. Figure 7.9 (C) shows the typical optical micrograph of the resulting core-shell PAN/IPDI fibers. It can be observed that though the core-shell PAN/IPDI fibers were well formed with smooth morphologies of the interior core and exterior shell, the diameter of the core-shell fibers showed a large variation. Multiple measurements showed that the average diameter of the IPDI core is ~0.7 µm, whereas the average exterior diameter of the PAN shell is ~1.9 µm, which

are much larger than those with the wire spacing of 0.30 mm. In this case, relatively large droplets can assume on the dual-wire spinneret, which ultimately developed into Taylor cones with a large size, corresponding to the large diameter of the final core-shell nanofibers though detailed electrohydrodynamic mechanisms are still not available yet.

7.3.2.3. *Effect of the wire diameter on the diameter and morphology of the core-shell PAN/IPDI fibers*

To take into account the effect of wire diameter on the diameter and morphology of the final core-shell PAN/IPDI fibers, a dual-wire spinneret with the wire diameter 0.78 mm and wire spacing 0.30 mm was used, and the rest process parameters were still maintained the same. Figure 7.9 (D) shows the typical optical micrograph of the resulting core-shell PAN/IPDI fibers. From Fig. 7.9 (D), it can be found that the core-shell PAN/IPDI fibers still carried well-formed morphologies of the interior core and exterior shell. However, the diameter of the core-shell fibers had a much larger variation than those in the two cases investigated above. In this case, the average diameters of the IPDI core and PAN shell are ~0.8 and ~2.0 μm, respectively, slightly larger than those based on the dual-wire spinneret with zero spacing. In this case, after electrohydrodynamic destabilization, droplets with a larger size assumed on the dual-wire spinneret, which finally resulted in the core-shell PAN/IPDI nanofibers with larger diameters. As a result, the wire diameter and spacing of the dual-wire spinneret combined with other process and material parameters can be used for tuning the geometry of electrospun core-shell fibers.

The structure of the present core-shell PAN/IPDI nanofibers was also examined by means of SEM. During the process, as-prepared core-shell PAN/IPDI nanofibers made from 10 wt. % PAN/IPDI/DMF emulsion were consolidated into an epoxy resin. After curing in room

temperature, five pieces of sample slides were prepared using a sharp razor, coated with carbon, and SEM-scanned. Figure 7.10 (A) shows the cross-section of a scissored core-shell PAN/IPDI nanofiber embedded in epoxy resin, where the core–shell structure can be clearly detected, and the liquid IPDI dissipated due to polymerization triggered by the air. Figure 7.10 (B) shows the side view of a cracked core-shell PAN/IPDI nanofiber, from which the cracked shell material can be obviously detected and the liquid IPDI solidified into newborn porous structure after polymerization.
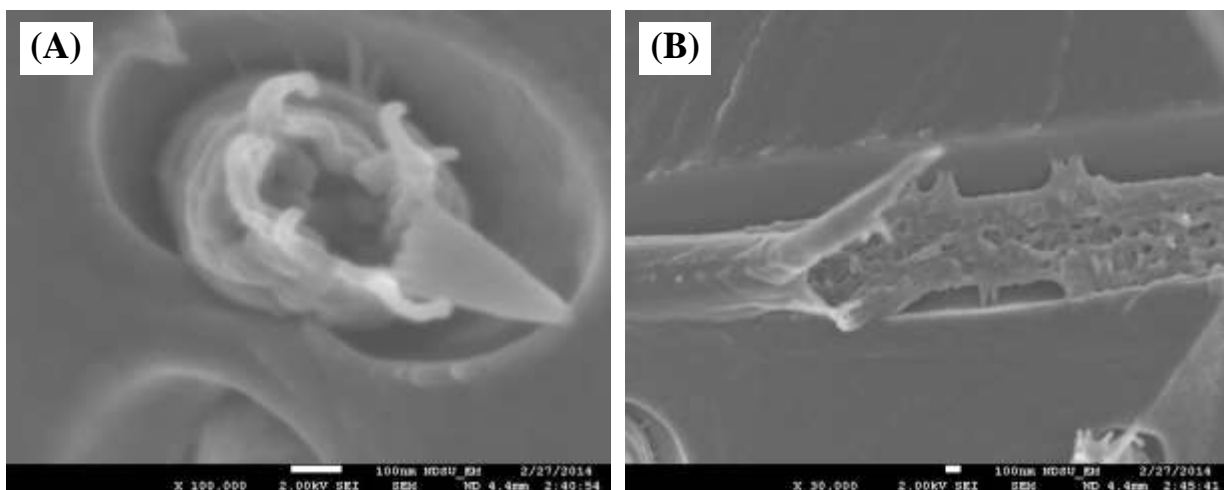
Figure 7.10. SEM micrographs of (A) cross-section of a scissored core-shell PAN/IPDI nanofiber and (B) side view of a cracked core-shell PAN/IPDI embedded in epoxy resin.

7.3.2.4.　　　*FT-IR characterization of the core-shell PAN/IPDI fibers*

In addition, FT-IR was further utilized to validate the chemical composition of the PAN/IPDI nanofibers. Figure 7.11 shows the comparative FT-IR spectra of the pure PAN nanofibers produced by single-needle based electrospinning and the present core-shell PAN/IPDI fibers. The FT-IR results confirm the existence of IPDI in the core-shell fibers. In the spectra of PAN nanofibers, the characteristic absorption bands at 2,920 cm^{-1}, 2,238 cm^{-1}, 1,662 cm^{-1} and 1,449 cm^{-1} are, respectively, assigned to νC-H stretching, νC≡N stretching, δC-H bond bending

and δCH₂ asymmetric vibration (Moreno et al., 2010). In contrast, in the spectra of PAN/IPDI fibers, two obvious peaks at ~2,245 cm^{-1} and ~2,920 cm^{-1} exist due to the isocyanate νN=C=O and νC-H stretching vibrations in IPDI, respectively (Zhou et al., 2010). Besides, bands at 1,627 cm^{-1} and 1,563 cm^{-1} due to C=O vibration in the –NCO group are in a good agreement with the existence of IPDI in the PAN/IPDI core-shell nanofibers. These characteristic infrared spectra combined with the layered structure observed by means of optical microscopy above confirmed the core-shell structure of the obtained PAN/IPDI fibers.
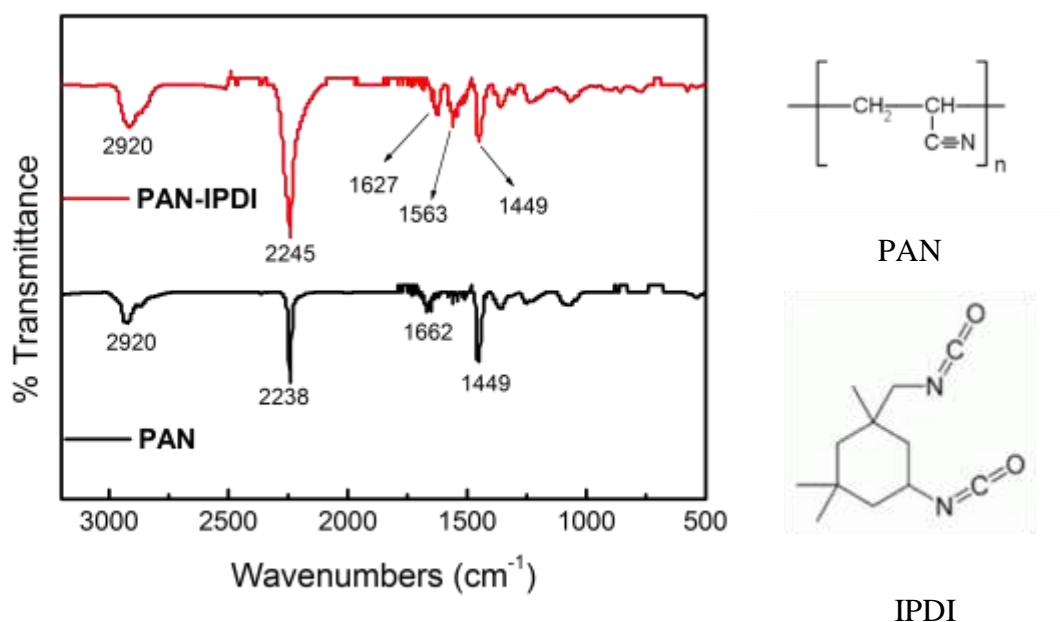
Figure 7.11. FT-IR spectra of both pure PAN nanofibers and typical emulsion-electrospun core-shell PAN/IPDI nanofibers.

7.3.2.5. *Effect of the PAN/IPDI mass concentration on the diameter of core-shell PAN/IPDI fibers*

To examine the effect of PAN/IPDI mass concentration on the diameter of the resulting core-shell nanofibers, five PAN/IPDI/DMF emulsions with the PAN/IPDI mass concentration of

6%, 8%, 10%, 12%, and 14% (mass fraction PAN : IPDI = 1 : 1) were prepared and tested as aforementioned. Figure 7.12 shows the transient viscosity of the five emulsions tested on a TA ARG2 Rheometer (TA Instruments, New Castle, DE). It can be found from Fig. 7.12 that given a shear rate, the transient viscosity increases with increasing mass concentration. Furthermore, in the case of the PAN/IPDI mass concentration of 6% and 8%, the viscosity of the PAN/IPDI/DMF emulsion appears nearly constant in the range of testing shear rate from 0 to 1,000 s^{-1}. However, in the case of PAN/IPDI mass concentration of 10%, 12%, and 14%, the viscosity decreases noticeably at the high shear rate. Such a shear-thinning effect is typically observed in polymer solutions at high shear rates due to delayed chain relaxation (Barnes and Roberts, 1992; Zhou et al., 2011).
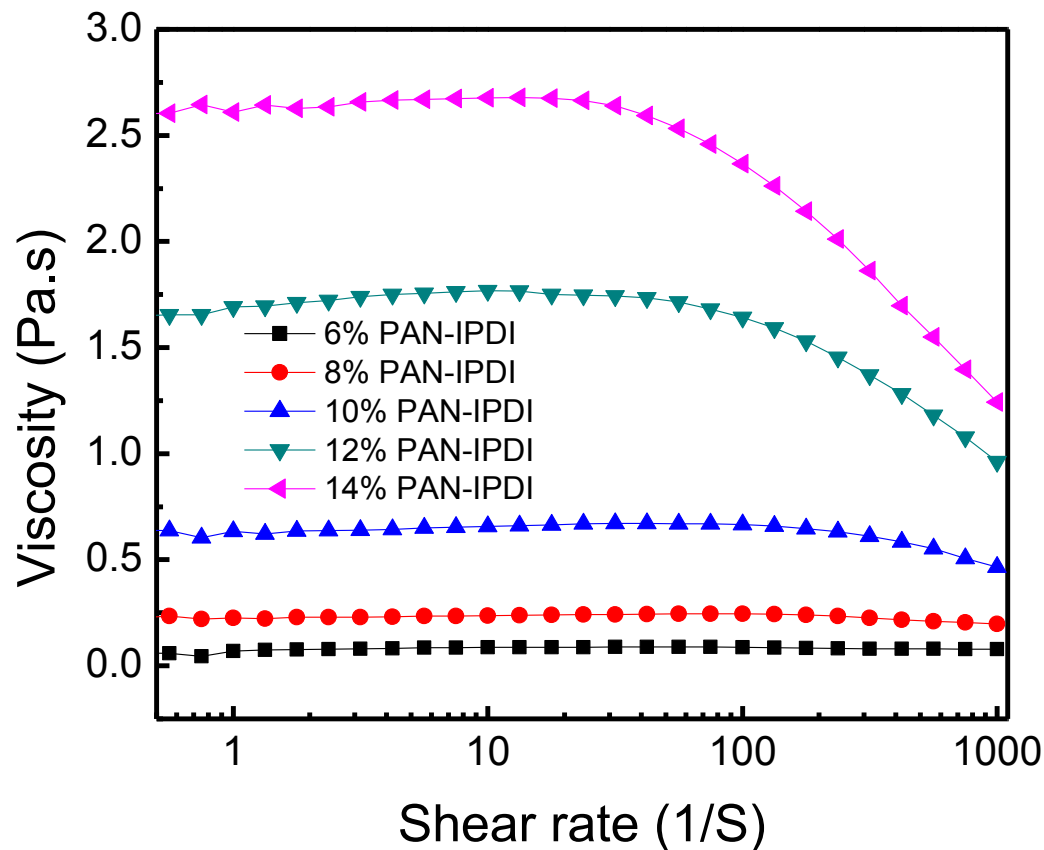
Figure 7.12. Variation of the shear viscosity with varying shear rate for PAN/IPDI (mass ratio=1:1)/DMF solutions at varying PAN/IPDI mass concentrations of 6%, 8%, 10%, 12%, and 14%.

The variation of the exterior diameter of the core-shell PAN/IPDI with varying PAN/IPDI mass concentration is tabulated in Table 7.3 and shown in Fig. 7.13. It can be found that the average fiber diameter increases rapidly with increasing PAN/IPDI concentration from 144 nm at 6 wt. % to 3,426 nm at 14 wt. %. Correspondingly, the deviation of the fiber diameter also increases rapidly with increasing PAN/IPDI concentration. These average and deviation values of fiber diameter were obtained by performing ~100 measurements from ~20 to 30 SEM micrographs of the typical core-shell PAN/IPDI fibers.

Table 7.3. Average exterior diameters of the PAN/IPDI nanofibers produced by means of needleless emulsion electrospinning at varying solution mass concentrations.

Solution concentration (wt. %) (PAN:IPDI=1:1 by weight)	6	8	10	12	14
Exterior diameter of nanofiber (nm)	144 ± 50	314 ± 55	710 ± 180	1630 ± 640	3430 ± 1450
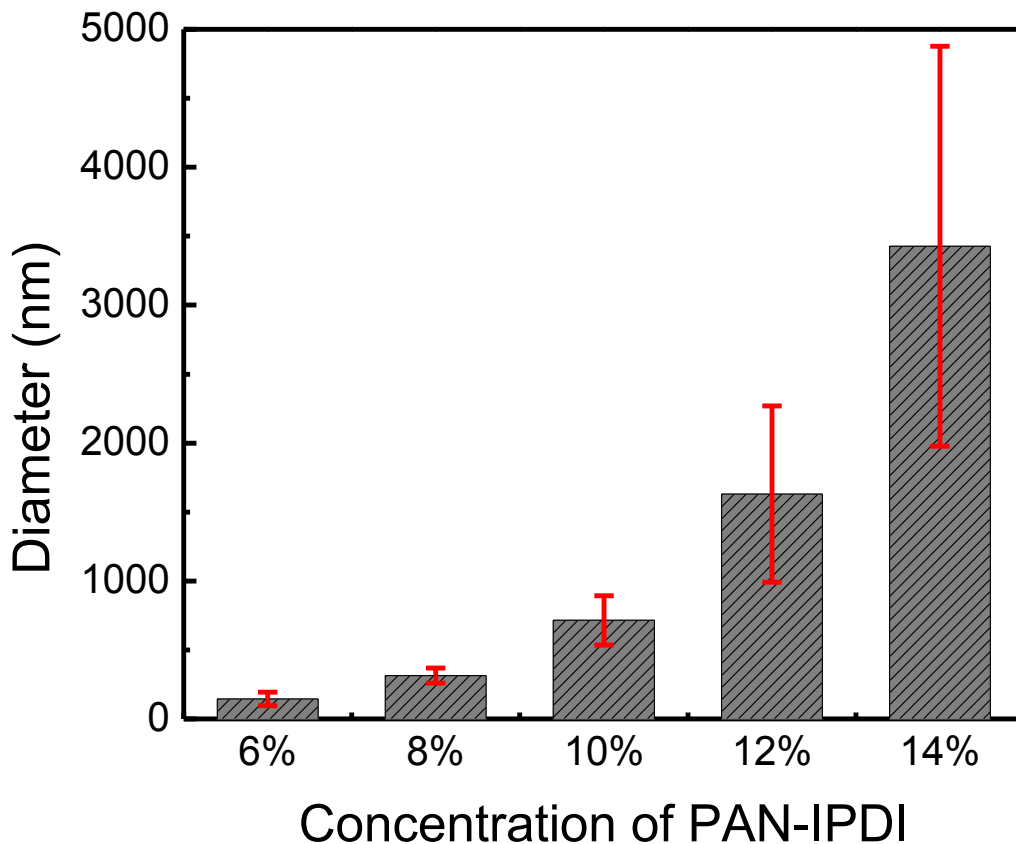
Figure 7.13. Variation of the exterior diameter of emulsion-electrospun core-shell PAN/IPDI fibers with varying mass concentration of PAN and IPDI (copper wire diameter: 0.28 mm and wire spacing: 0.30 mm).

Figure 7.14 shows the SEM micrographs of typical PAN/IPDI nanofibers produced at varying PAN/IPDI mass concentrations. It can be detected that the diameter variation of these ultrathin PAN/IPDI fibers becomes larger and larger with increasing PAN/IPDI mass

concentration. Thus, it can be concluded that to produce core-shell fibers with uniform diameter, relatively low mass concentration is preferred in needleless emulsion electrospinning.

It is worthy to point out that these ultrathin core-shell PAN/IPDI fibers are technologically important to self-repairing PMCs (Sinha- Ray et al., 2012; Wu et al., 2013; Wu and Yarin, 2013). The core-shell PAN/IPDI fibers can be embedded at the interfaces of fiber-reinforced PMCs via depositing them onto the prepreg sheets before thermal press molding or onto the fiber fabrics before resin infusion. After curing, the core-shell PAN/IPDI nanofibers will form ultrathin self-repairing interlayers with rich PAN/IPDI nanofibers. Upon occurrence of interfacial damage such as delamination that scissors the PAN/IPDI nanofibers, the liquid healing-agent IPDI will autonomically release at the locus of damage under the action of capillary forces and local stresses and polymerize upon catalysis with the aid of local and environmental water or moisture (Sinha-Ray et al., 2012; Wu et al., 2013; Wu and Yarin, 2013).

Moreover, the present experimental study also opens an innovative route in electrospinning and nanomanufacturing for scale-up continuous fabrication of core-shell nanofibers because multiple core-shell jets can form simultaneously from the dual-wire spinneret. Also, the experimental observations available in this study can provide valuable first-hand experimental data to advance understanding and exploitation of the fundamental electrohydrodynamic theories for intelligent mass production of core-shell nanofibers. All the results in this section have been published in *Journal of Applied Polymer Science* in 2014 (Zhou et al., 2014).
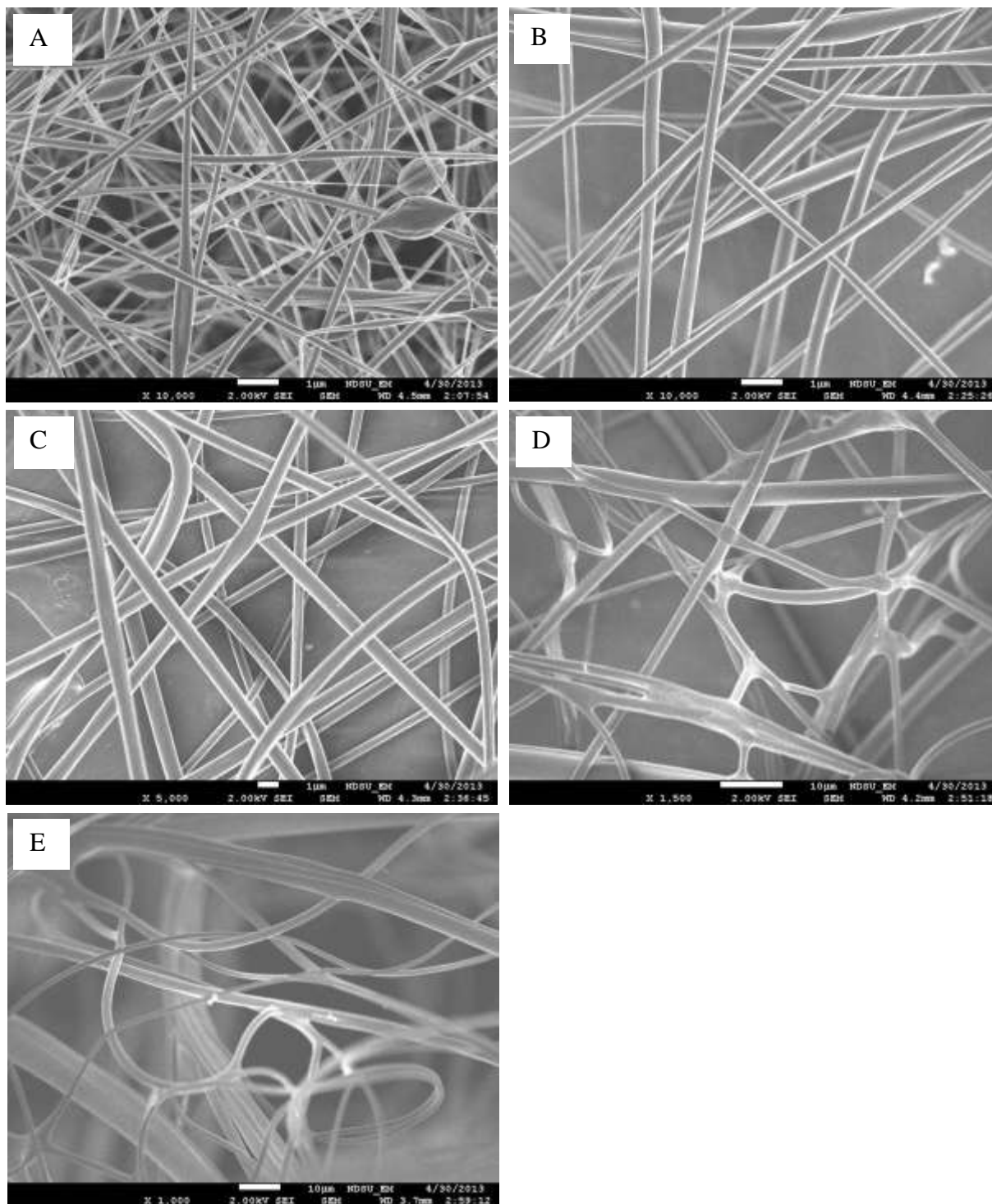
Figure 7.14. SEM micrographs of typical emulsion-electrospun core-shell PAN/IPDI fibers with varying mass concentration of PAN/IPDI: A) 6 %, B) 8 %, C) 10 %, D) 12 %, and E) 14 % by weight concentration in DMF (copper wire diameter: 0.28 mm and wire spacing: 0.30 mm).

7.4. Summary

In the first section of this chapter, a detailed experimental investigation has been carried out to explore the dependency of conic angle of nanofiber envelope upon the polymer concentration, applied DC voltage, flow rate, and needle inner diameter employed in electrospinning. The experimental results provide an insight of the fundamental electrohydrodynamic phenomenon in the electrospinning process, which can facilitate the research on controllable fabrication of electrospun nanofibers for numerous applications as well as relevant process modeling.

In the second section, a novel dual-wire emulsion electrospinning method has been developed and demonstrated for successful scalable continuous fabrication of core-shell nanofibers with well layered structures. Effects of several process and material parameters on the fiber diameter have been examined. The experimental results indicated that the average fiber diameter increases with increasing either wire diameter or mass concentration, or decreasing wire spacing of the dual-wire spinneret. The present experimental study also provides useful first-hand data to explore the fundamental understanding of modern electrospinning processes. The needleless dual-wire emulsion electrospinning technique can be exploited for low-cost mass production of core-shell nanofibers for large-scale applications in broad areas.

CHAPTER 8. CONCLUSIONS AND FUTURE STUDIES

In this dissertation, two rational synthesis routes have been successfully formulated for fabrication of four types of advanced hierarchical nanofibrous electrode materials (i.e., CNFs surface-grown with CNTs, CNT-grown CNFs coated with PANI, graphene-beaded CNFs, and graphene-beaded CNFs coated with PANI) for use as electrode materials in electrochemical supercapacitors. The main goal of the research was to introduce the favorable pseudocapacitive effect and simultaneously suppress the high contact electrical resistance of discretely stacked nanomaterials (e.g., CNTs, graphene nanosheets, etc.) used in existing electrodes of supercapacitors.

During the study, the continuous porous CNFs as template were synthesized via stabilization, carbonization of as-electrospun PAN/Ni(AcAc)$_2$ nanofibers; the hierarchically structured CNFs surface-grown with CNTs (CNT/CNFs) were fabricated in sequence by growing brush-like CNTs onto the surface of electrospun CNFs via controlled CVD. These hierarchically structured CNT/CNF films were further used as porous scaffolds to function as active sites for *in situ* polymerization of aniline to form ternary core-shell nanofibrous PANI/CNT/CNF films, which can be used as an innovative multifunctional electrode material with high specific surface area and strong pseudocapacitive effect. Such unique hierarchal structure guarantees the high electrochemical performance of the resulting supercapacitors with noticeably enhanced energy and power densities. Meanwhile, the CNT/CNF networks were functioned as the excellent current-delivery channels to suppress the electrical contact resistance of the electrodes due to their high electrical conductivity and excellent topological connectivity.

Furthermore, graphene-beaded CNFs (G/CNFs) were successfully produced via electrospinning PAN/DMF solution dispersed with oxidized graphene nanosheets, followed by controlled carbonization. These hierarchically structured G/CNFs were further surface-functionized via coating thorn-like PANI nanorods to form ternary porous PANI-G/CNFs.

Detailed microstructural and electrochemical characterizations have been performed successfully by means of SEM, TEM, Raman spectrometry, EIS, FTIR, etc. The electrochemical performances of the four innovative porous nanofibrous electrode materials synthesized in this study are tabulated in Table 8.1.

Table 8.1. Electrochemical performances of the hierarchically structured CNT/CNFs, PAN/CNT/CNFs, G/CNFs, and PANI/G/CNFs synthesized in this study.

Electrode Materials	Specific Capacitance	Electrolytes	Voltage Window	Discharge Current Density
CNT/CNFs	185 F/g	PVA/H_3PO_4 (10 wt. %)	0-0.8 V	625 mA/g
PAN/CNT/CNFs	503 F/g	1 M H_2SO_4	-0.2-0.8 V	300 mA/g
G/CNFs	226.2 F/g	6 M KOH	0-0.8 V	500 mA/g
PANI/G/CNFs	591 F/g	1 M H_2SO_4	-0.2-0.8 V	300 mA/g

From Table 8.1, it can be found that the innovative hierarchically structured CNT/CNFs and G/CNFs can noticeably enhance their electrochemical performance compared to electrospun CNFs by increasing their specific surface area. The values of specific capacitance of CNT/CNFs and G/CNFs as electrode materials of supercapacitor are 185 F/g at discharge current 625 mA/g and 226.2F/g at discharge current 500 mA/g against electrospun CNFs with the value of specific capacitance as 114.6F/g at discharge current 500 mA/g. In addition, by introducing the unique

synergetic pseudocapacitive effect to CNT/CNFs and G/CNFs via deposition of nanostructured PANI, the values of specific pseudocapacitance of the resulting PANI/CNT/CNFs and PANI/G/CNFs are 503 F/g and 591 F/g at discharge current of 300 mA/g, respectively. Also, these advanced nanofibrous electrode materials exhibited very good cyclability.

Thus, this study has provided a family of unique low-cost, multifunctional nanofibrous electrode materials with high specific capacitance, cyclability, and related high power and energy densities for potential use in high-performance electrochemical energy storage devices. The successful formulation of the related rational synthesis routes leads to a systematical manufacturing method for parameter study, optimization, and low-cost, scale-up, controllable fabrication.

In addition, the present study of parameter study of conic angle of electrospinning provided the first-hand experimental data for understanding the fundamental principle of electrohydrodynamics of needle-based electrospinning and controllable electrospinning. Furthermore, development of needleless emulsion electrospinning in this study also offered a low-cost nanofabrication method for continuous, scalable production of core-shell nanofibers. This method makes it possible to large-scale use of core-shell nanofibers for toughening and damage self-healing of polymer composites, biomedical applications, etc.

The present research also opens up several potential investigations in this field in the future as follows:

1. Optimization of the material and process parameters to maximize the electrochemical performance of hierarchally structured nanofibrous electrode materials such as control of the length of grown CNTs, type and size of graphene nanosheets, type of electrolyte, etc.

142

2. Synthesis of other types of ternary core-shell nanofibrous electrode materials via coating other types of conducting polymers (e.g., PPy, PEDOT, etc.) and transition metal oxides (e.g., RuO_2, MnO_2, NiO, etc.) onto the surface of CNT/CNFs and G/CNFs.

3. Fabrication and electrochemical performance characterization and modeling of supercapacitor devices based on the novel nanofibrous electrode materials synthesized in the present research.

4. Exploration of the fundamental growth mechanisms of CNTs and conducting polymers onto CNF surfaces and related growth characterization and modeling.

5. Scalable fabrication of core-shell nanofibers of a variety of polymer (material) pairs via needleless emulsion electrospinning and exploration of their novel applications in toughening and damage self-healing of polymer matrix composites, drug delivery, etc.

6. Establishment of novel models to simulate the conic angle of electrospinning and examine the parameter dependency for controllable nanofiber fabrication.

7. Establishment of novel models to simulate the entire process of needleless electrospinning and needleless emulsion electrospinning (i.e., multiple jet initiation, elongation, drying, etc.) and examine their parameter dependency for controllable nanofiber fabrication.

REFERENCES

Key World Energy Statistics In *International Energy Agency*, 2010; p 82.

An, K. H.; Kim, W. S.; Park, Y. S.; Moon, J. M.; Bae, D. J.; Lim, S. C.; Lee, Y. S.; Lee, Y. H., Electrochemical properties of high-power supercapacitors using single-walled carbon nanotube electrodes. *Advanced Functional Materials* **2001,** *11* (5), 387.

Andrady, A. L., Science and Technology of Polymer Nanofibers, John Wiley & Sons, Inc. **2008**; p 404.

Arico, A. S.; Bruce, P.; Scrosati, B.; Tarascon, J. M.; Van Schalkwijk, W., Nanostructured materials for advanced energy conversion and storage devices. *Nature materials* **2005,** *4* (5), 366.

Arunachalam, V. S.; Fleischer, E. L., The global energy landscape and materials innovation. *MRS Bullutin* **2008,** *33* (04), 264.

Balandin, A. A.; Ghosh, S.; Bao, W.; Calizo, I.; Teweldebrhan, D.; Miao, F.; Lau, C. N., Superior thermal conductivity of single-layer graphene. *Nano Letters* **2008,** *8* (3), 902.

Balaya, P., Size effects and nanostructured materials for energy applications. *Energy & Environmental Science* **2008,** *1* (6), 645.

Barhate, R. S.; Ramakrishna, S., Nanofibrous filtering media: Filtration problems and solutions from tiny materials. *Journal of Membrane Science* **2007,** *296* (1–2), 1.

Barnes, C. P.; Sell, S. A.; Boland, E. D.; Simpson, D. G.; Bowlin, G. L., Nanofiber technology: Designing the next generation of tissue engineering scaffolds. *Advanced Drug Delivery Reviews* **2007,** *59* (14), 1413.

Barnes, H. A.; Roberts, G. P., A simple empirical model describing the steady-state shear and extensional viscosities of polymer melts. *Journal of Non-Newtonian Fluid Mechanics* **1992,** *44*, 113.

Barranco, V.; Lillo-Rodenas, M. A.; Linares-Solano, A.; Oya, A.; Pico, F.; Ibañez, J.; Agullo-Rueda, F.; Amarilla, J. M.; Rojo, J. M., Amorphous carbon nanofibers and their activated carbon nanofibers as supercapacitor electrodes. *The Journal of Physical Chemistry C* **2010,** *114* (22), 10302.

Basnayaka, P. A.; Ram, M. K.; Stefanakos, E. K.; Kumar, A., Supercapacitors based on graphene–polyaniline derivative nanocomposite electrode materials. *Electrochimica Acta* **2013,** *92*, 376.

Bazilevsky, A. V.; Yarin, A. L.; Megaridis, C. M., Co-electrospinning of core−shell fibers using a single-nozzle technique. *Langmuir* **2007,** *23* (5), 2311.

Becker, H. I., Low voltage electrolytic capacitor. US Patent: 2800616 A, 1957.

Bedarkar, A.; Wu, X.-F.; Vaynberg, A., Wetting of liquid droplets on two parallel filaments. *Applied Surface Science* **2010,** *256* (23), 7260.

Benson, S. M.; Orr, F. M., Sustainability and energy conversions. *MRS Bullutin* **2008,** *33* (4), 297.

Bird, R. B.; Armstrong, R. C.; Hassager, O., *Dynamics of Polymeric Liquids, Volume 1, Fluid Mechanics*. 2nd ed.; John Wiley & Sons: New York, 1987.

Biswas, S.; Drzal, L. T., Multilayered nano-architecture of variable sized graphene nanosheets for enhanced supercapacitor electrode performance. *ACS Applied Materials & Interfaces* **2010,** *2* (8), 2293.

Biswas, S.; Drzal, L. T., Multilayered nanoarchitecture of graphene nanosheets and polypyrrole nanowires for high performance supercapacitor electrodes. *Chemistry of Materials* **2010,** *22* (20), 5667.

Brennan, L.; Owende, P., Biofuels from microalgae—A review of technologies for production, processing, and extractions of biofuels and co-products. *Renewable and Sustainable Energy Reviews* **2010,** *14* (2), 557.

Brownson, D. A. C.; Kampouris, D. K.; Banks, C. E., An overview of graphene in energy production and storage applications. *Journal of Power Sources* **2011,** *196* (11), 4873.

Bruce, P. G.; Scrosati, B.; Tarascon, J. M., Nanomaterials for rechargeable lithium batteries. *Angewandte Chemie* **2008,** *47* (16), 2930.

Burger, C.; Hsiao, B. S.; Chu, B., Nanofibrous materials and their applications. *Annual Review of Materials Research* **2006,** *36* (1), 333.

Burke, A., Ultracapacitors: why, how, and where is the technology. *Journal of Power Sources* **2000,** *91* (1), 37.

Castro Neto, A. H.; Guinea, F.; Peres, N. M. R.; Novoselov, K. S.; Geim, A. K., The electronic properties of graphene. *Reviews of Modern Physics* **2009,** *81* (1), 109.

Chen, F.; Peng, X.; Li, T.; Chen, S.; Wu, X.-F.; Reneker, D. H.; Hou, H., Mechanical characterization of single high-strength electrospun polyimide nanofibres. *Journal of Physics D: Applied Physics* **2008,** *41* (2), 025308.

Chen, L.; Hong, S.; Zhou, X.; Zhou, Z.; Hou, H., Novel Pd-carrying composite carbon nanofibers based on polyacrylonitrile as a catalyst for Sonogashira coupling reaction. *Catalysis Communications* **2008,** *9* (13), 2221.

Chen, Q.; Zhang, L.; Rahman, A.; Zhou, Z.; Wu, X.-F.; Fong, H., Hybrid multi-scale epoxy composite made of conventional carbon fiber fabrics with interlaminar regions containing electrospun carbon nanofiber mats. *Composites Part A: Applied Science and Manufacturing* **2011**, *42* (12), 2036.

Chen, Q.; Zhang, L.; Yoon, M.-K.; Wu, X.-F.; Arefin, R. H.; Fong, H., Preparation and evaluation of nano-epoxy composite resins containing electrospun glass nanofibers. *Journal of Applied Polymer Science* **2012,** *124* (1), 444.

Chen, Q.; Zhang, L.; Zhao, Y.; Wu, X.-F.; Fong, H., Hybrid multi-scale composites developed from glass microfiber fabrics and nano-epoxy resins containing electrospun glass nanofibers. *Composites Part B: Engineering* **2012,** *43* (2), 309.

Chen, Q.; Zhao, Y.; Zhou, Z.; Rahman, A.; Wu, X.-F.; Wu, W.; Xu, T.; Fong, H., Fabrication and mechanical properties of hybrid multi-scale epoxy composites reinforced with conventional carbon fiber fabrics surface-attached with electrospun carbon nanofiber mats. *Composites Part B: Engineering* **2013,** *44* (1), 1.

Chen, S.; Zhu, J.; Wu, X.; Han, Q.; Wang, X., Graphene oxide−MnO_2 nanocomposites for supercapacitors. *ACS Nano* **2010,** *4* (5), 2822.

Chen, W.; Rakhi, R. B.; Alshareef, H. N., Facile synthesis of polyaniline nanotubes using reactive oxide templates for high energy density pseudocapacitors. *Journal of Materials Chemistry A* **2013,** *1* (10), 3315.

Chen, Z.; Wen, J.; Yan, C.; Rice, L.; Sohn, H.; Shen, M.; Cai, M.; Dunn, B.; Lu, Y., High-performance supercapacitors based on hierarchically porous graphite particles. *Advanced Energy Materials* **2011,** *1* (4), 551.

Cheng, C.; Chen, J.; Chen, F.; Hu, P.; Wu, X.-F.; Reneker, D. H.; Hou, H., High-strength and high-toughness polyimide nanofibers: Synthesis and characterization. *Journal of Applied Polymer Science* **2010,** *116* (3), 1581.

Cheng, Q.; Tang, J.; Shinya, N.; Qin, L.-C., Polyaniline modified graphene and carbon nanotube composite electrode for asymmetric supercapacitors of high energy density. *Journal of Power Sources* **2013,** *241*, 423.

Chew, S. Y.; Wen, Y.; Dzenis, Y.; Leong, K. W., The role of electrospinning in the emerging field of nanomedicine. *Current Pharmaceutical Design* **2006,** *12* (36), 4751.

Chmiola, J.; Yushin, G.; Gogotsi, Y.; Portet, C.; Simon, P.; Taberna, P. L., Anomalous increase in carbon capacitance at pore sizes less than 1 nanometer. *Science* **2006,** *313* (5794), 1760.

Clegg, S. J., A review of regenerative braking systems. *Institute of Transport Studies* **1996,** *13*, 471.

Cong, H.-P.; Ren, X.-C.; Wang, P.; Yu, S.-H., Flexible graphene–polyaniline composite paper for high-performance supercapacitor. *Energy & Environmental Science* **2013,** *6* (4), 1185.

Conway, B. E., *Electrochemical Supercapacitors: Scientific Fundamentals and Technological Applications*. Springer: New York, 1999; p 698.

Conway, B. E., Transition from "supercapacitor" to "battery" behavior in electrochemical energy storage. *Journal of The Electrochemical Society* **1991,** *138* (6), 1539.

Conway, B. E.; Angerstein-Kozlowska, H., The electrochemical study of multiple-state adsorption in monolayers. *Accounts of Chemical Research* **1981,** *14* (2), 49.

Dong, Z.; Kennedy, S. J.; Wu, Y., Electrospinning materials for energy-related applications and devices. *Journal of Power Sources* **2011,** *196* (11), 4886.

Doshi, J.; Reneker, D. H., Electrospinning process and applications of electrospun fibers. *Journal of Electrostatics* **1995,** *35* (2–3), 151.

Dreyer, D. R.; Park, S.; Bielawski, C. W.; Ruoff, R. S., The chemistry of graphene oxide. *Chemical Society reviews* **2010,** *39* (1), 228.

Drzal, L.; Fukushima, H., Expanded graphite and products produced therefrom. US Patent: 20040127621 A1, 2004.

Duffy, N. W.; Baldsing, W.; Pandolfo, A. G., The nickel–carbon asymmetric supercapacitor—Performance, energy density and electrode mass ratios. *Electrochimica Acta* **2008,** *54* (2), 535.

Dunn, B.; Kamath, H.; Tarascon, J.-M., Electrical energy storage for the grid: A battery of choices. *Science* **2011,** *334* (6058), 928.

Dzenis, Y., Spinning continuous fibers for nanotechnology. *Science* **2004,** *304* (5679), 1917.

Dzenis, Y., Structural nanocomposites. *Science* **2008,** *319* (5862), 419.

El-Kady, M. F.; Strong, V.; Dubin, S.; Kaner, R. B., Laser scribing of high-performance and flexible graphene-based electrochemical capacitors. *Science* **2012,** *335* (6074), 1326.

Endo, M. T., Kim, Y. J.; Koshiba, K.; Ishii, K., High power electric double layer capacitor (EDLC's); from operating principle to pore size control in advanced activated carbons. *Carbon Science* **2001,** *1* (3), 117.

Fan, L.-Z.; Maier, J., High-performance polypyrrole electrode materials for redox supercapacitors. *Electrochemistry Communications* **2006,** *8* (6), 937.

Fan, W.; Zhang, C.; Tjiu, W. W.; Pramoda, K. P.; He, C.; Liu, T., Graphene-wrapped polyaniline hollow spheres as novel hybrid electrode materials for supercapacitor applications. *ACS Applied Materials and Interfaces* **2013,** *5* (8), 3382.

Feng, J. J., Stretching of a straight electrically charged viscoelastic jet. *Journal of Non-Newtonian Fluid Mechanics* **2003,** *116* (1), 55.

Feng, J. J., The stretching of an electrified non-Newtonian jet: A model for electrospinning. *Physics of Fluids (1994-present)* **2002,** *14* (11), 3912.

Fernández, J. A.; Morishita, T.; Toyoda, M.; Inagaki, M.; Stoeckli, F.; Centeno, T. A., Performance of mesoporous carbons derived from poly(vinyl alcohol) in electrochemical capacitors. *Journal of Power Sources* **2008,** *175* (1), 675.

Forward, K. M.; Flores, A.; Rutledge, G. C., Production of core/shell fibers by electrospinning from a free surface. *Chemical Engineering Science* **2013,** *104* (0), 250.

Fowler, J. D.; Allen, M. J.; Tung, V. C.; Yang, Y.; Kaner, R. B.; Weiller, B. H., Practical chemical sensors from chemically derived graphene. *ACS Nano* **2009,** *3* (2), 301.

Frackowiak, E., Carbon materials for supercapacitor application. *Physical Chemistry Chemical Physics: PCCP* **2007,** *9* (15), 1774.

Frackowiak, E.; Béguin, F., Carbon materials for the electrochemical storage of energy in capacitors. *Carbon* **2001,** *39* (6), 937.

Frackowiak, E.; Khomenko, V.; Jurewicz, K.; Lota, K.; Béguin, F., Supercapacitors based on conducting polymers/nanotubes composites. *Journal of Power Sources* **2006,** *153* (2), 413.

Fridrikh, S. V.; Yu, J. H.; Brenner, M. P.; Rutledge, G. C., Controlling the fiber diameter during electrospinning. *Physical Review Letters* **2003,** *90* (14), 144502.

Futaba, D. N.; Hata, K.; Yamada, T.; Hiraoka, T.; Hayamizu, Y.; Kakudate, Y.; Tanaike, O.; Hatori, H.; Yumura, M.; Iijima, S., Shape-engineerable and highly densely packed single-walled carbon nanotubes and their application as super-capacitor electrodes. *Nature Materials* **2006,** *5* (12), 987.

Gamby, J.; Taberna, P. L.; Simon, P.; Fauvarque, J. F.; Chesneau, M., Studies and characterisations of various activated carbons used for carbon/carbon supercapacitors. *Journal of Power Sources* **2001,** *101* (1), 109.

Geim, A. K., Graphene: Status and prospects. *Science* **2009,** *324* (5934), 1530.

Geng, J.; Jefferson, D. A.; Johnson, B. F. G., The unusual nanostructure of nickel-boron catalyst. *Chemical Communications* **2007,** (9), 969.

Ghosh, D.; Giri, S.; Mandal, A.; Das, C. K., Supercapacitor based on H^+ and Ni^{2+} co-doped polyaniline–MWCNTs nanocomposite: synthesis and electrochemical characterization. *RSC Advances* **2013,** *3* (29), 11676.

Gibson, P.; Schreuder-Gibson, H.; Rivin, D., Transport properties of porous membranes based on electrospun nanofibers. *Colloids and Surfaces A: Physicochemical and Engineering Aspects* **2001,** *187–188* (0), 469.

Gómez, H.; Ram, M. K.; Alvi, F.; Villalba, P.; Stefanakos, E.; Kumar, A., Graphene-conducting polymer nanocomposite as novel electrode for supercapacitors. *Journal of Power Sources* **2011,** *196* (8), 4102.

Gopal, R.; Kaur, S.; Ma, Z.; Chan, C.; Ramakrishna, S.; Matsuura, T., Electrospun nanofibrous filtration membrane. *Journal of Membrane Science* **2006,** *281* (1–2), 581.

Greiner, A.; Wendorff, J. H., Electrospinning: A fascinating method for the preparation of ultrathin fibers. *Angewandte Chemie International Edition* **2007,** *46* (30), 5670.

Guceri, S.; Gogotsi, Y. G.; Kuznetsov, V., *Nanoengineered Nanofibrous Materials*. Springer: 2004; 169, p 543.

Guo, Q.; Zhou, X.; Li, X.; Chen, S.; Seema, A.; Greiner, A.; Hou, H., Supercapacitors based on hybrid carbon nanofibers containing multiwalled carbon nanotubes. *Journal of Materials Chemistry* **2009,** *19* (18), 2810.

Gupta, V.; Miura, N., High performance electrochemical supercapacitor from electrochemically synthesized nanostructured polyaniline. *Materials Letters* **2006,** *60* (12), 1466.

Harrop, P. Z., H.; Dinter, M. *Batteries, Supercapacitors, Alternative Storage for Portable Devices 2009–2019*; IDTechEx: 2010; p 217.

He, S.; Hu, X.; Chen, S.; Hu, H.; Hanif, M.; Hou, H., Needle-like polyaniline nanowires on graphite nanofibers: hierarchical micro/nano-architecture for high performance supercapacitors. *Journal of Materials Chemistry* **2012,** *22* (11), 5114.

Hohman, M. M.; Shin, M.; Rutledge, G.; Brenner, M. P., Electrospinning and electrically forced jets. II. Applications. *Physics of Fluids (1994-present)* **2001,** *13* (8), 2221.

Hou, Y.; Cheng, Y.; Hobson, T.; Liu, J., Design and synthesis of hierarchical MnO_2 nanospheres/carbon nanotubes/conducting polymer ternary composite for high performance electrochemical electrodes. *Nano Letters* **2010,** *10* (7), 2727.

Hu, C.-C.; Chen, W.-C., Effects of substrates on the capacitive performance of $RuO_x \cdot nH_2O$ and activated carbon–RuO_x electrodes for supercapacitors. *Electrochimica Acta* **2004,** *49* (21), 3469.

Hu, C.-C.; Lin, J.-Y., Effects of the loading and polymerization temperature on the capacitive performance of polyaniline in $NaNO_3$. *Electrochimica Acta* **2002,** *47* (25), 4055.

Hu, G.; Zhou, Z.; Guo, Y.; Hou, H.; Shao, S., Electrospun rhodium nanoparticle-loaded carbon nanofibers for highly selective amperometric sensing of hydrazine. *Electrochemistry Communications* **2010,** *12* (3), 422.

Hu, L.; Tu, J.; Jiao, S.; Hou, J.; Zhu, H.; Fray, D. J., In situ electrochemical polymerization of a nanorod-PANI-Graphene composite in a reverse micelle electrolyte and its application in a supercapacitor. *Physical Chemistry Chemical Physics : PCCP* **2012,** *14* (45), 15652.

Huang, J.; Kaner, R. B., Nanofiber formation in the chemical polymerization of aniline: A mechanistic study. *Angewandte Chemie International Edition* **2004,** *43* (43), 5817.

Huang, J.; Sumpter, B. G.; Meunier, V., Theoretical model for nanoporous carbon supercapacitors. *Angewandte Chemie International Edition* **2008,** *47* (3), 520.

Huang, Z.-M.; Zhang, Y. Z.; Kotaki, M.; Ramakrishna, S., A review on polymer nanofibers by electrospinning and their applications in nanocomposites. *Composites Science and Technology* **2003,** *63* (15), 2223.

Hyder, M. N.; Lee, S. W.; Cebeci, F. Ç.; Schmidt, D. J.; Shao-Horn, Y.; Hammond, P. T., Layer-by-layer assembled polyaniline nanofiber/multiwall carbon nanotube thin film electrodes for high-power and high-energy storage applications. *ACS Nano* **2011,** *5* (11), 8552.

Inagaki, M.; Konno, H.; Tanaike, O., Carbon materials for electrochemical capacitors. *Journal of Power Sources* **2010,** *195* (24), 7880.

Izadi-Najafabadi, A.; Yasuda, S.; Kobashi, K.; Yamada, T.; Futaba, D. N.; Hatori, H.; Yumura, M.; Iijima, S.; Hata, K., Extracting the full potential of single-walled carbon nanotubes as durable supercapacitor electrodes operable at 4 V with high power and energy density. *Advanced Materials* **2010,** *22* (35), E235.

Ji, L.; Zhang, X., Electrospun carbon nanofibers containing silicon particles as an energy-storage medium. *Carbon* **2009,** *47* (14), 3219.

Kaempgen, M.; Chan, C. K.; Ma, J.; Cui, Y.; Gruner, G., Printable thin film supercapacitors using single-walled carbon nanotubes. *Nano Letters* **2009,** *9* (5), 1872.

Katsnelson, M. I., Graphene: carbon in two dimensions. *Materials Today* **2007,** *10* (1–2), 20.

Kenawy, E.-R.; Bowlin, G. L.; Mansfield, K.; Layman, J.; Simpson, D. G.; Sanders, E. H.; Wnek, G. E., Release of tetracycline hydrochloride from electrospun poly(ethylene-co-vinylacetate), poly(lactic acid), and a blend. *Journal of Controlled Release* **2002,** *81* (1–2), 57.

Khan, Z.; Bhattu, S.; Haram, S.; Khushalani, D., SWCNT/BiVO$_4$ composites as anode materials for supercapacitor application. *RSC Advances* **2014,** *4* (33), 17378.

Khomenko, V.; Frackowiak, E.; Béguin, F., Determination of the specific capacitance of conducting polymer/nanotubes composite electrodes using different cell configurations. *Electrochimica Acta* **2005,** *50* (12), 2499.

Kim, C.; Choi, Y.-O.; Lee, W.-J.; Yang, K.-S., Supercapacitor performances of activated carbon fiber webs prepared by electrospinning of PMDA-ODA poly(amic acid) solutions. *Electrochimica Acta* **2004,** *50* (2–3), 883.

Kim, C.; Ngoc, B. T. N.; Yang, K. S.; Kojima, M.; Kim, Y. A.; Kim, Y. J.; Endo, M.; Yang, S. C., Self-sustained thin webs consisting of porous carbon nanofibers for supercapacitors via the electrospinning of polyacrylonitrile solutions containing zinc chloride. *Advanced Materials* **2007,** *19* (17), 2341.

Kim, C.; Yang, K. S., Electrochemical properties of carbon nanofiber web as an electrode for supercapacitor prepared by electrospinning. *Applied Physics Letters* **2003,** *83* (6), 1216.

Kim, J. S.; Reneker, D. H, Mechanical properties of composites using ultrafine electrospun fibers. *Polymer Composites* **1999**, 20 (1), 124.

Kirichenko, V. N.; Petryanov-Sokolov, I. V.; Suprun, N. N.; Shutov, A. A., Asymptotic radius of a slightly conducting liquid jet in an electric field. *Soviet Physics—Doklady* **1986,** *31*, 611.

Kötz, R.; Carlen, M., Principles and applications of electrochemical capacitors. *Electrochimica Acta* **2000,** *45* (15–16), 2483.

Kumar, A.; Saxena, A.; De, A.; Shankar, R.; Mozumdar, S., Controlled synthesis of size-tunable nickel and nickel oxide nanoparticles using water-in-oil microemulsions. *Advances in Natural Sciences: Nanoscience and Nanotechnology* **2013,** *4* (2), 025009.

Kumar, N. A.; Choi, H.-J.; Shin, Y. R.; Chang, D. W.; Dai, L.; Baek, J.-B., Polyaniline-grafted reduced graphene oxide for efficient electrochemical supercapacitors. *ACS Nano* **2012,** *6* (2), 1715.

Lai, C.; Guo, Q.; Wu, X. F.; Reneker, D. H.; Hou, H., Growth of carbon nanostructures on carbonized electrospun nanofibers with palladium nanoparticles. *Nanotechnology* **2008,** *19* (19), 195303.

Lai, C.; Zhou, Z.; Zhang, L.; Wang, X.; Zhou, Q.; Zhao, Y.; Wang, Y.; Wu, X.-F.; Zhu, Z.; Fong, H., Free-standing and mechanically flexible mats consisting of electrospun carbon nanofibers made from a natural product of alkali lignin as binder-free electrodes for high-performance supercapacitors. *Journal of Power Sources* **2014,** *247*, 134.

Lai, L.; Yang, H.; Wang, L.; Teh, B. K.; Zhong, J.; Chou, H.; Chen, L.; Chen, W.; Shen, Z.; Ruoff, R. S.; Lin, J., Preparation of supercapacitor electrodes through selection of graphene surface functionalities. *ACS Nano* **2012,** *6* (7), 5941.

Laudenslager, M. J.; Scheffler, R. H.; Sigmund, W. M., Electrospun materials for energy harvesting, conversion, and storage: A review. *Pure and Applied Chemistry* **2010,** *82* (11), 2137.

Lee, C.; Wei, X.; Kysar, J. W.; Hone, J., Measurement of the elastic properties and intrinsic strength of monolayer graphene. *Science* **2008,** *321* (5887), 385.

Li, D.; Babel, A.; Jenekhe, S. A.; Xia, Y., Nanofibers of conjugated polymers prepared by electrospinning with a two-capillary spinneret. *Advanced Materials* **2004,** *16* (22), 2062.

Li, D.; Xia, Y., Electrospinning of nanofibers: reinventing the wheel? *Advanced Materials* **2004,** *16* (14), 1151.

Li, L.; Song, H.; Zhang, Q.; Yao, J.; Chen, X., Effect of compounding process on the structure and electrochemical properties of ordered mesoporous carbon/polyaniline composites as electrodes for supercapacitors. *Journal of Power Sources* **2009,** *187* (1), 268.

Li, S.; Luo, Y.; Lv, W.; Yu, W.; Wu, S.; Hou, P.; Yang, Q.; Meng, Q.; Liu, C.; Cheng, H.-M., Vertically aligned carbon nanotubes grown on graphene paper as electrodes in lithium-ion batteries and dye-sensitized solar cells. *Advanced Energy Materials* **2011,** *1* (4), 486.

Li, W.-J.; Laurencin, C. T.; Caterson, E. J.; Tuan, R. S.; Ko, F. K., Electrospun nanofibrous structure: A novel scaffold for tissue engineering. *Journal of Biomedical Materials Research* **2002,** *60* (4), 613.

Li, Y.; Fang, Y.; Liu, H.; Wu, X.; Lu, Y., Free-standing 3D polyaniline-CNT/Ni-fiber hybrid electrodes for high-performance supercapacitors. *Nanoscale* **2012,** *4* (9), 2867.

Li, Z.-F.; Zhang, H.; Liu, Q.; Sun, L.; Stanciu, L.; Xie, J., Fabrication of high-surface-area graphene/polyaniline nanocomposites and their application in supercapacitors. *ACS Applied Materials and Interfaces* **2013,** *5* (7), 2685.

Liang, D.; Hsiao, B. S.; Chu, B., Functional electrospun nanofibrous scaffolds for biomedical applications. *Advanced Drug Delivery Reviews* **2007,** *59* (14), 1392.

Liang, M.; Zhi, L., Graphene-based electrode materials for rechargeable lithium batteries. *Journal of Materials Chemistry* **2009,** *19* (33), 5871.

Kim, J. S.; Reneker, D. H., Mechanical properties of composites using ultrafine electrospun fibers, Polymer Composites **1999**, *20*, 124-131.

Lin, L.-Y.; Yeh, M.-H.; Tsai, J.-T.; Huang, Y.-H.; Sun, C.-L.; Ho, K.-C., A novel core-shell multi-walled carbon nanotube@graphene oxide nanoribbon heterostructure as a potential supercapacitor material. *Journal of Materials Chemistry A* **2013,** *1* (37), 11237.

Lim, C. T.; Tan, E. P. S.; Ng, S. Y., Effects of crystalline morphology on the tensile properties of electrospun polymer nanofibers. *Applied Physics Letters* **2008**, 92 (14), 141908.

Liu, C.; Li, F.; Ma, L.-P.; Cheng, H.-M., Advanced materials for energy storage. *Advanced Materials* **2010,** *22* (8), E28.

Liu, C.; Yu, Z.; Neff, D.; Zhamu, A.; Jang, B. Z., Graphene-based supercapacitor with an ultrahigh energy density. *Nano Letters* **2010,** *10* (12), 4863.

Liu, J.; Yue, Z.; Fong, H., Continuous nanoscale carbon fibers with superior mechanical strength. *Small* **2009,** *5* (5), 536.

Liu, M.; Miao, Y. E.; Zhang, C.; Tjiu, W. W.; Yang, Z.; Peng, H.; Liu, T., Hierarchical composites of polyaniline-graphene nanoribbons-carbon nanotubes as electrode materials in all-solid-state supercapacitors. *Nanoscale* **2013,** *5* (16), 7312.

Liu, T.; Sreekumar, T. V.; Kumar, S.; Hauge, R. H.; Smalley, R. E., SWNT/PAN composite film-based supercapacitors. *Carbon* **2003,** *41* (12), 2440.

Loh, K. P.; Bao, Q.; Ang, P. K.; Yang, J., The chemistry of graphene. *Journal of Materials Chemistry* **2010,** *20* (12), 2277.

Lota, K.; Khomenko, V.; Frackowiak, E., Capacitance properties of poly(3,4-ethylenedioxythiophene)/carbon nanotubes composites. *Journal of Physics and Chemistry of Solids* **2004,** *65* (2–3), 295.

Lukáš, D.; Sarkar, A.; Martinová, L.; Vodsed'álková, K.; Lubasová, D.; Chaloupek, J.; Pokorný, P.; Mikeš, P.; Chvojka, J.; Komárek, M., Physical principles of electrospinning (Electrospinning as a nano-scale technology of the twenty-first century). *Textile Progress* **2009,** *41* (2), 59.

Lukas, D.; Sarkar, A.; Pokorny, P., Self-organization of jets in electrospinning from free liquid surface: A generalized approach. *Journal of Applied Physics* **2008**, *103* (8).

Luo, W.; Hu, X.; Sun, Y.; Huang, Y., Electrospinning of carbon-coated MoO_2 nanofibers with enhanced lithium-storage properties. *Physical Chemistry Chemical Physics* **2011**, *13* (37), 16735.

Luo, W.; Hu, X.; Sun, Y.; Huang, Y., Surface modification of electrospun TiO_2 nanofibers via layer-by-layer self-assembly for high-performance lithium-ion batteries. *Journal of Materials Chemistry* **2012**, *22* (11), 4910.

Luo, Y.; Kong, D.; Jia, Y.; Luo, J.; Lu, Y.; Zhang, D.; Qiu, K.; Li, C. M.; Yu, T., Self-assembled graphene@PANI nanoworm composites with enhanced supercapacitor performance. *RSC Advances* **2013**, *3* (17), 5851.

Lv, W.; Tang, D.-M.; He, Y.-B.; You, C.-H.; Shi, Z.-Q.; Chen, X.-C.; Chen, C.-M.; Hou, P.-X.; Liu, C.; Yang, Q.-H., Low-temperature exfoliated graphenes: vacuum-promoted exfoliation and electrochemical energy storage. *ACS Nano* **2009**, *3* (11), 3730.

Matthews, J. A.; Wnek, G. E.; Simpson, D. G.; Bowlin, G. L., Electrospinning of collagen nanofibers. *Biomacromolecules* **2002**, *3* (2), 232.

Maze, B.; Vahedi Tafreshi, H.; Wang, Q.; Pourdeyhimi, B., A simulation of unsteady-state filtration via nanofiber media at reduced operating pressures. *Journal of Aerosol Science* **2007**, *38* (5), 550.

Meng, C.; Liu, C.; Fan, S., Flexible carbon nanotube/polyaniline paper-like films and their enhanced electrochemical properties. *Electrochemistry Communications* **2009**, *11* (1), 186.

Miao, J.; Miyauchi, M.; Simmons, T. J.; Dordick, J. S.; Linhardt, R. J., Electrospinning of nanomaterials and applications in electronic components and devices. *Journal of Nanoscience and Nanotechnology* **2010,** *10* (9), 5507.

Miller, J. R.; Outlaw, R. A.; Holloway, B. C., Graphene double-layer capacitor with ac line-filtering performance. *Science* **2010,** *329* (5999), 1637.

Miller, J. R.; Simon, P., Materials science. Electrochemical capacitors for energy management. *Science* **2008,** *321* (5889), 651.

Miller, J. R. B., A. F., Electrochemical capacitors: Challenges and opportunities for real-world applications. *The Electrochemical Society Interface* **2008,** *17* (1), 53.

Miloh, T.; Spivak, B.; Yarin, A. L., Needleless electrospinning: Electrically driven instability and multiple jetting from the free surface of a spherical liquid layer. *Journal of Applied Physics* **2009,** *106* (11).

Moghe, A. K.; Gupta, B. S., Co-axial electrospinning for nanofiber structures: Preparation and applications. *Polymer Reviews* **2008,** *48* (2), 353.

Moreno, M.; Ana, M. A. S.; Gonzalez, G.; Benavente, E., Poly(acrylonitrile)-montmorillonite nanocomposites: Effects of the intercalation of the filler on the conductivity of composite polymer electrolytes. *Electrochimica Acta* **2010,** *55* (4), 1323.

Naoi, K. S., P., New materials and new configurations for advanced electrochemical capacitors. *The Electrochemical Society Interface* **2008,** *17* (1), 34.

Niu, C.; Sichel, E. K.; Hoch, R.; Moy, D.; Tennent, H., High power electrochemical capacitors based on carbon nanotube electrodes. *Applied Physics Letters* **1997,** *70* (11), 1480.

Niu, Z.; Luan, P.; Shao, Q.; Dong, H.; Li, J.; Chen, J.; Zhao, D.; Cai, L.; Zhou, W.; Chen, X.; Xie, S., A "skeleton/skin" strategy for preparing ultrathin free-standing single-walled carbon

nanotube/polyaniline films for high performance supercapacitor electrodes. *Energy and Environmental Science* **2012,** *5* (9), 8726.

Novoselov, K. S., Nobel lecture: Graphene: Materials in the flatland. *Reviews of Modern Physics* **2011,** *83* (3), 837.

Novoselov, K. S.; Geim, A. K.; Morozov, S. V.; Jiang, D.; Zhang, Y.; Dubonos, S. V.; Grigorieva, I. V.; Firsov, A. A., Electric field effect in atomically thin carbon films. *Science* **2004,** *306* (5696), 666.

Numao, S.; Judai, K.; Nishijo, J.; Mizuuchi, K.; Nishi, N., Synthesis and characterization of mesoporous carbon nano-dendrites with graphitic ultra-thin walls and their application to supercapacitor electrodes. *Carbon* **2009,** *47* (1), 306.

Obreja, V. V. N., On the performance of supercapacitors with electrodes based on carbon nanotubes and carbon activated material—A review. *Physica E: Low-dimensional Systems and Nanostructures* **2008,** *40* (7), 2596.

Pandolfo, A. G.; Hollenkamp, A. F., Carbon properties and their role in supercapacitors. *Journal of Power Sources* **2006,** *157* (1), 11.

Peng, C.; Jin, J.; Chen, G. Z., A comparative study on electrochemical co-deposition and capacitance of composite films of conducting polymers and carbon nanotubes. *Electrochimica Acta* **2007,** *53* (2), 525.

Petrik, S.; Maly, M., Production nozzle-less electrospinning nanofiber technology. *MRS Proceedings* **2009,** *1240,* 1240-WW03-07 doi:10.1557/PROC-1240-WW03-07.

Pham, Q. P.; Sharma, U.; Mikos, A. G., Electrospinning of polymeric nanofibers for tissue engineering applications: A review. *Tissue Engineering* **2006,** *12* (5), 1197.

Portet, C.; Yushin, G.; Gogotsi, Y., Effect of carbon particle size on electrochemical performance of EDLC. *Journal of The Electrochemical Society* **2008,** *155* (7), A531.

Princen, H. M., Capillary phenomena in assemblies of parallel cylinders: III. Liquid columns between horizontal parallel cylinders. *Journal of Colloid and Interface Science* **1970,** *34* (2), 171.

Qu, D.; Shi, H., Studies of activated carbons used in double-layer capacitors. *Journal of Power Sources* **1998,** *74* (1), 99.

Qu, Q.; Zhu, Y.; Gao, X.; Wu, Y., Core–shell structure of polypyrrole grown on V_2O_5 nanoribbon as high performance anode material for supercapacitors. *Advanced Energy Materials* **2012,** *2* (8), 950.

Ra, E. J.; Raymundo-Piñero, E.; Lee, Y. H.; Béguin, F., High power supercapacitors using polyacrylonitrile-based carbon nanofiber paper. *Carbon* **2009,** *47* (13), 2984.

Ramaseshan, R.; Sundarrajan, S.; Jose, R.; Ramakrishna, S., Nanostructured ceramics by electrospinning. *Journal of Applied Physics* **2007,** *102* (11), 111101.

Reneker, D. H.; Chun, I., Nanometre diameter fibres of polymer, produced by electrospinning. *Nanotechnology* **1996,** *7* (3), 216.

Reneker, D. H.; Yarin, A. L., Electrospinning jets and polymer nanofibers. *Polymer* **2008,** *49* (10), 2387.

Reneker, D. H.; Yarin, A. L.; Fong, H.; Koombhongse, S., Bending instability of electrically charged liquid jets of polymer solutions in electrospinning. *Journal of Applied physics* **2000,** *87* (9), 4531.

Reneker, D. H.; Yarin, A. L.; Zussman, E.; Xu, H., Electrospinning of Nanofibers from Polymer Solutions and Melts. In *Advances in Applied Mechanics*, Hassan, A.; Erik van der, G., Eds. Elsevier: **2007**, 41, p 43.

Rightmire, R. A., Electrical energy storage apparatus. US Patent: 3288641 A, 1966.

Ruoff, R., Graphene: Calling all chemists. *Nature Nanotechnology* **2008,** *3* (1), 10.

Rutledge, G. C.; Fridrikh, S. V., Formation of fibers by electrospinning. *Advanced Drug Delivery Reviews* **2007,** *59* (14), 1384.

Ryu, K. S.; Kim, K. M.; Park, N.-G.; Park, Y. J.; Chang, S. H., Symmetric redox supercapacitor with conducting polyaniline electrodes. *Journal of Power Sources* **2002,** *103* (2), 305.

Sarangapani, S.; Tilak, B. V.; Chen, C. P., Materials for electrochemical capacitors: Theoretical and experimental constraints. *Journal of The Electrochemical Society* **1996,** *143* (11), 3791.

Schulz, D. L.; Hoey, J.; Smith, J.; Elangovan, A.; Wu, X.; Akhatov, I.; Payne, S.; Moore, J.; Boudjouk, P.; Pederson, L.; Xiao, J.; Zhang, J.-G., Si_6H_{12}/polymer inks for electrospinning a-Si nanowire lithium ion battery anodes. *Electrochemical and Solid-State Letters* **2010,** *13* (10), A143.

Seo, M.-K.; Park, S.-J., Electrochemical characteristics of activated carbon nanofiber electrodes for supercapacitors. *Materials Science and Engineering: B* **2009,** *164* (2), 106.

Sharma, A.; Tyagi, V. V.; Chen, C. R.; Buddhi, D., Review on thermal energy storage with phase change materials and applications. *Renewable and Sustainable Energy Reviews* **2009,** *13* (2), 318.

Shin, Y. M.; Hohman, M. M.; Brenner, M. P.; Rutledge, G. C., Electrospinning: A whipping fluid jet generates submicron polymer fibers. *Applied Physics Letters* **2001,** *78* (8), 1149.

Simon, P.; Gogotsi, Y., Materials for electrochemical capacitors. *Nature Materials* **2008,** *7* (11), 845.

Sinha-Ray, S.; Pelot, D. D.; Zhou, Z. P.; Rahman, A.; Wu, X. F.; Yarin, A. L., Encapsulation of self-healing materials by coelectrospinning, emulsion electrospinning, solution blowing and intercalation. *Journal of Materials Chemistry* **2012,** *22* (18), 9138.

Smith, D. J.; Kataphinan, W.; Reneker, D. H.; Dabney, S., Preservation of biological materials using fiber-forming techniques. US Patent: 2450539 A1, 2004.

Smith, D. J.; Reneker, D. H.; McManus, A. T.; Schreuder-Gibson, H. L.; Mello, C.; Sennett, M. S., Electrospun fibers and an apparatus therefor. US Patent: 6753454 B1, 2004.

Snook, G. A.; Kao, P.; Best, A. S., Conducting-polymer-based supercapacitor devices and electrodes. *Journal of Power Sources* **2011,** *196* (1), 1.

Song, M.-K.; Park, S.; Alamgir, F. M.; Cho, J.; Liu, M., Nanostructured electrodes for lithium-ion and lithium-air batteries: the latest developments, challenges, and perspectives. *Materials Science and Engineering R: Reports* **2011,** *72* (11), 203.

Spivak, A. F.; Dzenis, Y. A., Asymptotic decay of radius of a weakly conductive viscous jet in an external electric field. *Applied Physics Letters* **1998,** *73* (21), 3067.

Spivak, A. F.; Dzenis, Y. A., A condition of the existence of a conductive liquid meniscus in an external electric field. *Journal of Applied Mechanics* **1999,** *66* (4), 1026.

Spivak, A. F.; Dzenis, Y. A.; Reneker, D. H., A model of steady state jet in the electrospinning process. *Mechanics Research Communications* **2000,** *27* (1), 37.

Srinivasan, V.; Weidner, J. W., An electrochemical route for making porous nickel oxide electrochemical capacitors. *Journal of The Electrochemical Society* **1997,** *144* (8), L210.

Stoller, M. D.; Park, S.; Zhu, Y.; An, J.; Ruoff, R. S., Graphene-based ultracapacitors. *Nano Letters* **2008,** *8* (10), 3498.

Su, D. S.; Schlögl, R., Nanostructured carbon and carbon nanocomposites for electrochemical energy storage applications. *ChemSusChem* **2010,** *3* (2), 136.

Sun, Z.; Zussman, E.; Yarin, A. L.; Wendorff, J. H.; Greiner, A., Compound core–shell polymer nanofibers by co-electrospinning. *Advanced Materials* **2003,** *15* (22), 1929.

Sung, J.-H.; Kim, S.-J.; Jeong, S.-H.; Kim, E.-H.; Lee, K.-H., Flexible micro-supercapacitors. *Journal of Power Sources* **2006,** *162* (2), 1467.

Tan, Q. I., P.; Cao, Y., Advanced dielectrics for capacitors. *IEEE Transactions on Fundamentals and Materials* **2006,** *126* (11), 1153.

Tang, Q.; Wu, J.; Sun, X.; Li, Q.; Lin, J., Shape and size control of oriented polyaniline microstructure by a self-assembly method. *Langmuir* **2009,** *25* (9), 5253.

Taylor, G., Disintegration of water drops in an electric field. *Proceedings of the Royal Society of London. Series A: Mathematical and Physical Sciences* **1964,** *280* (1382), 383.

Taylor, G., Electrically driven jets. *Proceedings of the Royal Society of London. A: Mathematical and Physical Sciences* **1969,** *313* (1515), 453.

Thompson, C.J.; Chase, G. G.; Yarin, A. L.; Reneker, D. H., Effects of parameters on nanofiber diameter determined from electrospinning model. *Polymer* **2007**, 48, 6913.

Theron, S. A.; Yarin, A. L.; Zussman, E.; Kroll, E., Multiple jets in electrospinning: Experiment and modeling. *Polymer* **2005,** *46* (9), 2889.

Toupin, M.; Brousse, T.; Bélanger, D., Charge storage mechanism of MnO_2 electrode used in aqueous electrochemical capacitor. *Chemistry of Materials* **2004,** *16* (16), 3184.

Wan, W. B.; Zhao, Z. B.; Fan, Y. R.; Hu, H.; Zhou, Q.; Qiu, J. S., Graphene derivatives: Synthesis and applications. *Progress in Chemistry* **2011,** *23* (9), 1883.

Wang, C. Y.; Mottaghitalab, V.; Too, C. O.; Spinks, G. M.; Wallace, G. G., Polyaniline and polyaniline–carbon nanotube composite fibres as battery materials in ionic liquid electrolyte. *Journal of Power Sources* **2007,** *163* (2), 1105.

Wang, D.-W.; Li, F.; Zhao, J.; Ren, W.; Chen, Z.-G.; Tan, J.; Wu, Z.-S.; Gentle, I.; Lu, G. Q.; Cheng, H.-M., Fabrication of graphene/polyaniline composite paper via in situ anodic electropolymerization for high-performance flexible electrode. *ACS Nano* **2009,** *3* (7), 1745.

Wang, X.; Li, G.; Chen, Z.; Augustyn, V.; Ma, X.; Wang, G.; Dunn, B.; Lu, Y., High-performance supercapacitors based on nanocomposites of Nb_2O_5 nanocrystals and carbon nanotubes. *Advanced Energy Materials* **2011,** *1* (6), 1089.

Wang, Y. G.; Li, H. Q.; Xia, Y. Y., Ordered whiskerlike polyaniline grown on the surface of mesoporous carbon and its electrochemical capacitance performance. *Advanced Materials* **2006,** *18* (19), 2619.

Washburn, E. W., The Dynamics of capillary flow. *Physical Review* **1921,** *17* (3), 273.

Wei, J.; Zhang, J.; Liu, Y.; Xu, G.; Chen, Z.; Xu, Q., Controlled growth of whisker-like polyaniline on carbon nanofibers and their long cycle life for supercapacitors. *RSC Advances* **2013,** *3* (12), 3957.

Whittingham, M. S., Materials challenges facing electrical energy storage. *MRS Bullutin* **2008,** *33* (04), 411.

Winter, M.; Brodd, R. J., What are batteries, fuel cells, and supercapacitors? *Chemical Reviews* **2004,** *104* (10), 4245.

Wu, Q.; Xu, Y.; Yao, Z.; Liu, A.; Shi, G., Supercapacitors based on flexible graphene/polyaniline nanofiber composite films. *ACS Nano* **2010,** *4* (4), 1963.

Wu, X.-F., *Fracture of Advanced Polymer Composites with Nanofiber-Reinforced Interface* (Ph.D. Disseration), University of Nebraska-Lincoln, NE, USA (2003).

Wu, X.-F., *Fracture of Advanced Polymer Composites with Nanofiber-Reinforced Interface-Farbication, Characterizaiton and Modeling, VDM Verlag Publishing House, Germany* (2009).

Wu, X.-F., Wave propagation in prestretched polymer nanofibers. *Journal of Applied Physics* **2010,** *107* (1), 013509.

Wu, X.-F.; Bedarkar, A.; Vaynberg, K. A., Droplets wetting on filament rails: Surface energy and morphology transition. *Journal of Colloid and Interface Science* **2010,** *341* (2), 326.

Wu, X.-F.; Dzenis, Y. A., Electrohydrodynamic instability of thin conductive liquid films. *Journal of Physics D: Applied Physics* **2005,** *38* (16), 2848.

Wu, X.-F.; Rahman, A.; Zhou, Z.; Pelot, D. D.; Sinha-Ray, S.; Chen, B.; Payne, S.; Yarin, A. L., Electrospinning core-shell nanofibers for interfacial toughening and self-healing of carbon-fiber/epoxy composites. *Journal of Applied Polymer Science* **2013,** *129* (3), 1383.

Wu, X.-F.; Salkovskily, Y.; Dzenis, Y. A., Modeling of solvent evaporation from polymer jets in electrospinning. *Applied Physics Letters* **2011,** 98 (22), 223108.

Wu, X.-F.; Yarin, A. L., Recent progress in interfacial toughening and damage self-healing of polymer composites based on electrospun and solution-blown nanofibers: An overview. *Journal of Applied Polymer Science* **2013,** *130* (4), 2225.

Wu, X.-F.; Zhou, Z.; Rahman, A.; Bedarkar, A., Mechanical properties of continuous nanofibers: characterization and mechanics, In: *Nanostructures: Properties, Production Methods and*

Applications, Chapter 8, pp. 247-285 (Editor: Yu Dong), Nova Scientific Publisher, New York, USA (2013).

Wu, X.-F.; Zhou, Z.; Zhou, W.-M., Electrical contact resistance in filaments. *Applied Physics Letters* **2012,** *100* (19), 193115.

Wu, Z.-S.; Pei, S.; Ren, W.; Tang, D.; Gao, L.; Liu, B.; Li, F.; Liu, C.; Cheng, H.-M., Field emission of single-layer graphene films prepared by electrophoretic deposition. *Advanced Materials* **2009,** *21* (17), 1756.

Wu, Z.-S.; Ren, W.; Gao, L.; Zhao, J.; Chen, Z.; Liu, B.; Tang, D.; Yu, B.; Jiang, C.; Cheng, H.-M., Synthesis of graphene sheets with high electrical conductivity and good thermal stability by hydrogen arc discharge exfoliation. *ACS Nano* **2009,** *3* (2), 411.

Xie, J.; Li, X.; Xia, Y., Putting electrospun nanofibers to work for biomedical research. *Macromolecular Rapid Communications* **2008,** *29* (22), 1775.

Xu, X.; Zhuang, X.; Chen, X.; Wang, X.; Yang, L.; Jing, X., Preparation of core-sheath composite nanofibers by emulsion electrospinning. *Macromolecular Rapid Communications* **2006,** *27* (19), 1637.

Xu, Y.; Wang, J.; Sun, W.; Wang, S., Capacitance properties of poly(3,4-ethylenedioxythiophene)/polypyrrole composites. *Journal of Power Sources* **2006,** *159* (1), 370.

Yan, J.; Fan, Z.; Wei, T.; Qian, W.; Zhang, M.; Wei, F., Fast and reversible surface redox reaction of graphene–MnO_2 composites as supercapacitor electrodes. *Carbon* **2010,** *48* (13), 3825.

Yan, J.; Liu, J.; Fan, Z.; Wei, T.; Zhang, L., High-performance supercapacitor electrodes based on highly corrugated graphene sheets. *Carbon* **2012,** *50* (6), 2179.

Yan, J.; Wei, T.; Fan, Z.; Qian, W.; Zhang, M.; Shen, X.; Wei, F., Preparation of graphene nanosheet/carbon nanotube/polyaniline composite as electrode material for supercapacitors. *Journal of Power Sources* **2010,** *195* (9), 3041.

Yan, X.; Tai, Z.; Chen, J.; Xue, Q., Fabrication of carbon nanofiber-polyaniline composite flexible paper for supercapacitor. *Nanoscale* **2011,** *3* (1), 212.

Yarin, A.; Koombhongse, S.; Reneker, D., Bending instability in electrospinning of nanofibers. *Journal of Applied Physics* **2001,** *89* (5), 3018.

Yarin, A. L., Coaxial electrospinning and emulsion electrospinning of core-shell fibers. *Polymers for Advanced Technologies* **2011,** *22* (3), 310.

Yarin, A. L.; Zussman, E., Upward needleless electrospinning of multiple nanofibers. *Polymer* **2004,** *45* (9), 2977.

Yu, D.; Dai, L., Self-Assembled Graphene/Carbon Nanotube Hybrid Films for Supercapacitors. *The Journal of Physical Chemistry Letters* **2009,** *1* (2), 467.

Yuan, D.-s.; Zhou, T.-x.; Zhou, S.-l.; Zou, W.-j.; Mo, S.-s.; Xia, N.-n., Nitrogen-enriched carbon nanowires from the direct carbonization of polyaniline nanowires and its electrochemical properties. *Electrochemistry Communications* **2011,** *13* (3), 242.

Zhang, K.; Zhang, L. L.; Zhao, X. S.; Wu, J., Graphene/polyaniline nanofiber composites as supercapacitor electrodes. *Chemistry of Materials* **2010,** *22* (4), 1392.

Zhang, L. L.; Zhao, X. S., Carbon-based materials as supercapacitor electrodes. *Chemical Society reviews* **2009,** *38* (9), 2520.

Zhang, X.; Ji, L.; Toprakci, O.; Liang, Y.; Alcoutlabi, M., Electrospun nanofiber-based anodes, cathodes, and separators for advanced lithium-ion batteries. *Polymer Reviews* **2011,** *51* (3), 239.

Zhang, Y.; Tan, Y.-W.; Stormer, H. L.; Kim, P., Experimental observation of the quantum hall effect and Berry's phase in graphene. *Nature* **2005,** *438* (7065), 201.

Zhao, X.; Sanchez, B. M.; Dobson, P. J.; Grant, P. S., The role of nanomaterials in redox-based supercapacitors for next generation energy storage devices. *Nanoscale* **2011,** *3* (3), 839.

Zheng, J. P.; Cygan, P. J.; Jow, T. R., Hydrous ruthenium oxide as an electrode material for electrochemical capacitors. *Journal of The Electrochemical Society* **1995,** *142* (8), 2699.

Zhou, S.; Zhang, H.; Wang, X.; Li, J.; Wang, F., Sandwich nanocomposites of polyaniline embedded between graphene layers and multi-walled carbon nanotubes for cycle-stable electrode materials of organic supercapacitors. *RSC Advances* **2013,** *3* (6), 1797.

Zhou, S. J.; Ma, C. Y.; Meng, Y. Y.; Su, H. F.; Zhu, Z.; Deng, S. L.; Xie, S. Y., Activation of boron nitride nanotubes and their polymer composites for improving mechanical performance. *Nanotechnology* **2012,** *23* (5), 055708.

Zhou, Y.-k.; He, B.-l.; Zhou, W.-j.; Huang, J.; Li, X.-h.; Wu, B.; Li, H.-l., Electrochemical capacitance of well-coated single-walled carbon nanotube with polyaniline composites. *Electrochimica Acta* **2004,** *49* (2), 257.

Zhou, Y.; Qin, Z.-Y.; Li, L.; Zhang, Y.; Wei, Y.-L.; Wang, L.-F.; Zhu, M.-F., Polyaniline/multi-walled carbon nanotube composites with core–shell structures as supercapacitor electrode materials. *Electrochimica Acta* **2010,** *55* (12), 3904.

Zhou, Z. P.; Lai, C.; Zhang, L.; Qian, Y.; Hou, H.; Reneker, D. H.; Fong, H., Development of carbon nanofibers from aligned electrospun polyacrylonitrile nanofiber bundles and characterization of their microstructural, electrical, and mechanical properties. *Polymer* **2009,** *50* (13), 2999.

Zhou, Z. P.; Liu, K.; Lai, C.; Zhang, L.; Li, J.; Hou, H.; Reneker, D. H.; Fong, H., Graphitic carbon nanofibers developed from bundles of aligned electrospun polyacrylonitrile nanofibers containing phosphoric acid. *Polymer* **2010,** *51* (11), 2360.

Zhou, Z. P.; Wu, X.-F., Graphene-beaded carbon nanofibers for use in supercapacitor electrodes: Synthesis and electrochemical characterization. *Journal of Power Sources* **2013,** *222*, 410.

Zhou, Z. P.; Wu, X.-F., High-performance porous electrodes for pseudosupercapacitors based on graphene-beaded carbon nanofibers surface-coated with nanostructured conducting polymers. *Journal of Power Sources* **2014,** *262*, 44.

Zhou, Z. P.; Wu, X.-F.; Ding, Y. C.; Yu, M.; Zhao, Y. H.; Jiang, L.; Xuan, C. L.; Sun, C. W., Needleless emulsion electrospinning for scalable fabrication of core–shell nanofibers. *Journal of Applied Polymer Science* **2014**, DOI: 10.1002/app.40896.

Zhou, Z. P.; Wu, X.-F.; Fong, H., Electrospun carbon nanofibers surface-grafted with vapor-grown carbon nanotubes as hierarchical electrodes for supercapacitors. *Applied Physics Letters* **2012,** *100* (2), 023115.

Zhou, Z. P.; Wu, X.-F.; Gao, X.; Jiang, L.; Zhao, Y.; Fong, H., Parameter dependence of conic angle of nanofibres during electrospinning. *Journal of Physics D: Applied Physics* **2011,** *44* (43), 435401.

Zhou, Z. P.; Wu, X.-F.; Hou, H. Q., Electrospun carbon nanofibers surface-grown with carbon nanotubes and polyaniline for use as high-performance electrode materials of supercapacitors. *RSC Advances* **2014**, DOI: 10.1039/C4RA00964A.

Zhu, Y.; Murali, S.; Cai, W.; Li, X.; Suk, J. W.; Potts, J. R.; Ruoff, R. S., Graphene and graphene oxide: synthesis, properties, and applications. *Advanced Materials* **2010,** *22* (35), 3906.

Zhu, Y.; Murali, S.; Stoller, M. D.; Ganesh, K. J.; Cai, W.; Ferreira, P. J.; Pirkle, A.; Wallace, R. M.; Cychosz, K. A.; Thommes, M.; Su, D.; Stach, E. A.; Ruoff, R. S., Carbon-based supercapacitors produced by activation of graphene. *Science* **2011,** *332* (6037), 1537.

Ziebro, J.; Lukasiewicz, I.; Borowiak-Palen, E.; Michalkiewicz, B., Low temperature growth of carbon nanotubes from methane catalytic decomposition over nickel supported on a zeolite. *Nanotechnology* **2010,** *21* (14), 145308.